

國立臺灣大學工學院工程科學及海洋工程學研究所



碩士論文

Department of Engineering Science and Ocean Engineering

College of Engineering

National Taiwan University

Master Thesis

波浪邊界層流場渦漩結構之擷取

Extraction of vortical structures in boundary layer next to wavy
surface

陳柏丞

Po-Chen Chen

指導教授：蔡武廷 教授

Advisor: Wu-Ting Tsai, Ph.D.

中華民國 106 年 10 月

October, 2017

國立臺灣大學碩士學位論文
口試委員會審定書

波浪邊界層紊流場渦漩結構之擷取

Extraction of vortical structures in boundary layer next to
wavy surface

本論文係陳柏丞君（學號 R04525010）在國立臺灣大學工程科學及海洋工程學系完成之碩士學位論文，於民國 106 年 10 月 5 日承下列考試委員審查通過及口試及格，特此證明

口試委員：



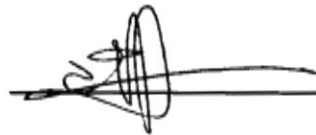
（指導教授）

周廷倫

戴憲恒

黃印良

陳世楨



系主任

江英雄

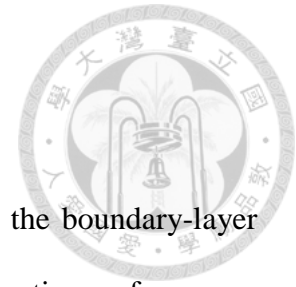
中文摘要



本研究旨於探究自由傳播波浪下之流場、波狀面上之空氣紊流場邊界層內之渦旋結構。我們採用四種建立於速度應變率特徵之旋渦結構辨識方法，並與傳統與渦度向量有關之方法比較。此外，條件平均法也被運用於擷取馬蹄形渦旋結構。在兩種流場中，四種渦旋結構辨識方法皆可得到相近之結果。在自由傳播波浪下之流場，可以觀察到沿流向伸展、成對反向旋轉之渦旋結構。藉由比較渦旋結構辨識方法和與渦度向量有關之方法，可以得知以渦旋結構辨識方法來研究流場較為直覺。在波浪上之空氣紊流場中，可以觀察到馬蹄型渦旋結構及類沿流向渦旋結構，我們也觀察到了馬蹄型渦旋結構的演化並發現其紊流場存在大尺度之旋轉運動。此外，條件平均的結果顯示象限分析取樣法較 VISA 取樣法佳。

關鍵字: 邊界層、渦旋結構、波浪表面、漩渦結構辨識方法、條件平均法

Abstract



In this thesis we study the coherent vortical structures within the boundary-layer flow next to a wavy surface. Both aqueous flow beneath a free-propagating surface wave and turbulent air flow above a prescribed propagating wavy boundary are considered. Four vortex identification schemes based on the characteristics of velocity-strain rate are adopted to extract the vortical structures. These schemes are also compared with traditional methods based on vorticity vector. Conditional averaging technique of the flow field is also applied to extract the horseshoe vortices. In both aqueous and air flow, four vortex identification schemes derive similar results. For the aqueous flow underneath a free-propagating surface wave, counter-rotating vortex pairs that elongate along streamwise direction are observed. By comparing vortex identification schemes with methods based on vorticity vector, it is found that observing vortical structures is a more intuitive way to study the flow field. For the air flow above a prescribed propagating wavy boundary, horseshoe vortices and quasi-streamwise vortices are found, the regeneration of forward horseshoe vortices are observed, and the larger scale vortical motions in the flow field above wavy surface are discovered. In addition, the conditional averaging results shows that out of the two sampling criterions, the quadrant analysis sampling technique is more feasible than the VISA sampling technique.

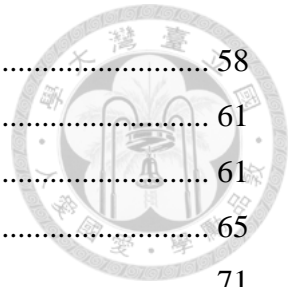
Keyword: boundary layer, vortical structures, wavy surface, vortex identification method, conditional averaging method

Contents



中文摘要	i
Abstract	ii
Contents	iii
List of figures	v
List of tables	xii
Chapter 1.	Introduction	1
1.1	Research background and objectives.....	1
1.2	Outline of this thesis	3
Chapter 2.	Conditional averaging method.....	5
2.1	Quadrant analysis	6
2.2	VISA sampling technique.....	8
Chapter 3.	Vortex identification methods.....	9
3.1	Q Criterion.....	10
3.2	Δ Criterion	12
3.3	λ_2 Criterion.....	14
3.4	λ_{ci} Criterion.....	17
3.5	Relation between Q , Δ , λ_2 and λ_{ci}	18
Chapter 4.	Coherent vortical structures beneath free-propagating wavy surface ..	21
4.1	Numerical simulation	21
4.2	Results of vortical structure identification.....	23
4.2.1	Equivalent thresholds	23
4.2.2	Vortical structures.....	27
4.2.3	Relation between vorticity inclination angle and vortical structures	29
Chapter 5.	Coherent vortical structures above wavy surface	35
5.1	Numerical simulation	35
5.2	Results of structure identification.....	38
5.2.1	Equivalent thresholds	41
5.2.2	Vortical structures.....	45
5.2.3	Regeneration of the forward horseshoe vortices	54

5.2.4	Larger scale vortical motions	58
5.3	Conditional averaging analysis.....	61
5.3.1	Conditional averaging procedures.....	61
5.3.2	Subjective conditional average	65
5.3.3	Autonomous conditional average.....	71
Chapter 6.	Conclusion	83
References	85
Appendix A.	Phase plane method and critical point theory	87
Appendix B.	Properties of the Hessian matrix.....	89



List of figures



Figure 2-1: Quadrant of instantaneous u', w' -plane, u' and w' is the streamwise and spanwise turbulent velocity, respectively. 7

Figure 4-1: Vortical structures beneath free-propagating wavy surface. The vortical structures are represented by the isosurface of (a) $Q = 0.001$, (b) $\Delta = 3.7 \times 10^{-11}$, (c) $\lambda_2 = -0.001$, (d) $\lambda_{ci}^2 = 0.001$. The structures with $\omega'_x > 0$ are marked in red color; the structures with $\omega'_x < 0$ are marked in blue color. 24

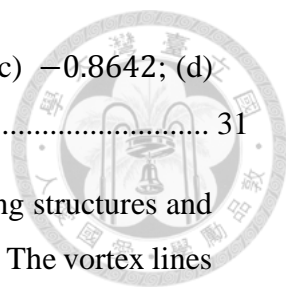
Figure 4-2: Vortical structures beneath free-propagating wavy surface. The vortical structures are represented by the isosurface of (a) $Q = 0.003$, (b) $\Delta = 10^{-9}$, (c) $\lambda_2 = -0.003$, (d) $\lambda_{ci}^2 = 0.003$. The structures with $\omega'_x > 0$ are marked in red color; the structures with $\omega'_x < 0$ are marked in blue color. 25

Figure 4-3: Vortical structures beneath free-propagating wavy surface. The vortical structures are represented by isosurface of (a) $\lambda_{ci}^2 = 0.003$, (b) $\lambda_{ci}^2 = 0.002$ (c) $\lambda_{ci}^2 = 0.001$, (d) $\lambda_{ci}^2 = 0.0005$. The structures with $\omega'_x > 0$ are marked in red color; the structures with $\omega'_x < 0$ are marked in blue color. 27

Figure 4-4: (a) The vortical structures beneath free-propagating wavy surface. (b) Temperature contour on the water surface. (c) Combination of (a) and (b). The wave propagates from left to right and the vortical structures are represented by isosurface of $\lambda_{ci}^2 = 0.003$. Examples of cool streaks and warm bands are marked by circular dots and cross signs, respectively. The structures with $\omega'_x > 0$ are marked in red color; the structures with $\omega'_x < 0$ are marked in blue color. 28

Figure 4-5: Sign convention for vorticity inclination angles θ and ϕ 30

Figure 4-6: Distribution of the inclination angle of the projection of the vorticity vectors in (x, y) -planes; data weighted with the magnitude of the



projected vorticity. (a) $z = -0.0474$; (b) -0.1032 ; (c) -0.8642 ; (d) -0.9851 . (e) Presumptions of the structures. 31

Figure 4-7: (a) Vortex lines among structures. (b) Vortex lines among structures and contour distribution of temperature on the water surface. The vortex lines are drawn with velocities fluctuation. The vortical structures are represented by isosurface of $\lambda_{ci}^2 = 0.003$ 32

Figure 4-8: Distribution of the inclination angle of the projection of the vorticity vectors in (x, y) -planes; data weighted with the magnitude of the projected vorticity and filtered by $\lambda_2 < 0$. (a) $z = -0.0474$; (b) -0.1032 ; (c) -0.8642 ; (d) -0.9851 . (e) Presumptions of the structures. 33

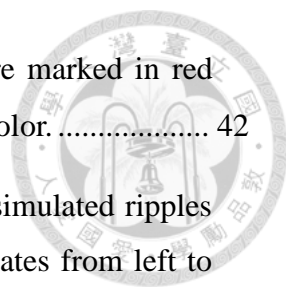
Figure 5-1: An illustration of physical domain (left) and computational domain (right) above wavy surface. 36

Figure 5-2: Wave shape of (a) artificial ripples with $ak = 0.2$; and (b) simulated ripples with $ak = 0.3$ 37

Figure 5-3: (Top view) Vortical structures above wavy surface of artificial ripples with $ak = 0.2$. The wave propagates from left to right and the vortical structures are represented by isosurface of (a) $\lambda_{ci}^2 = 2$, (b) $\lambda_{ci}^2 = 3$ (c) $\lambda_{ci}^2 = 4$, (d) $\lambda_{ci}^2 = 5$. The structures with $\omega'_x > 0$ are marked in red color; the structures with $\omega'_x < 0$ are marked in blue color. 39

Figure 5-4: (Top view) Vortical structures above wavy surface of simulated ripples with $ak = 0.3$, time sequence = 05. The wave propagates from left to right and the vortical structures are represented by isosurface of (a) $\lambda_{ci}^2 = 3.5$, (b) $\lambda_{ci}^2 = 4$, (c) $\lambda_{ci}^2 = 4.5$, (d) $\lambda_{ci}^2 = 5$. The structures with $\omega'_x > 0$ are marked in red color; the structures with $\omega'_x < 0$ are marked in blue color. 40

Figure 5-5: (Top view) Vortical structures above wavy surface of artificial ripples with $ak = 0.2$. The wave propagates from left to right and the vortical structures are represented by the isosurface of (a) $Q = 4$, (b) $\Delta = 4$, (c)



$\lambda_2 = -4$, (d) $\lambda_{ci}^2 = 4$. The structures with $\omega'_x > 0$ are marked in red color; the structures with $\omega'_x < 0$ are marked in blue color. 42

Figure 5-6: (Top view) Vortical structures above wavy surface of simulated ripples with $ak = 0.3$, time sequence = 05. The wave propagates from left to right and the vortical structures are represented by the isosurface of (a) $Q = 4$, (b) $\Delta = 2.37$, (c) $\lambda_2 = -4$, (d) $\lambda_{ci}^2 = 4$. The structures with $\omega'_x > 0$ are marked in red color; the structures with $\omega'_x < 0$ are marked in blue color. 43

Figure 5-7: (Top view) Vortical structures above wavy surface of simulated ripples with $ak = 0.3$, time sequence = 05. The wave propagates from left to right and the vortical structures are represented by the isosurface of (a) $Q = 4$, (b) $\Delta = 6$, (c) $\lambda_2 = -4$, (d) $\lambda_{ci}^2 = 4$. The structures with $\omega'_x > 0$ are marked in red color; the structures with $\omega'_x < 0$ are marked in blue color. 44

Figure 5-8: Vortical structures above wavy surface of artificial ripples with $ak = 0.2$: (a) oblique view; (b) top view. The wave propagates from left to right and the vortical structures are represented by the isosurface of $\lambda_{ci}^2 = 4$. The structures with $\omega'_x > 0$ are marked in red color; the structures with $\omega'_x < 0$ are marked in blue color. 46

Figure 5-9: Forward and reversed horseshoe vortices above wavy surface of artificial ripples with $ak = 0.2$. The wave propagates from left to right and the vortical structures are represented by the isosurface of $\lambda_{ci}^2 = 4$. The structures with $\omega'_x > 0$ are marked in red color; the structures with $\omega'_x < 0$ are marked in blue color. 47

Figure 5-10: Time evolution of vortical structures above wavy surface of artificial ripples with $ak = 0.3$ (oblique and top view): (a, b) time sequence = 01; (c, d) 02; (e, f) 03; (g, h) 04; (i, j) 05. The wave propagates from left to right and the vortical structures are represented by the isosurface of $\lambda_{ci}^2 = 4$. The structures with $\omega'_x > 0$ are marked in red color; the structures with $\omega'_x < 0$ are marked in blue color. 52

- Figure 5-11: Forward and reversed horseshoe vortices above wavy surface of simulated ripples with $ak = 0.3$, time sequence = 05. The wave propagates from left to right and the vortical structures are represented by the isosurface of $\lambda_{ci}^2 = 4$. The structures with $\omega'_x > 0$ are marked in red color; the structures with $\omega'_x < 0$ are marked in blue color. 53
- Figure 5-12: Enlarged view of the forward horseshoe vortex marked by the green box above wavy surface of simulated ripples with $ak = 0.3$. The wave propagates from left to right and the vortical structures are represented by the isosurface of $\lambda_{ci}^2 = 4$. The structures with $\omega'_x > 0$ are marked in red color; the structures with $\omega'_x < 0$ are marked in blue color. 55
- Figure 5-13: Time evolution of the forward horseshoe vortex above wavy surface (oblique and top view): (a, b) time sequence = 01; (c, d) 02; (e, f) 03; (g, h) 04; (i, j) 05. The wave propagates from left to right and the vortical structures are represented by the isosurface of $\lambda_{ci}^2 = 4$ 57
- Figure 5-14: (a) Vortical structures above wavy surface of simulated ripples with $ak = 0.3$, time sequence = 05. (b) Vortical structures and streamwise turbulent velocity contour above these structures. The wave propagates from left to right and the vortical structures are represented by the isosurface of $\lambda_{ci}^2 = 4$. The structures with $\omega'_x > 0$ are marked in red color; the structures with $\omega'_x < 0$ are marked in blue color. 59
- Figure 5-15: Distribution of streamwise-averaged (a) streamwise, (b) spanwise and (c) vertical turbulent velocity above wavy surface of simulated ripples with $ak = 0.3$, time sequence = 05. The green and yellow arrows indicate flow directions. The dotted lines mark the interface of fast and slow-moving fluids..... 60
- Figure 5-16: An illustration of conditional averaging in the computational domain..... 63
- Figure 5-17: An illustration of conditional averaging in the physical domain. 64
- Figure 5-18: Above wavy surface of artificial ripples with $ak = 0.2$: educed reversed horseshoe vortex by conditional averaging subjectively. The structures are represented by the isosurface of (a) $Q = 4$, (b) $\Delta = 30$, (c) $\lambda_2 =$

-4, (d) $\lambda_{ci}^2 = 4$. The structures with $\omega'_x > 0$ are marked in red color; the structures with $\omega'_x < 0$ are marked in blue color. 67

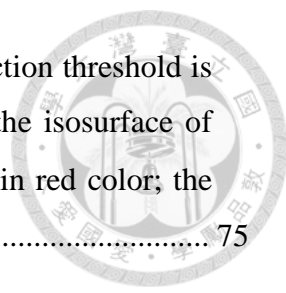
Figure 5-19: Above wavy surface of artificial ripples with $ak = 0.2$: (a) the position of the contour slice; side view of the educed reversed horseshoe vortex by conditional averaging subjectively and contours of (b) streamwise, (c) vertical turbulent velocity, (d) partial derivative of the streamwise turbulent velocity with respect to x . The structures are represented by the isosurface of $\lambda_{ci}^2 = 4$. The structures with $\omega'_x > 0$ are marked in red color; the structures with $\omega'_x < 0$ are marked in blue color. The green arrows indicate flow directions. 68

Figure 5-20: Above wavy surface of simulated ripples with $ak = 0.3$, time sequence = 05: educed reversed horseshoe vortex by conditional averaging subjectively. The structures are represented by the isosurface of (a) $Q = 8$, (b) $\Delta = 100$, (c) $\lambda_2 = -8$, (d) $\lambda_{ci}^2 = 2$. The structures with $\omega'_x > 0$ are marked in red color; the structures with $\omega'_x < 0$ are marked in blue color. 69

Figure 5-21: Above wavy surface of simulated ripples with $ak = 0.3$, time sequence = 05: educed forward horseshoe vortex by conditional averaging subjectively. The structures are represented by the isosurface of (a) $Q = 2$, (b) $\Delta = 20$, (c) $\lambda_2 = -2$, (d) $\lambda_{ci}^2 = 1.2$. The structures with $\omega'_x > 0$ are marked in red color; the structures with $\omega'_x < 0$ are marked in blue color. 70

Figure 5-22: Above wavy surface of artificial ripples with $ak = 0.2$: contours of Reynolds stress. (a) High intensity regions of $\langle -u'w' \rangle_2$ are denoted by the 0.0008 and 0.001 contour with solid and dotted lines, respectively; the purple arrow indicate the detection position for the QD-2 method. (b) High intensity regions of $\langle -u'w' \rangle_4$ are denoted by the 0.0008 and 0.001 contour with solid and dotted lines, respectively; the green arrow indicate the detection position for the QD-4 method. 74

Figure 5-23: Above wavy surface of artificial ripples with $ak = 0.2$: (a) oblique view, (b) side view and (c) top view of the conditionally averaged reversed



horseshoe vortex by QD-4 sampling method. The detection threshold is chosen to be 5 and the structures are represented by the isosurface of $\lambda_{ci}^2 = 2.625$. The structures with $\omega'_x > 0$ are marked in red color; the structures with $\omega'_x < 0$ are marked in blue color. 75

Figure 5-24: Above wavy surface of artificial ripples with $ak = 0.2$: (a) oblique view , (b) side view and (c) top view of the conditionally averaged quasistreamwise vortex by QD-2 sampling method. The detection threshold is chosen to be 3 and the structures are represented by the isosurface of $\lambda_{ci}^2 = 1.76$. The structures with $\omega'_x > 0$ are marked in red color; the structures with $\omega'_x < 0$ are marked in blue color. 76

Figure 5-25: Above wavy surface of artificial ripples with $ak = 0.2$: (a) oblique view , (b) side view and (c) top view of the conditionally averaged reversed horseshoe vortex by VISA sampling method. The detection threshold is chosen to be 1.5 and the structures are represented by the isosurface of $\lambda_{ci}^2 = 0.5$. The structures with $\omega'_x > 0$ are marked in red color; the structures with $\omega'_x < 0$ are marked in blue color. 77

Figure 5-26: Above wavy surface of simulated ripples with $ak = 0.2$, time sequence = 05: contours of Reynolds stress. (a) High intensity regions of $\langle -u'w' \rangle_2$ are denoted by the 0.0008 and 0.001 contour with solid and dotted lines, respectively; the purple arrow indicate the detection position for the QD-2 method. (b) High intensity regions of $\langle -u'w' \rangle_4$ are denoted by the 0.0008 and 0.001 contour with solid and dotted lines, respectively; the green arrow indicate the detection position for the QD-4 method. 78

Figure 5-27: Above wavy surface of simulated ripples with $ak = 0.3$, time sequence = 05: (a) oblique view , (b) side view and (c) top view of the conditionally averaged reversed horseshoe vortex by QD-4 sampling method. The detection threshold is chosen to be 10 and the structures are represented by the isosurface of $\lambda_{ci}^2 = 5$. The structures with $\omega'_x > 0$ are marked in red color; the structures with $\omega'_x < 0$ are marked in blue color. 79

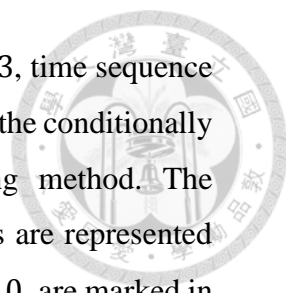


Figure 5-28: Above wavy surface of simulated ripples with $ak = 0.3$, time sequence = 05: (a) oblique view , (b) side view and (c) top view of the conditionally averaged quasistreamwise vortex by QD-2 sampling method. The detection threshold is chosen to be 2 and the structures are represented by the isosurface of $\lambda_{ci}^2 = 1$. The structures with $\omega'_x > 0$ are marked in red color; the structures with $\omega'_x < 0$ are marked in blue color. 80

Figure 5-29: Above wavy surface of simulated ripples with $ak = 0.3$, time sequence = 05: (a) oblique view , (b) side view and (c) top view of the conditionally averaged reversed horseshoe vortex by VISA sampling method. The detection threshold is chosen to be 6 and the structures are represented by the isosurface of $\lambda_{ci}^2 = 0.45$. The structures with $\omega'_x > 0$ are marked in red color; the structures with $\omega'_x < 0$ are marked in blue color. 81

List of tables



Table 2-1:	Vortex identification methods.....	9
Table 2-2:	Physical meaning of Q , Δ , λ_2 and λ_{ci} criterions.....	19

Chapter 1.

Introduction

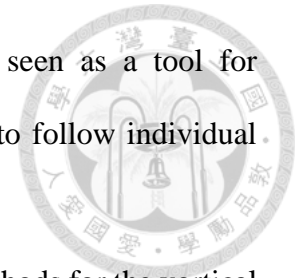


1.1 Research background and objectives

During the past decades, coherent vortical structures in the wall-bounded turbulent flow have been the subject of considerable interest among researchers. In the experiments of wall-bounded turbulent flow, researchers attributed the streaks to the swirling motions of vortical structures, which bring the slow-moving fluids away from the wall and the fast-moving fluids towards the wall. There was no concrete definition for a vortical structure (vortex) until Robinson (1991) proposed the following definition: *A vortex exists when instantaneous streamlines mapped onto a plane normal to the vortex core exhibit a roughly circular or spiral pattern, when viewed from a reference frame moving with the center of the vortex core.*

Robinson also proposed two conceptual models of vortical structures in wall-bounded turbulent flow. Therefore, many methods and techniques were developed to study vortical structures in wall-bounded turbulent flow. Conditional averaging method was used to reduce noise and educe the specific vortical structures (e.g. Willmarth & Lu 1972; Wallace *et.al.* 1972; Blackwelder & Kaplan 1976; Kim 1983). Moin and Kim (1985) took statistics of vorticity inclination angle in different depth in order to realize the dominant vorticity direction in the turbulent flow. To visualize the vortical structures, some researchers observed the vorticity isosurface and vortex lines; nevertheless, such methods are inadequate and can be misleading, vortex identification methods (e.g. Hunt *et.al.* 1988; Chong, Perry & Cantwell 1990; Jeong & Hussain 1995; Zhou *et.al.* 1999)

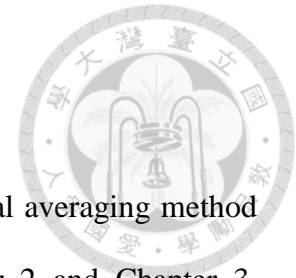
were then proposed. Identification of vortical structures can be seen as a tool for understanding complex flow phenomena, for example, being able to follow individual vortical structure in a turbulent flow throughout their lifetimes.



The aim of this thesis is to investigate and compare existing methods for the vortical structure identification methods, as well as applying to our numerical simulation. Moreover, the relations between these identification methods and previous methods such as vorticity inclination angle and vortex lines are of interest. To educe the specific vortical structures, conditional averaging method is also investigated and applied. The methods implemented for this Master's thesis have been programmed in FORTRAN.

1.2 Outline of this thesis

This thesis is structured in the following sequence. Conditional averaging method and the vortex identification methods are introduced in Chapter 2 and Chapter 3, respectively. In Chapter 4, we present the coherent vortical structures beneath free-propagating wavy surface, as well as investigate the relation between vorticity inclination angle and vortical structures. In Chapter 5, the coherent vortical structures, the regeneration of horseshoe vortices, as well as the discovery of the larger scale vortical motions above wavy surface are presented; in addition, the coherent vortical structures are also investigated through conditional averaging technique. Eventually, conclusions are drawn in Chapter 6.





Chapter 2.

Conditional averaging method



The basic concepts of the conditional averaging method are conditional sampling technique and ensemble average. To single out the coherent vortical structures associated with the bursting events from the near-wall chaotic turbulent flow, several conditional sampling methods were developed. Willmarth and Lu (1972) and Wallace et al. (1972) introduced the quadrant analysis. Based on the well-developed variable-interval time-averaging (VITA) sampling technique of Blackwelder and Kaplan (1976), Kim (1983) proposed the variable-interval space-averaging (VISA) sampling technique. The detail of ensemble averaging procedure is introduced in section 5.3.1.

Kim and Moin (1986) used VISA sampling technique and quadrant analysis as conditions to obtain ensemble-averaged vorticity lines in a large eddy simulation (LES) of a low-Reynolds number turbulent channel flow. In our study, we also use both of the sampling methods as conditions. In section 2.1 and 2.2 the quadrant analysis and the VISA sampling technique are described, respectively.



2.1 Quadrant analysis

Previous research of wall-bounded turbulence indicated that the near-wall coherent structures are often associated with the turbulence motion of “sweeps” and “ejections”. Ejection and sweep events are defined as second ($u' < 0, w' > 0$) and fourth ($u' > 0, w' < 0$) quadrant motions, as Figure 2-1 shows. To detect the ejection and sweeping events, Willmarth and Lu (1972) and Wallace et al. (1972) applied the quadrant analysis. The original method was designed for velocity signals measured by experiments; to apply it to the numerical simulation, as Kim and Moin (1986), the detection criterion of the second quadrant analysis can be written as

$$D(x, y, z, t_0) = 1, \quad \text{if } u' < 0, w' > 0 \text{ and } \frac{u'w'}{\langle u'w' \rangle_{xy}} > k, \quad (2-1)$$
$$= 0, \quad \text{otherwise}$$

and the fourth quadrant analysis can be written as

$$D(x, y, z, t_0) = 1, \quad \text{if } u' > 0, w' < 0 \text{ and } \frac{u'w'}{\langle u'w' \rangle_{xy}} > k, \quad (2-2)$$
$$= 0, \quad \text{otherwise}$$

where k is the threshold level and $\langle \quad \rangle_{xy}$ is the average over the (x, y) -plane. With quadrant analysis, vortical structures related to the ejection and sweep events can be separated. In the remainder of this paper, the second and fourth quadrant analysis will be referred to as QD-2 and QD-4 respectively.

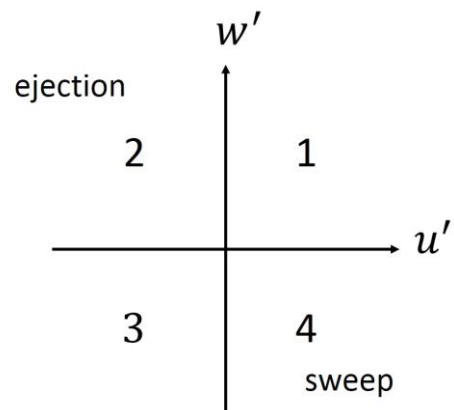


Figure 2-1: Quadrant of instantaneous (u', w') -plane, u' and w' is the streamwise and spanwise turbulent velocity, respectively.

2.2 VISA sampling technique



For numerical simulation, the variable-interval space-averaging (VISA) by Kim (1983) is defined as,

$$\hat{u}(x, y, z, t_0, L) = \frac{1}{L} \int_{x-\frac{1}{2}L}^{x+\frac{1}{2}L} u(\xi, y, z, t_0) d\xi, \quad (2-3)$$

where u is the streamwise velocity, L is the width of the spatial averaging and (x, y, z) is the position and t_0 is the time step at which sampling occurred. If averaged in two directions, the function can be express as,

$$\hat{u}(x, y, z, t_0, L_x, L_y) = \frac{1}{L_x L_y} \int_{x-\frac{1}{2}L_x}^{x+\frac{1}{2}L_x} \int_{y-\frac{1}{2}L_y}^{y+\frac{1}{2}L_y} u(\xi, \zeta, z, t_0) d\xi d\zeta, \quad (2-4)$$

where L_x and L_y are the widths of the averaging window along the streamwise and spanwise directions respectively. The value of L_x and L_y should be determined by scale of the event. In this paper, we use $L_x = 15\Delta x$ and $L_y = 15\Delta y$. To identify strong events, a localized variance is introduced with

$$var = u^2 - \hat{u}^2. \quad (2-5)$$

Strong sweeping events are detected using the following criterion,

$$D(x, y, z, t_0) = \begin{cases} 1, & \text{if } var > k \cdot u_{r.m.s.}^2 \text{ and } \frac{\partial u}{\partial x} < 0. \\ 0, & \text{otherwise} \end{cases} \quad (2-6)$$

The detection function $D = 1$ if the event exists. $u_{r.m.s.}$ is the root-mean-square variation of u at the horizontal plane and k is the threshold level.

Chapter 3.

Vortex identification methods



Vortical structures have been investigated by numerous researchers, using different techniques and methods. In the following sections, we provide an overview of four popular schemes for vortex identification, shown in Table 3-1. All of the four criteria are based on the local analysis of the velocity gradient tensor, thereby making them Galilean invariant. The results of the four methods are shown in the following chapters.

Year	Criterion	Proposer
1988	Q Criterion	Hunt et al.
1990	Δ Criterion	Chong & Perry
1995	λ_2 Criterion	Jeong & Hussain
1999	λ_{ci} Criterion	Zhou et al.

Table 3-1: Vortex identification methods.



3.1 Q Criterion

Hunt et al. (1988) defined an eddy zone as the region characterized by positive second invariant Q of the velocity gradient, i.e. $Q > 0$. Additionally, the pressure in the eddy zone should be lower than the ambient pressure. Jeong and Hussain (1995) shown that the additional low pressure condition is subsumed by $Q > 0$.

The velocity gradient is given by

$$\nabla \mathbf{u} = u_{i,j} = \begin{bmatrix} \frac{\partial u_1}{\partial x_1} & \frac{\partial u_1}{\partial x_2} & \frac{\partial u_1}{\partial x_3} \\ \frac{\partial u_2}{\partial x_1} & \frac{\partial u_2}{\partial x_2} & \frac{\partial u_2}{\partial x_3} \\ \frac{\partial u_3}{\partial x_1} & \frac{\partial u_3}{\partial x_2} & \frac{\partial u_3}{\partial x_3} \end{bmatrix}, \quad (3-1)$$

and the characteristic equation of $\nabla \mathbf{u}$

$$\det(u_{i,j} - \sigma \mathbf{I}) = 0, \quad (3-2)$$

$$\sigma^3 + P\sigma^2 + Q\sigma + R = 0, \quad (3-3)$$

where σ is the eigenvalue and

$$P = -u_{i,i}, \quad (3-4)$$

$$Q = \frac{1}{2}(u_{i,i}^2 - u_{i,j}u_{j,i}), \quad (3-5)$$

$$R = -\det(u_{i,j}), \quad (3-6)$$

are the invariants of the velocity gradient tensor.

In the case of incompressible flow,

$$P = -u_{i,i} = 0, \quad (3-7)$$

and decompose the velocity gradient tensor into strain rate tensor and rotation tensor, i.e.

$u_{i,j} = S_{ij} + \Omega_{ij}$, where $S_{ij} = \frac{1}{2}(u_{i,j} + u_{j,i})$ and $\Omega_{ij} = \frac{1}{2}(u_{i,j} - u_{j,i})$, the second invariant becomes

$$Q = \frac{1}{2}(u_{i,i}^2 - u_{i,j}u_{j,i}) = -\frac{1}{2}u_{i,j}u_{j,i} = \frac{1}{2}(\|\Omega\|^2 - \|S\|^2), \quad (3-8)$$

where $\|\Omega\| = \sqrt{\sum_i \sum_j \Omega_{ij}^2}$ is the Frobenius norm. Thus, Q represents the local balance between vorticity magnitude and shear strain rate. That is to say, when Q is positive, the term of vorticity magnitude dominates.



3.2 Δ Criterion

Using critical point theory, Chong and Perry (1990) defined a vortex core to be the region where velocity gradient has complex eigenvalues. In local coordinate, the reference frame is moving with the fluid particle, hence the velocities at original point are zero. The velocities at a local coordinate system can be represented as a set of differential equations

$$\frac{d}{dt} \begin{Bmatrix} x_1 \\ x_2 \\ x_3 \end{Bmatrix} = \begin{Bmatrix} u_1 \\ u_2 \\ u_3 \end{Bmatrix} = \begin{bmatrix} \frac{\partial u_1}{\partial x_1} & \frac{\partial u_1}{\partial x_2} & \frac{\partial u_1}{\partial x_3} \\ \frac{\partial u_2}{\partial x_1} & \frac{\partial u_2}{\partial x_2} & \frac{\partial u_2}{\partial x_3} \\ \frac{\partial u_3}{\partial x_1} & \frac{\partial u_3}{\partial x_2} & \frac{\partial u_3}{\partial x_3} \end{bmatrix} \begin{Bmatrix} x_1 \\ x_2 \\ x_3 \end{Bmatrix}. \quad (3-9)$$

The general solution is

$$\mathbf{x} = c_1 \mathbf{V}_1 e^{\lambda_1 t} + c_2 \mathbf{V}_2 e^{\lambda_2 t} + c_3 \mathbf{V}_3 e^{\lambda_3 t}, \quad (3-10)$$

where c_1 , c_2 and c_3 are constant, \mathbf{V}_1 , \mathbf{V}_2 and \mathbf{V}_3 are eigenvectors of $\nabla \mathbf{u}$, λ_1 , λ_2 and λ_3 are eigenvalues of $\nabla \mathbf{u}$. By the phase plane method and critical point theory (Appendix A.), the local streamline pattern demonstrates a spiral or center phase portrait when the linear system of differential equations has complex eigenvalues. Then the characteristic equation of $\nabla \mathbf{u}$ is same as (3-3) and (3-4)-(3-6) are the invariants of the velocity gradient tensor. To determine the solution type, use the discriminant of the characteristic equation

$$\Delta = \left(-\frac{P^3}{27} - \frac{R}{2} + \frac{PQ}{6} \right)^2 + \left(\frac{Q}{3} - \frac{P^2}{9} \right)^3. \quad (3-11)$$

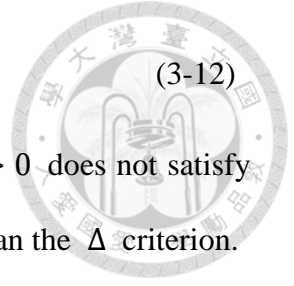
The condition $\Delta > 0$ implies that $\nabla \mathbf{u}$ has complex eigenvalues.

Chakraborty et al. (2005) analyzed that for incompressible flow, the first invariant becomes zero, as (3-7). Then, the discriminant can be written as

$$\Delta = \left(\frac{1}{2}R\right)^2 + \left(\frac{1}{3}Q\right)^3.$$

(3-12)

It can be seen that when $Q > 0$, Δ must be positive. However, $\Delta > 0$ does not satisfy the condition of $Q > 0$. Thus, the Q criterion is more restrictive than the Δ criterion.





3.3 λ_2 Criterion

Jeong and Hussain (1995) discussed the inadequacies of intuitive indicators of vortices: local pressure minimum, pathline and streamline, and vorticity magnitude. The existence of a pressure minimum and a vortex core are inconsistent due to unsteady straining and viscous effects. Unsteady straining can create a pressure minimum without vortical or swirling motion. Viscous effects can reduce the pressure minimum in a flow with vortical motion.

To improve the inadequate concept of pressure minimum, Jeong and Hussain proposed a new detection criterion for a vortex core. Pressure minimum can be obtained from the Hessian of pressure ($p_{,ij}$)

$$p_{,ij} = \begin{bmatrix} \frac{\partial^2 p}{\partial x \partial x} & \frac{\partial^2 p}{\partial x \partial y} & \frac{\partial^2 p}{\partial x \partial z} \\ \frac{\partial^2 p}{\partial y \partial x} & \frac{\partial^2 p}{\partial y \partial y} & \frac{\partial^2 p}{\partial y \partial z} \\ \frac{\partial^2 p}{\partial z \partial x} & \frac{\partial^2 p}{\partial z \partial y} & \frac{\partial^2 p}{\partial z \partial z} \end{bmatrix}, \quad (3-13)$$

which is derived from the gradient of the Navier-Stokes equation. The Navier-Stokes equation can be written in tensor form as

$$\frac{\partial u_i}{\partial t} + u_k u_{i,k} = -\frac{1}{\rho} p_{,i} + \nu u_{i,kk}. \quad (3-14)$$

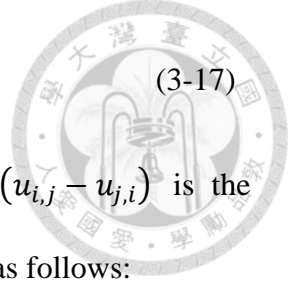
Taking the gradient of the Navier-Stokes equation,

$$\frac{\partial u_{i,j}}{\partial t} + u_{k,j} u_{i,k} + u_k u_{i,jk} = -\frac{1}{\rho} p_{,ij} + \nu u_{i,jkk}, \quad (3-15)$$

the first two terms can be substituted by material derivative as

$$\frac{Du_{i,j}}{Dt} + u_{k,j} u_{i,k} = -\frac{1}{\rho} p_{,ij} + \nu u_{i,jkk}, \quad (3-16)$$

where $p_{,ij}$ is a Hessian matrix, which is always symmetric. Then, (3-16) can be decomposed into symmetric and antisymmetric part by



$$u_{i,j} = S_{ij} + \Omega_{ij}, \quad (3-17)$$

where $S_{ij} = \frac{1}{2}(u_{i,j} + u_{j,i})$ is the strain rate tensor and $\Omega_{ij} = \frac{1}{2}(u_{i,j} - u_{j,i})$ is the rotation tensor. Hence, the left-hand side of (3-16) can be expressed as follows:

$$\begin{aligned} \frac{Du_{i,j}}{Dt} + u_{k,j}u_{i,k} &= \frac{D(S_{i,j} + \Omega_{i,j})}{Dt} + (S_{jk} - \Omega_{jk})(S_{ik} + \Omega_{ik}) \\ &= \frac{D(S_{i,j} + \Omega_{i,j})}{Dt} + S_{ik}S_{jk} + S_{jk}\Omega_{ik} - S_{ik}\Omega_{jk} - \Omega_{ik}\Omega_{jk} \\ &= \left[\frac{DS_{i,j}}{Dt} + \Omega_{ik}\Omega_{kj} + S_{ik}S_{kj} \right] + \left[\frac{D\Omega_{i,j}}{Dt} + \Omega_{ik}S_{kj} + S_{ik}\Omega_{kj} \right]. \end{aligned} \quad (3-18)$$

The right-hand side of (3-16) can be expressed as follows:

$$-\frac{1}{\rho}p_{,ij} + \nu u_{i,jkk} = \left[-\frac{1}{\rho}p_{,ij} + \nu S_{ij,kk} \right] + \nu [\Omega_{ij,kk}]. \quad (3-19)$$

Both in (3-18) and (3-19), the first square brackets include symmetric parts and the second square brackets include antisymmetric parts. Since the pressure Hessian is symmetric, consider the symmetric part of (3-16)

$$\frac{DS_{i,j}}{Dt} + \Omega_{ik}\Omega_{kj} + S_{ik}S_{kj} - \nu S_{ij,kk} = -\frac{1}{\rho}p_{,ij}. \quad (3-20)$$

The term $\frac{DS_{i,j}}{Dt}$ represents the unsteady irrotational straining and $\nu S_{ij,kk}$ represents viscous effect. By neglecting these two terms as discussed above, (3-20) becomes

$$\mathbf{S}^2 + \mathbf{\Omega}^2 = -\frac{1}{\rho}p_{,ij}, \quad (3-21)$$

where $\mathbf{S}^2 + \mathbf{\Omega}^2 = \Omega_{ik}\Omega_{kj} + S_{ik}S_{kj}$. Note that $\mathbf{S}^2 + \mathbf{\Omega}^2$ is symmetric, all its eigenvalues are real.

The condition of local pressure minimum in a plane can be satisfied by a saddle point which includes a local maximum along an axial direction and two local minimums along the crossing axes. By the properties of the Hessian matrix (Appendix B.), the condition occurs when the tensor $p_{,ij}$ has two positive eigenvalues, which corresponds to a saddle

point. In two dimension, a saddle point will always occur at a relative minimum along one axial direction and at a relative maximum along the crossing axis. In three dimension, we want to find a point which is a local minimum in a plane, that is, a saddle point with two local minimum. Take a simple function with two local minimum for example:

$$f = x^2 + y^2 - z^2. \quad (3-22)$$

Its Hessian matrix at a point (X, Y, Z)

$$H = \begin{bmatrix} 2 & 0 & 0 \\ 0 & 2 & 0 \\ 0 & 0 & -2 \end{bmatrix}, \quad (3-23)$$

and its eigenvalues

$$\lambda = 2, 2, -2. \quad (3-24)$$

In this case, it has a local minimum in (x, y) -plane. Therefore, we get two positive eigenvalues to satisfy the condition.

In conclusion, two negative eigenvalues of $\mathbf{S}^2 + \mathbf{\Omega}^2$ are required, which equivalent to $\lambda_2 < 0$. (Assume λ_2 is the second largest eigenvalue of $\mathbf{S}^2 + \mathbf{\Omega}^2$)



3.4 λ_{ci} Criterion

Based on the Δ criterion, Zhou et al. (1999) proposed ‘swirling strength’ criterion, using the imaginary part of complex conjugate eigenvalue of velocity gradient tensor to identify vortices. In Cartesian coordinates, the velocity gradient $\nabla\mathbf{u}$ can be decomposed by diagonalization

$$\nabla\mathbf{u} = [\mathbf{v}_r \quad \mathbf{v}_{cr} \quad \mathbf{v}_{ci}] \begin{bmatrix} \lambda_r & 0 & 0 \\ 0 & \lambda_{cr} & \lambda_{ci} \\ 0 & -\lambda_{ci} & \lambda_{cr} \end{bmatrix} [\mathbf{v}_r \quad \mathbf{v}_{cr} \quad \mathbf{v}_{ci}]^{-1}, \quad (3-25)$$

where λ_r is the real eigenvalue corresponding with a real eigenvector V_r , and $\lambda_{cr} \pm i\lambda_{ci}$ are the conjugate pairs of the complex eigenvalues corresponding with complex eigenvectors $V_{cr} \pm iV_{ci}$.

In a locally curvilinear coordinate system (x_1, x_2, x_3) spanned by eigenvectors (v_r, v_{cr}, v_{ci}) , the local streamline can be expressed as

$$x_1(t) = c_r e^{\lambda_r t}, \quad (3-26)$$

$$x_2(t) = e^{\lambda_{cr} t} \left[c_c^{(1)} \cos(\lambda_{ci} t) + c_c^{(2)} \sin(\lambda_{ci} t) \right], \quad (3-27)$$

$$x_3(t) = e^{\lambda_{cr} t} \left[c_c^{(2)} \cos(\lambda_{ci} t) - c_c^{(1)} \sin(\lambda_{ci} t) \right], \quad (3-28)$$

where c_r , $c_c^{(1)}$ and $c_c^{(2)}$ are constants.

Equation (3-26) represents stretching or compressing of the local flow along the v_r axis, while (3-27) and (3-28) shows that on the plane spanned by v_{cr} and v_{ci} , the flow is swirling. Hence, the swirling strength, determined by λ_{ci} , is a measure of the local swirling rate inside the vortex, and the strength of stretching or compression is given by λ_r . In particular, the vortical structures are extracted by plotting isosurfaces of λ_{ci}^2 , since the term λ_{ci}^2 is similar to enstrophy, and it is also dimensionally consistent with other quantities such as Q used previously in the vortices identification.



3.5 Relation between Q , Δ , λ_2 and λ_{ci}

The physical meanings of Q , Δ , λ_2 and λ_{ci} magnitude are listed in Table 3-2. It is observed that all criterions represent strength of the vortex except the Δ criterion. Hereinafter, we arrange some results proposed by former researchers.

Jeong and Hussain (1995) discussed the relation between λ_2 criterion and Q criterion, “In summary, the Q - and λ_2 -definitions tend to be similar but often differ from the Δ -definitions.” As we elaborated in Chapter 2.1.2, Chakraborty et al. (2005) and Jeong and Hussain are on the same page. On the other hand, Zhou et al. (1999) commented that “The term λ_{ci}^2 is dimensionally consistent with other quantities such as Q used previously in the identification of vortices.” In conclusion, Q , Δ , and λ_2 criterion tend to be similar.

In 2005, Chakraborty et al. observed that inside the intense vortical structure, four methods have equivalent thresholds, such as

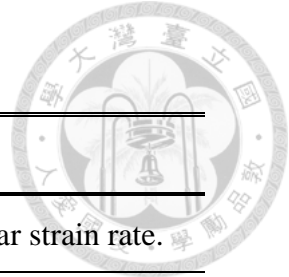
$$\lambda_{ci} \geq (\lambda_{ci})_{th} = \varepsilon, \quad (3-29)$$

$$Q \geq Q_{th} = \varepsilon^2, \quad (3-30)$$

$$\Delta \geq \Delta_{th} = \frac{1}{27} \varepsilon^6, \quad (3-31)$$

$$\lambda_2 \leq (\lambda_2)_{th} = -\varepsilon^2, \quad (3-32)$$

where $()_{th}$ is the threshold of the criterion and ε is the threshold value of λ_{ci} criterion. Note that these equivalent equations are non-optimal and can be modified in different flow cases. The results of applying the equivalent thresholds to our numerical simulation are presented in section 4.2.1 and 5.2.1.



Criteria	Physical meaning
$Q > 0$	Balance between vorticity magnitude and shear strain rate.
$\Delta > 0$	Positive determinant represents spiral trajectory.
$\lambda_2 < 0$	Decreasing negative λ_2 values correspond to increasing vortex strength.
$\lambda_{ci} > 0$	Swirling strength of the vortex.

Table 3-2: Physical meaning of Q , Δ , λ_2 and λ_{ci} criterions.





Chapter 4.

Coherent vortical structures beneath free-propagating wavy surface

4.1 Numerical simulation

The details of the numerical model studied in this chapter are reported in Tsai (2015). Direct numerical simulation (DNS) is performed in a fixed coordinate system for the region encountering the passage of non-breaking surface waves without surface tension. We consider a gravity wave with a wavelength of $\lambda = 7.5\text{cm}$ as well as initial wave steepness $ak = 0.25$, where a is the gravity wave amplitude and $k = 2\pi/\lambda$ is the wave number. The length, width and depth of the computational domain are 4λ , 2λ and 0.8λ , respectively, discretized by 512, 256 and 129 grids. In addition, the computational domain is closed in the horizontal directions by periodic conditions, and in the vertical direction by free surface boundary at the top and the free-slip boundary on the bottom. The spatial-differential operators with respect to horizontal direction are approximated by the pseudo-spectral method, and the operators with respect to vertical direction are approximated by the second-order finite-difference scheme.

In the present study, since the flow is dominated by the motions of surfaces wave, the flow variable f can be decomposed as

$$f(x, y, z, t) = \bar{f}(z, t) + \tilde{f}(x, z, t) + f'(x, y, z, t), \quad (4-1)$$

$$\tilde{f}(x, z, t) = \langle f(x, z, t) \rangle_y - \bar{f}(z, t), \quad (4-2)$$

where $\bar{f}(z, t)$ is the average over the (x, y) -plane and $\tilde{f}(x, z, t)$ is the wave-correlated component, $\langle f(x, z, t) \rangle_y$ is the phase average over spanwise y , and $f'(x, y, z, t)$ is the turbulent component. Hence the turbulent component can be written as

$$f'(x, y, z, t) = f(x, y, z, t) - \langle f(x, z, t) \rangle_y. \quad (4-3)$$

4.2 Results of vortical structure identification



4.2.1 Equivalent thresholds

In section 3.5, we introduced the equivalent thresholds for intense vortical structures proposed by Chakraborty et al. Hereinafter, we apply the equivalent thresholds to the numerical simulation.

After the application of the vortex identification methods, a flow field full of turbulent structures appears. To test the influence of different ε , two value $\varepsilon^2 = 0.001$ and $\varepsilon^2 = 0.003$ are given experimentally and the results are respectively shown in Figure 4-1 and Figure 4-2. Note that the value of ε represents the isosurface of vortical structures. The isosurface is a surface that represents points of a constant value within a volume of space. Both figures obviously show that four methods give similar results, demonstrating the equivalent equations proposed by Chakraborty et al.

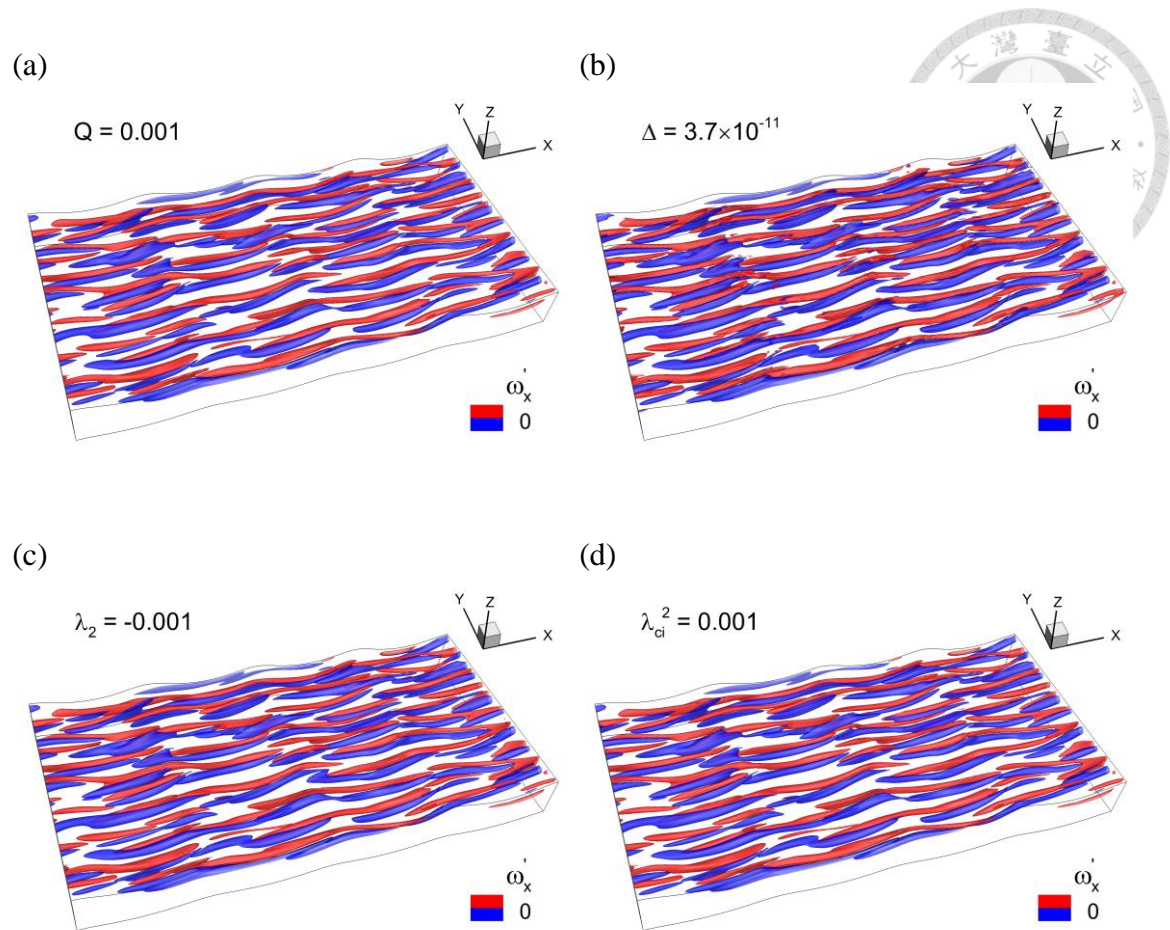


Figure 4-1: Vortical structures beneath free-propagating wavy surface. The vortical structures are represented by the isosurface of (a) $Q = 0.001$, (b) $\Delta = 3.7 \times 10^{-11}$, (c) $\lambda_2 = -0.001$, (d) $\lambda_{ci}^2 = 0.001$. The structures with $\omega'_x > 0$ are marked in red color; the structures with $\omega'_x < 0$ are marked in blue color.

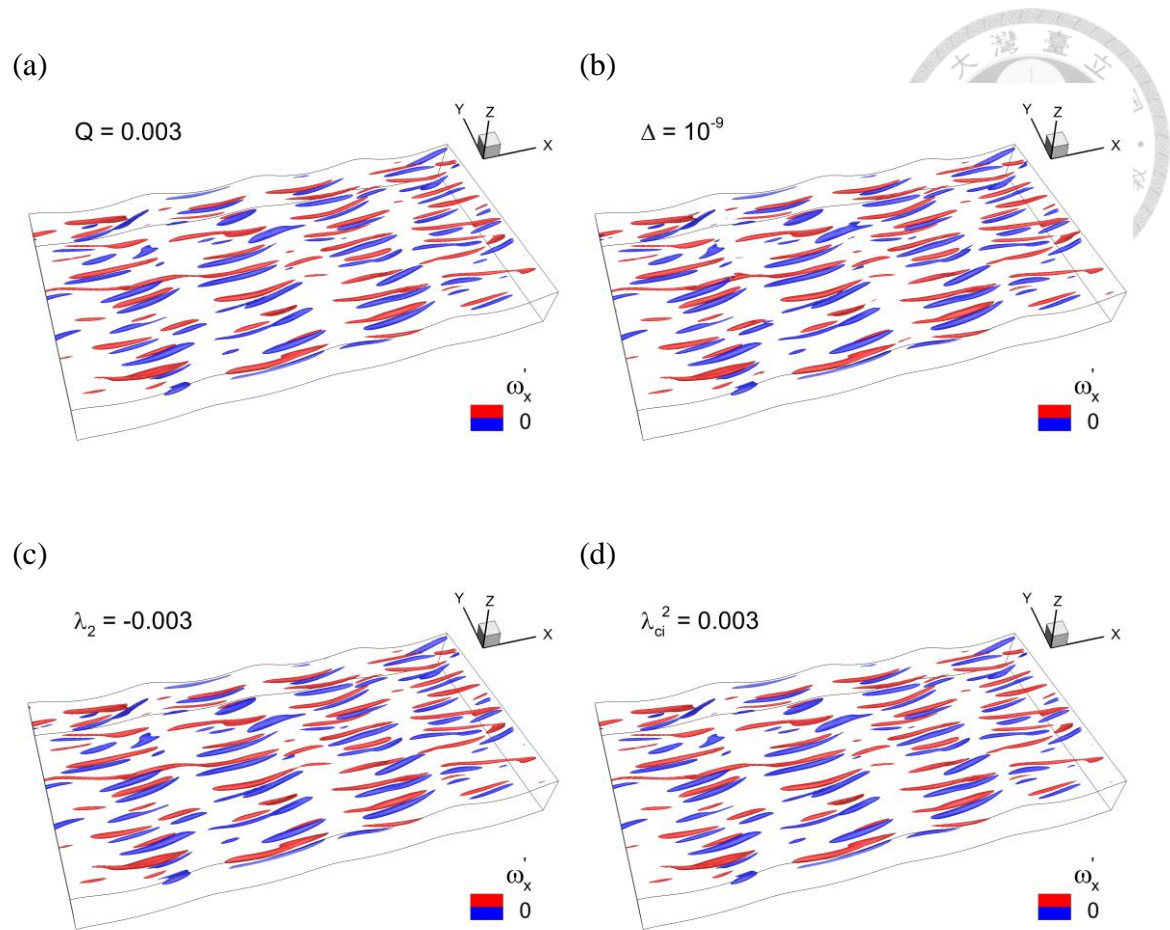


Figure 4-2: Vortical structures beneath free-propagating wavy surface. The vortical structures are represented by the isosurface of (a) $Q = 0.003$, (b) $\Delta = 10^{-9}$, (c) $\lambda_2 = -0.003$, (d) $\lambda_{ci}^2 = 0.003$. The structures with $\omega'_x > 0$ are marked in red color; the structures with $\omega'_x < 0$ are marked in blue color.

4.2.2 Vortical structures

To reveal the vortical structures in the turbulent flow, we adjust value of the isosurface and observe the variation of structures. Larger value of the isosurface representing stronger vortical structure. In Figure 4-3(a), intense vortical structures exist at the backward face. As the value of the isosurface decreases, we observe that vortical structures appear in pairs with opposite streamwise turbulent vorticity and are elongated along the streamwise direction.

In the same case, Tsai et al. (2015) attributed the elongated streaks in temperature contour to the Langmuir circulations by observing the contour distributions of the turbulent velocities and streamwise vorticities. Such vortical motions can also be revealed by the vortex identification method, as shown in Figure 4-4. It is observed that the cool streak is always between a structure with $\omega'_x > 0$ at the left side and a structure with $\omega'_x < 0$ at the right side, in the streamwise direction; the position corresponds to the converging and vertical downward flow. On the contrary, the warm band is always between a structure with $\omega'_x < 0$ at the left side and a structure with $\omega'_x > 0$ at the right side, in the streamwise direction, the position corresponds to the diverging flow. In consequence, it is intuitive to reveal the vortical structures by using the vortex identification methods marked with sign of the vorticity.

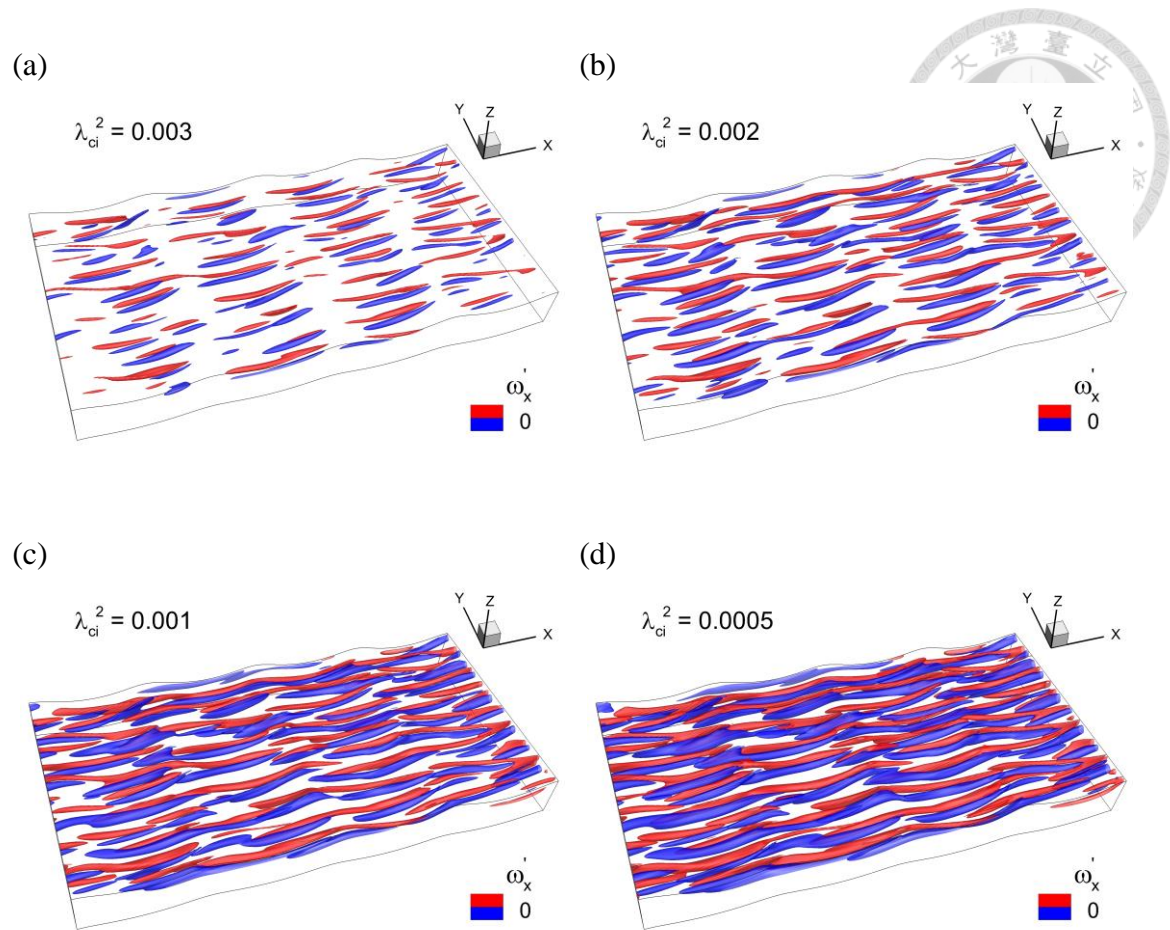


Figure 4-3: Vortical structures beneath free-propagating wavy surface. The vortical structures are represented by isosurface of (a) $\lambda_{ci}^2 = 0.003$, (b) $\lambda_{ci}^2 = 0.002$ (c) $\lambda_{ci}^2 = 0.001$, (d) $\lambda_{ci}^2 = 0.0005$. The structures with $\omega'_x > 0$ are marked in red color; the structures with $\omega'_x < 0$ are marked in blue color.

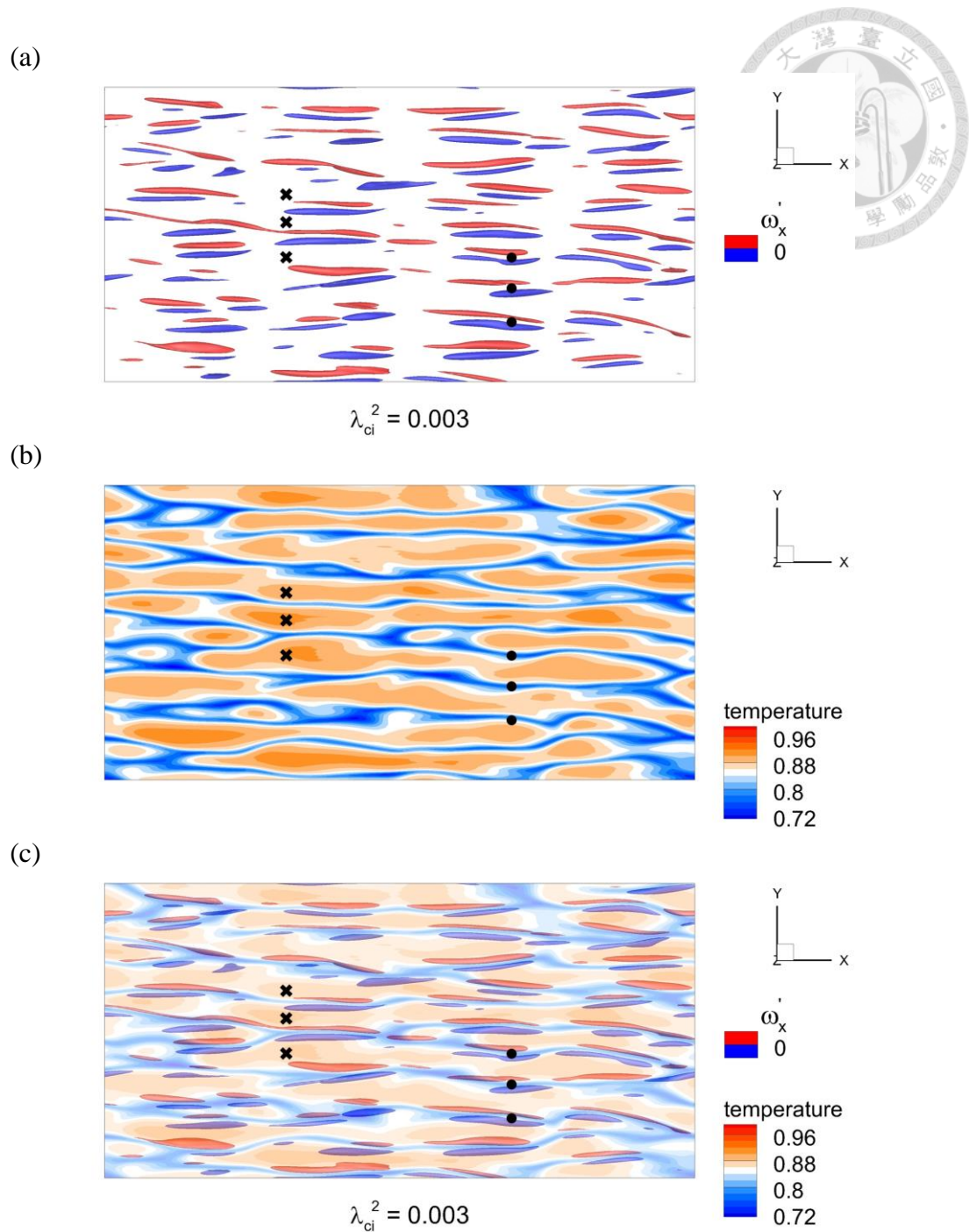


Figure 4-4: (a) The vortical structures beneath free-propagating wavy surface. (b) Temperature contour on the water surface. (c) Combination of (a) and (b). The wave propagates from left to right and the vortical structures are represented by isosurface of $\lambda_{ci}^2 = 0.003$. Examples of cool streaks and warm bands are marked by circular dots and cross signs, respectively. The structures with $\omega'_x > 0$ are marked in red color; the structures with $\omega'_x < 0$ are marked in blue color.

4.2.3 Relation between vorticity inclination angle and vortical structures



Moin and Kim (1985) used the statistics of vorticity inclination angle to represent the occurrence of horseshoe vortices in turbulent channel flow. In this study, the two-dimensional inclination angles of the projection of vorticity vectors in (x, y) - and (x, z) -planes are defined as $\theta = \tan^{-1}(\omega'_y/\omega'_x)$ and $\phi = \tan^{-1}(\omega'_z/\omega'_x)$, respectively, with the sign convention for the angles shown in Figure 4-5. The statistics of the inclination angles are weighted by the magnitudes of the projected vorticity vector,

$$\omega'_{xy} = \frac{\omega_x'^2 + \omega_y'^2}{\langle \omega_x'^2 + \omega_y'^2 \rangle_z}, \quad (4-4)$$

$$\omega'_{xz} = \frac{\omega_x'^2 + \omega_z'^2}{\langle \omega_x'^2 + \omega_z'^2 \rangle_z}, \quad (4-5)$$

where $\langle \rangle_z$ indicates average over the corresponding horizontal (x, y) -plane.

In our case, in order to study the relation between inclination angle and vortical structures, we compute the inclination angles in computational domain and focus on angles of the projection of vorticity vectors in (x, y) -plane. Figure 4-6(a)-(d) shows the probabilities of θ , and the probable structures suspected from Figure 4-6(a)-(d) are shown in Figure 4-6(e). From the histograms we can observe that two parallel vorticity vectors with opposite directions, which seem to be two legs of the structure, are located near wave surface, and the head part is located in deeper depth. Since the histograms are statistic results of vorticity inclination angle, it is reasonable that the speculation of the structures are different to the vortical structures drawn by isosurface of the identification methods.

Figure 4-7 shows vortex lines plotted by using the function of “streamtraces” in Tecplot. A vortex line is a line which is tangent to the local vorticity vector. Note that

these vortex lines are drawn by turbulent vorticities. For the hairpin-shaped vortex lines corresponding with cold streaks, their left and right legs merge into the vortical structures marked in positive and negative streamwise turbulent vorticity, respectively. Such vortex lines produce the ejecting flow from wave surface to the deeper water, causing the converging motion. Moreover, jet with fast-moving fluids is produced among those hairpin-shaped vortex lines, corresponding to the position of the cool streak. The statistic results of inclination angle contain only vortical structures if we filter the vorticity vectors with $\lambda_2 < 0$, thus the presumption structures are close to the identification results, which show elongated pairs with opposite streamwise turbulent vorticity vectors. The results are shown in Figure 4-8.

From the observation above, we can see that vortex lines can explain the physical phenomenon as well, though drawing vortex lines requires more skill and experience. In conclusion, it is important to study the turbulent flow by using vortex lines and vortical structures.

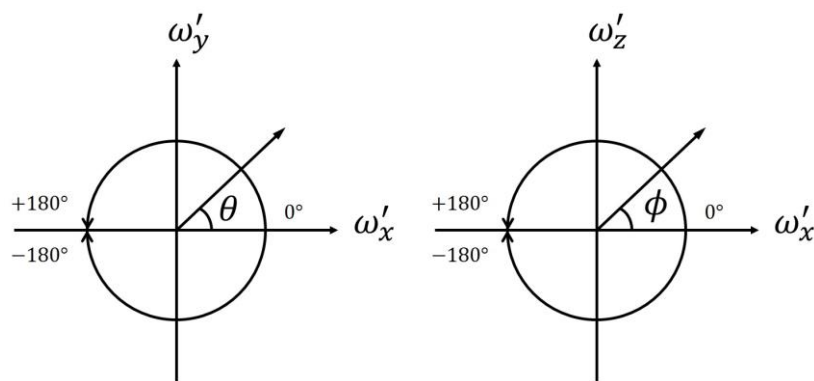


Figure 4-5: Sign convention for vorticity inclination angles θ and ϕ .

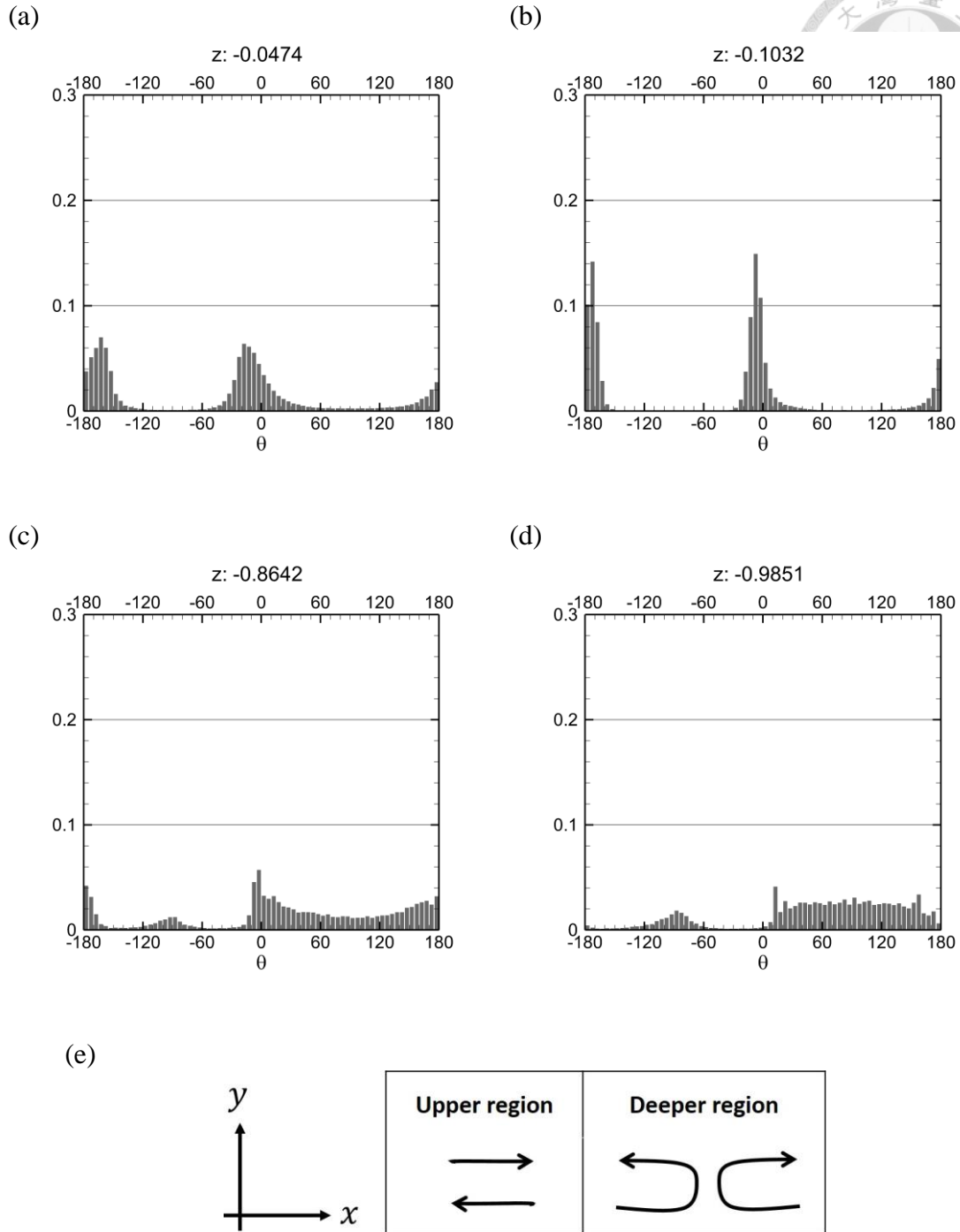


Figure 4-6: Distribution of the inclination angle of the projection of the vorticity vectors in (x, y) -planes; data weighted with the magnitude of the projected vorticity. (a) $z = -0.0474$; (b) -0.1032 ; (c) -0.8642 ; (d) -0.9851 . (e) Presumptions of the structures.

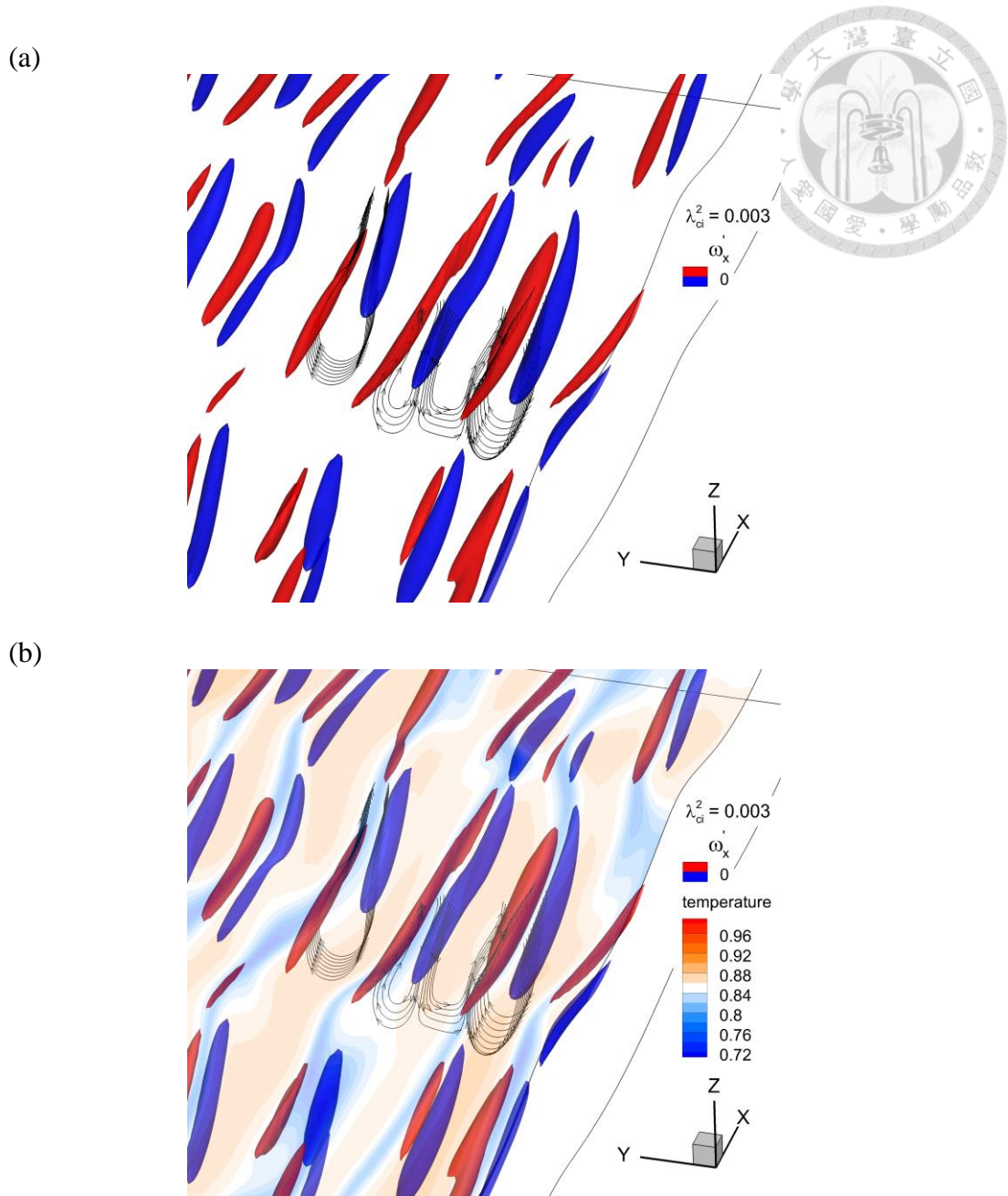


Figure 4-7: (a) Vortex lines among structures. (b) Vortex lines among structures and contour distribution of temperature on the water surface. The vortex lines are drawn with velocities fluctuation. The vortical structures are represented by isosurface of $\lambda_{ci}^2 = 0.003$.

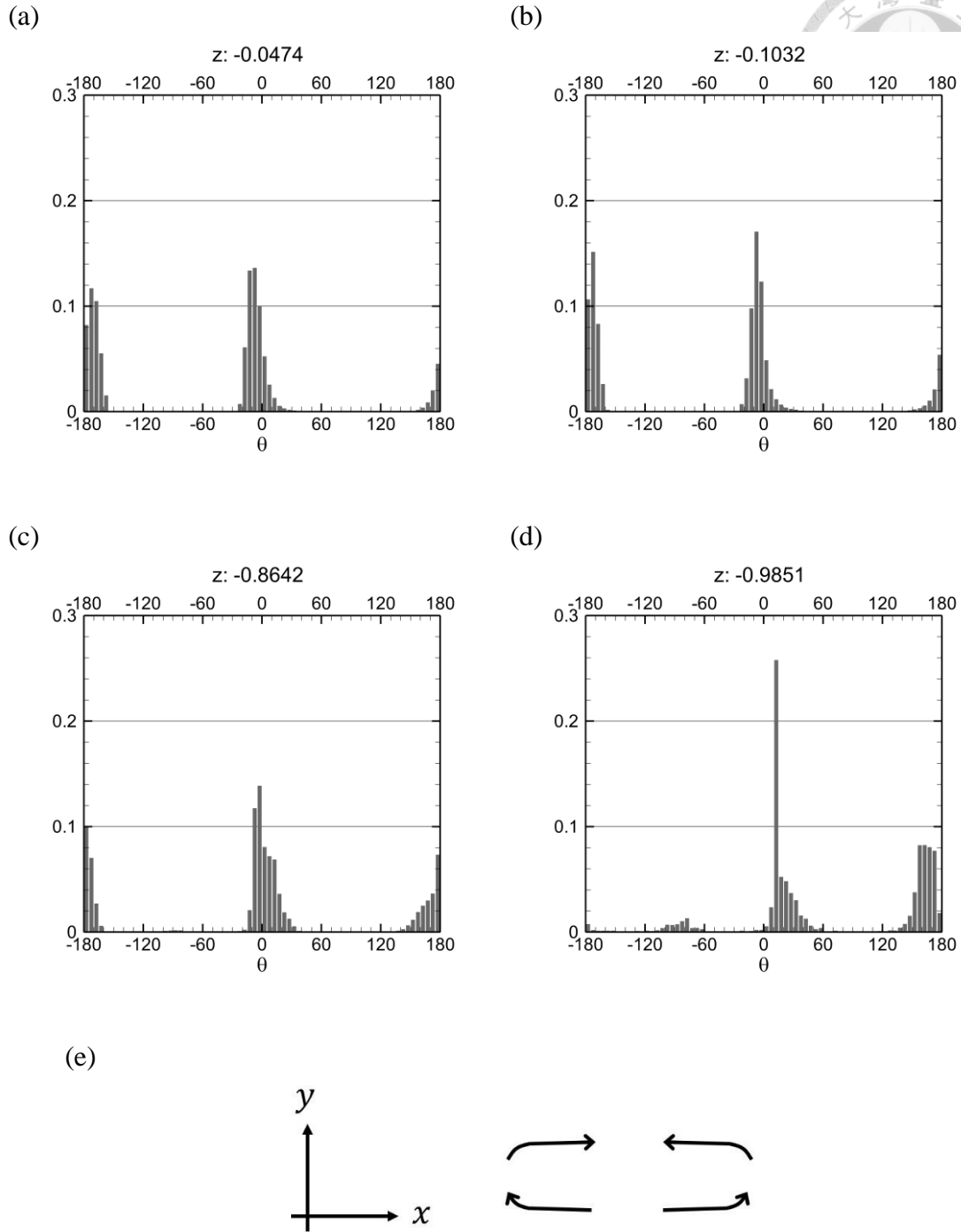


Figure 4-8: Distribution of the inclination angle of the projection of the vorticity vectors in (x, y) -planes; data weighted with the magnitude of the projected vorticity and filtered by $\lambda_2 < 0$. (a) $z = -0.0474$; (b) -0.1032 ; (c) -0.8642 ; (d) -0.9851 . (e) Presumptions of the structures.



Chapter 5.

Coherent vortical structures above wavy surface



5.1 Numerical simulation

The details of the numerical model studied in this chapter are reported in Druzhinin (2012). Direct numerical simulation (DNS) is performed in a reference frame moving with the wave phase velocity. The length, width and depth of the computational domain are 6λ , 4λ and λ , respectively, discretized by 360, 240 and 180 grids. In addition, the wind flow is assumed to be periodical in horizontal directions. A no-slip boundary condition is considered at the lower boundary, as well as a no-slip boundary condition is prescribed at the upper horizontal plane which is assumed to be moving with bulk velocity U_0 in the x direction.

The variables are transformed from the Cartesian frame (x, z) into a curvilinear coordinate system (ξ, η) defined by a conformal mapping

$$x = \xi - ae^{-k\eta} \sin k\xi, \quad (5-1)$$

$$z = \eta + ae^{-k\eta} \cos k\xi. \quad (5-2)$$

In addition, a mapping is employed over the vertical coordinate η as

$$\eta = 0.5 \left(1 + \frac{\tanh \tilde{\eta}}{\tanh 1.5} \right), \quad (5-3)$$

where $-1.5 < \tilde{\eta} < 1.5$. Such mapping introduces a non-uniform spacing of the computational nodes in the vertical direction, with stretching in the middle of the domain and clustering near boundaries, as shown in Figure 5-1.

As Figure 5-2 shown, two sets of numerical simulation are presented in this chapter, one is simulated with the lower boundary of artificial ripples which is introduced in Druzhinin (2012) and the other is simulated with the lower boundary of simulated ripples which is introduced in Tsai (2015), with initial $ak = 0.2$ and $ak = 0.3$, respectively, both of their wave length are $\lambda = 7$ cm. In the present study, the case of artificial ripples and simulated ripples are named as AR020 and SR030, respectively. There are five time steps in SR030 and a single time step in AR020.

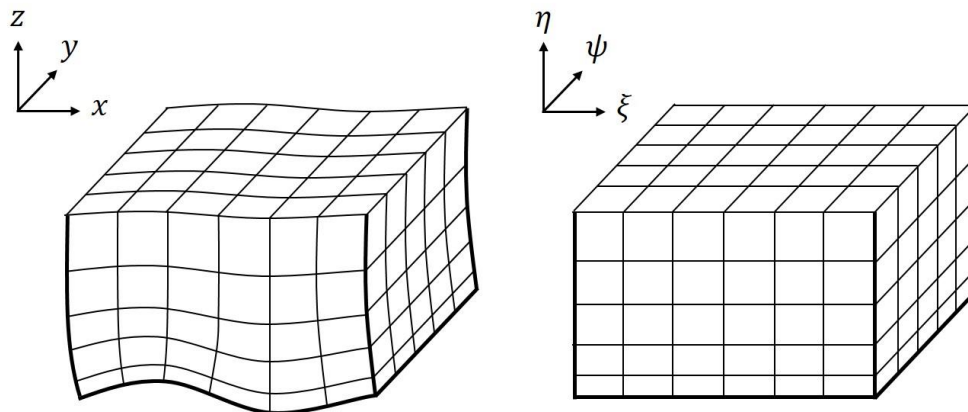
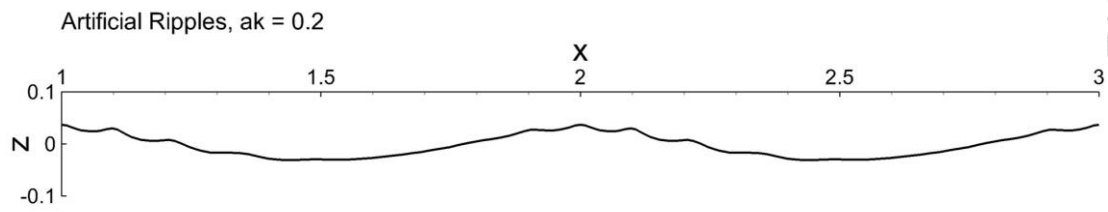


Figure 5-1: An illustration of physical domain (left) and computational domain (right) above wavy surface.



(a)



(b)

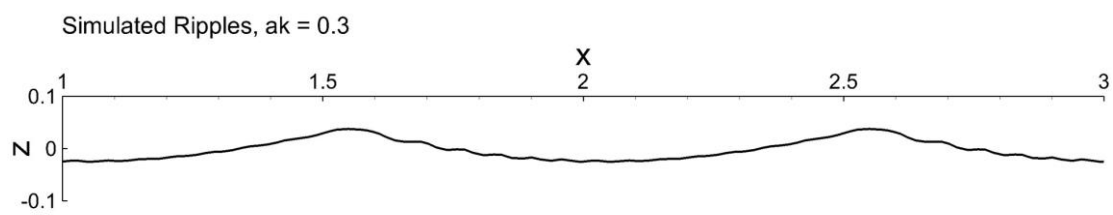
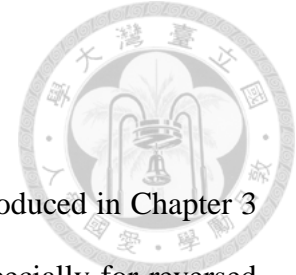


Figure 5-2: Wave shape of (a) artificial ripples with $ak = 0.2$; and (b) simulated ripples with $ak = 0.3$.

5.2 Results of structure identification



In this section, we apply the vortex identification methods introduced in Chapter 3 to the numerical simulation, and observe the vortical structures especially for reversed and forward horseshoe vortices. Additionally, we discover the existence of structure evolution and larger scale vortical motion.

After applying the vortex identification methods, a flow field full of turbulent structures appears. As Figure 5-3(a) and Figure 5-4(a) show, the vortical structures in the two cases are too abundant and complicated to observe; thus, before identifying vortical structures, values of the isosurface that represents the vortical structures has to be determined appropriately. Note that in the present study, the vortical structures are exhibited at the region near wave surface.

Figure 5-3 and Figure 5-4 show the cases AR020 and SR030, respectively. We choose an arbitrary time sequence for SR030 since the intensity of vortical structures between different time sequences are approximate. As the isosurface value of λ_{ci}^2 increase, weak and trivial structures vanish, hence the flow field becomes easier to observe; however, the structures start splitting when the value of λ_{ci}^2 gets too large. As a result, we determine $\lambda_{ci}^2 = 4$ as an appropriate value of the isosurface for both cases.

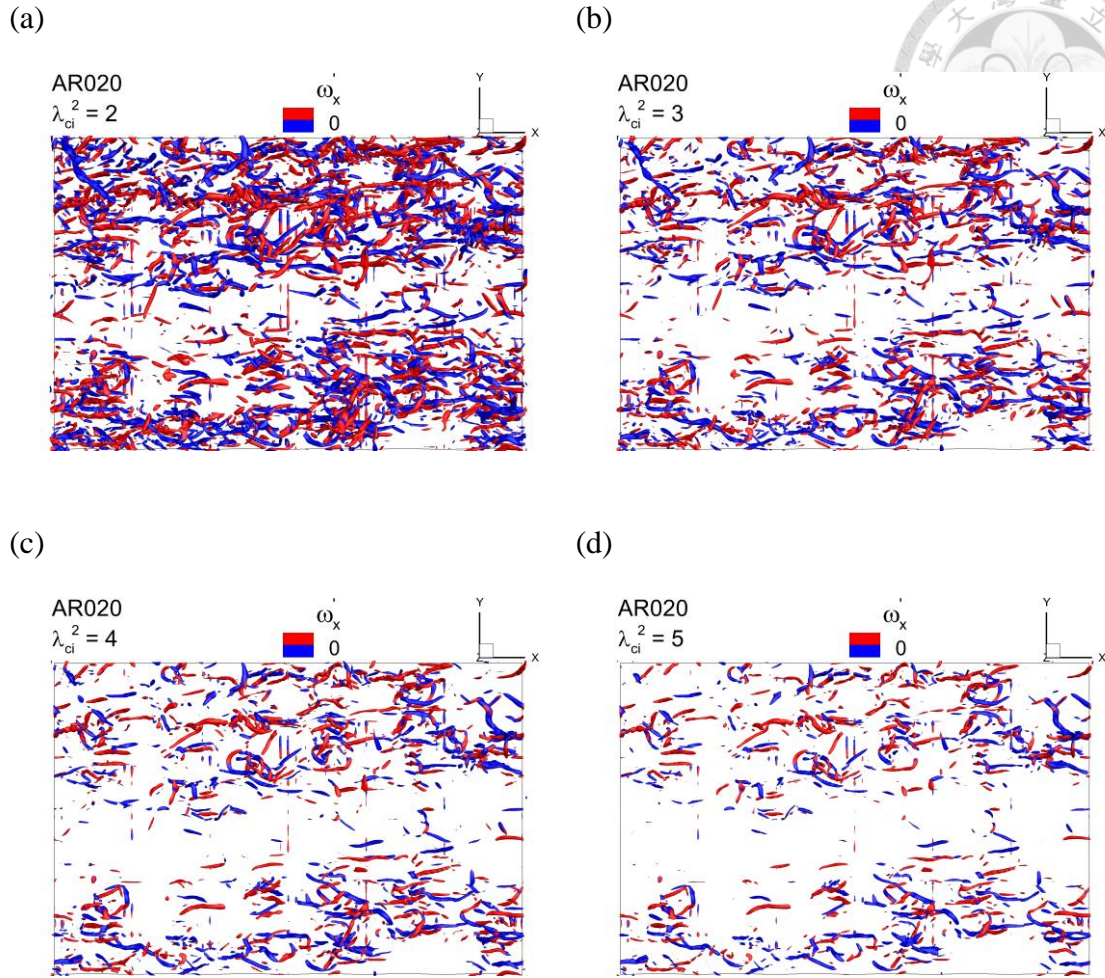


Figure 5-3: (Top view) Vortical structures above wavy surface of artificial ripples with $ak = 0.2$. The wave propagates from left to right and the vortical structures are represented by isosurface of (a) $\lambda_{ci}^2 = 2$, (b) $\lambda_{ci}^2 = 3$, (c) $\lambda_{ci}^2 = 4$, (d) $\lambda_{ci}^2 = 5$. The structures with $\omega'_x > 0$ are marked in red color; the structures with $\omega'_x < 0$ are marked in blue color.

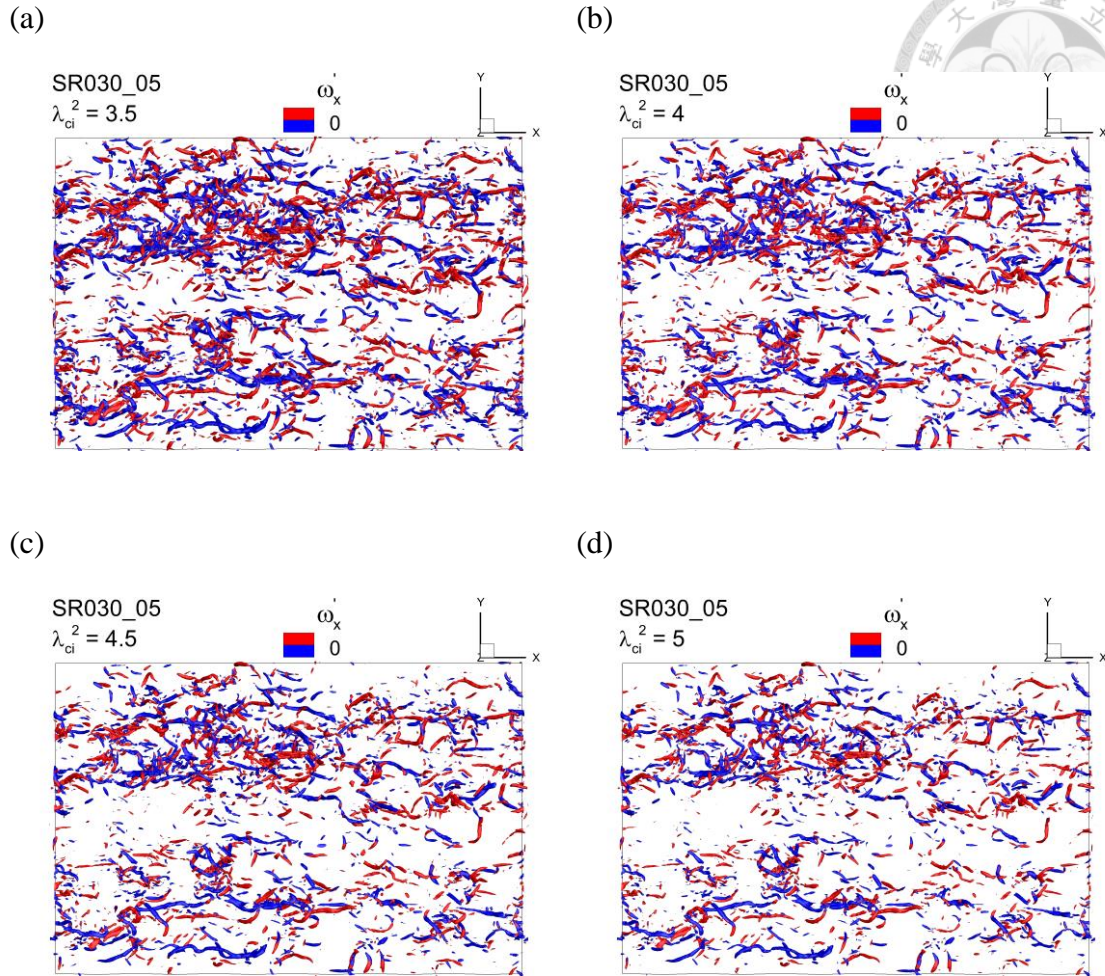


Figure 5-4: (Top view) Vortical structures above wavy surface of simulated ripples with $ak = 0.3$, time sequence = 05. The wave propagates from left to right and the vortical structures are represented by isosurface of (a) $\lambda_{ci}^2 = 3.5$, (b) $\lambda_{ci}^2 = 4$, (c) $\lambda_{ci}^2 = 4.5$, (d) $\lambda_{ci}^2 = 5$. The structures with $\omega'_x > 0$ are marked in red color; the structures with $\omega'_x < 0$ are marked in blue color.

5.2.1 Equivalent thresholds

In section 3.5, we introduced the equivalent thresholds for intense vortical structures proposed by Chakraborty et al. Hereinafter, we apply the equivalent thresholds to the numerical simulation.

From the discussion in the previous section, $\varepsilon^2 = 4$ is used for both cases as a value of the isosurface. Note that the value of ε represents the isosurface of vortical structures. The isosurface is a surface that represents points of a constant value within a volume of space. Figure 5-5 and Figure 5-6 show results after applying equivalent thresholds to the case AR020 and SR030, respectively. We choose an arbitrary time sequence for SR030 since the intensity of vortical structures between different time sequences are similar. Figure 5-5 shows that four methods bring out similar results. However, in Figure 5-6(b), it can be seen that Δ method is more fluctuating than other methods. If we modify the isosurface value of Δ , four methods can give more similar results, as shown in Figure 5-7.



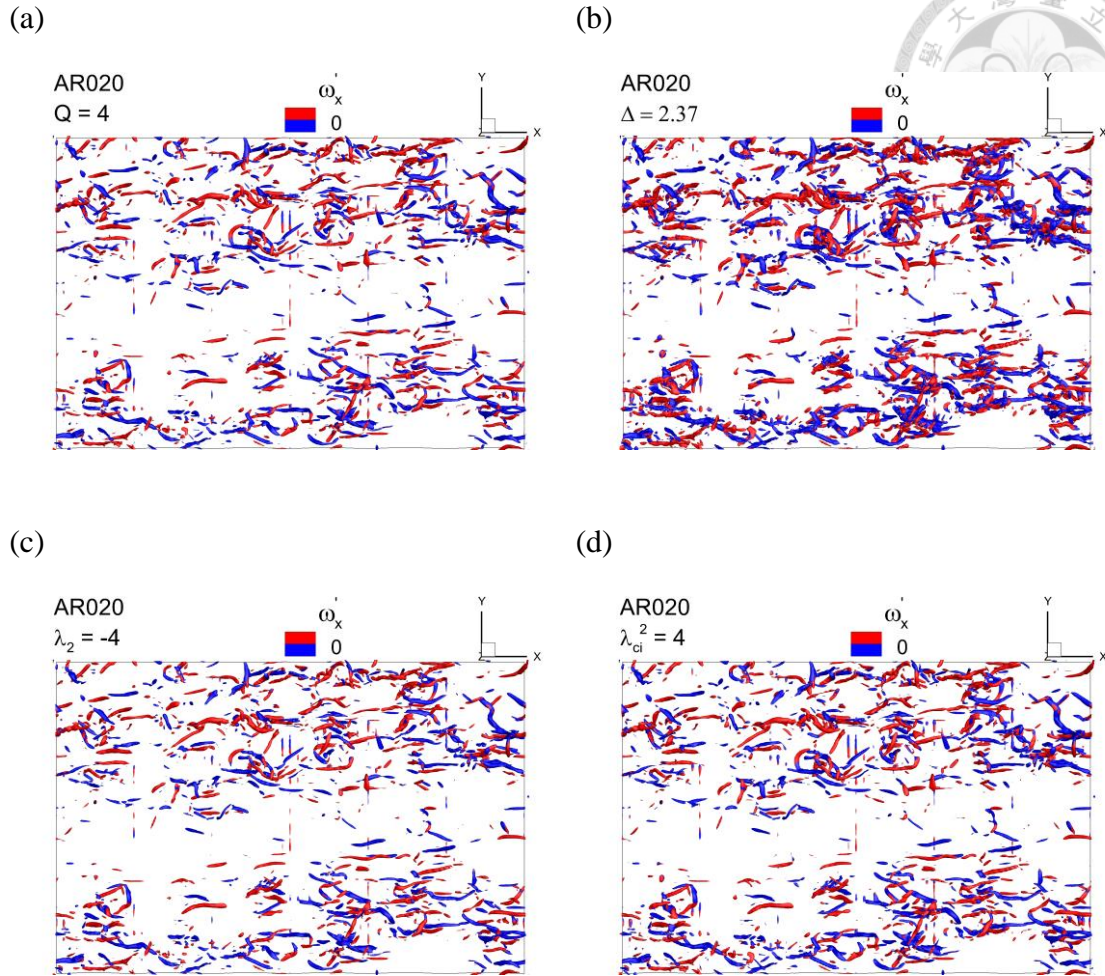


Figure 5-5: (Top view) Vortical structures above wavy surface of artificial ripples with $ak = 0.2$. The wave propagates from left to right and the vortical structures are represented by the isosurface of (a) $Q = 4$, (b) $\Delta = 4$, (c) $\lambda_2 = -4$, (d) $\lambda_{ci}^2 = 4$. The structures with $\omega'_x > 0$ are marked in red color; the structures with $\omega'_x < 0$ are marked in blue color.

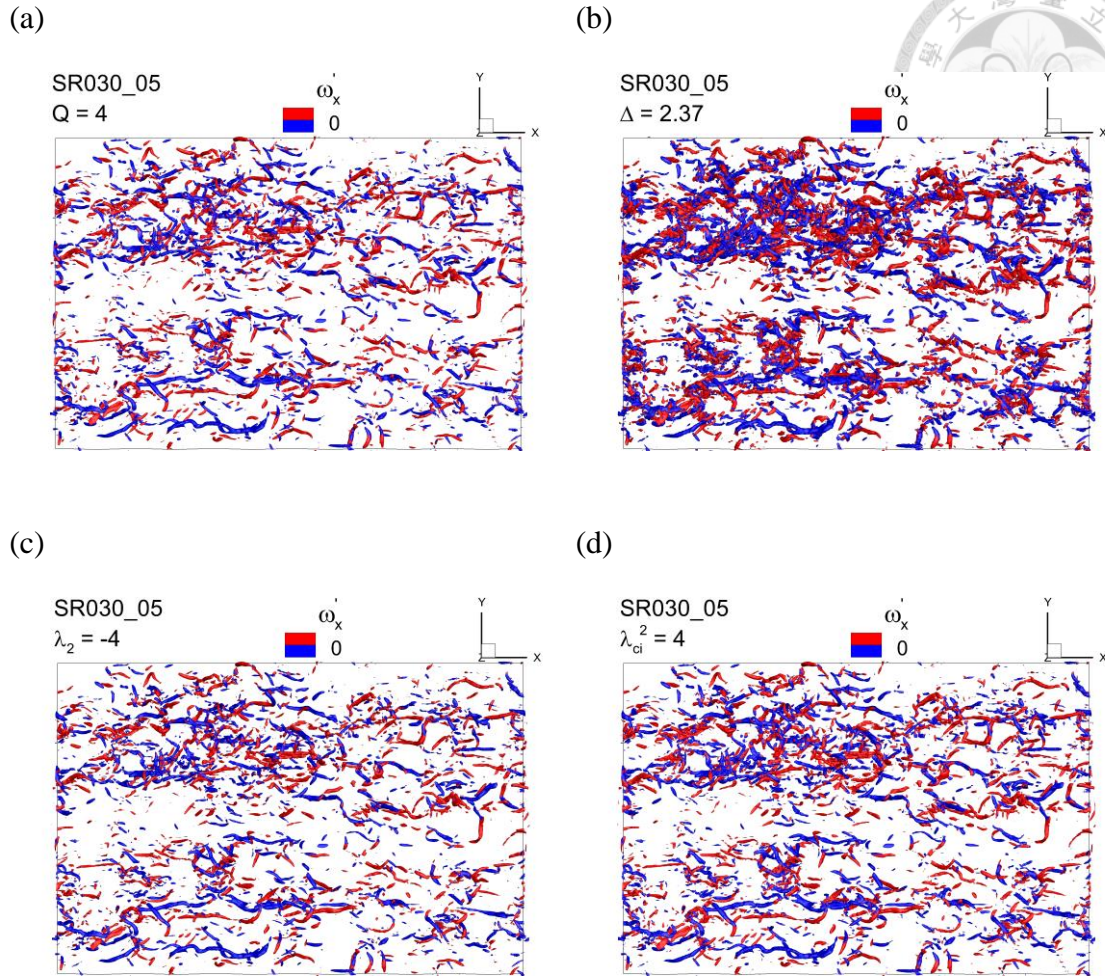


Figure 5-6: (Top view) Vortical structures above wavy surface of simulated ripples with $ak = 0.3$, time sequence = 05. The wave propagates from left to right and the vortical structures are represented by the isosurface of (a) $Q = 4$, (b) $\Delta = 2.37$, (c) $\lambda_2 = -4$, (d) $\lambda_{ci}^2 = 4$. The structures with $\omega'_x > 0$ are marked in red color; the structures with $\omega'_x < 0$ are marked in blue color.

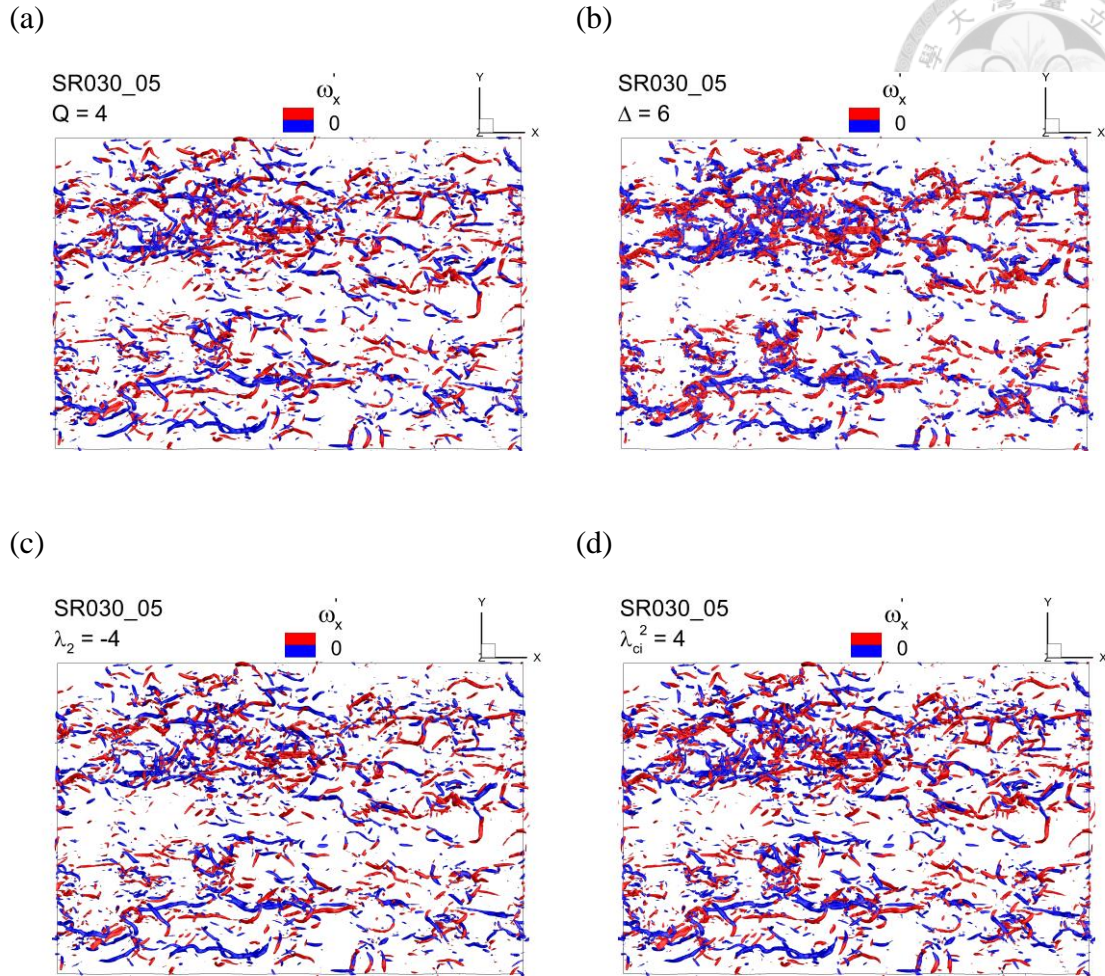
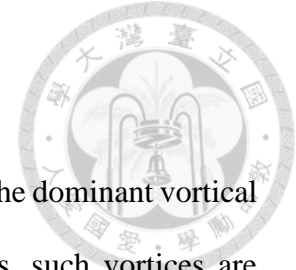


Figure 5-7: (Top view) Vortical structures above wavy surface of simulated ripples with $ak = 0.3$, time sequence = 05. The wave propagates from left to right and the vortical structures are represented by the isosurface of (a) $Q = 4$, (b) $\Delta = 6$, (c) $\lambda_2 = -4$, (d) $\lambda_{ci}^2 = 4$. The structures with $\omega'_x > 0$ are marked in red color; the structures with $\omega'_x < 0$ are marked in blue color.

5.2.2 Vortical structures



In the simulated case by Yang and Shen (2009), they found that the dominant vortical structures in the wavy boundary are the quasi-streamwise vortices, such vortices are mostly located above windward face. In addition to these quasi-streamwise vortices, there exist some reversed horseshoe vortices near the wave trough. About 1/4 of the horseshoe vortices are forward type, and about 3/4 of them are reversed type.

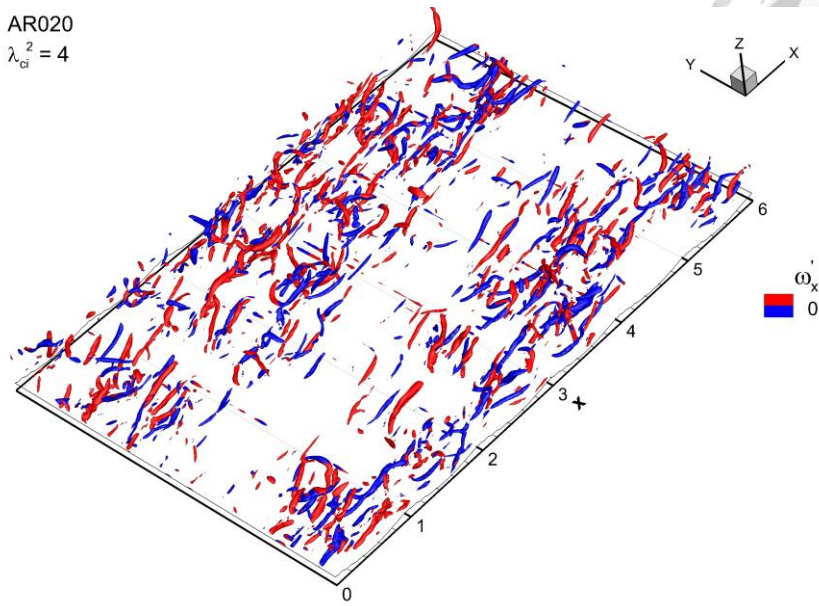
For the case AR020, the vortical structures are shown in Figure 5-8. Similar to Yang and Shen's result, quasi-streamwise vortices are dominant; however, vortical structures attributed to capillary ripples are profound in this case. Figure 5-9 shows the forward and reversed horseshoe vortices subjectively marked by green and yellow circles, respectively. The ratio of forward and reversed horseshoe vortices is close to that of Yang and Shen's. Additionally, most reversed horseshoe vortices are observed near the wave trough.

For the case SR030, the evolution of the vortical structures is shown in Figure 5-10. It is found that the vortical structures attributed to capillary ripples vanish in this case and the dominant vortical structures are also quasi-streamwise vortices. The forward and reversed horseshoe vortices of the last time sequence are subjectively marked by green and yellow circles in Figure 5-11, respectively. In this case, more forward horseshoe vortices are observed than reversed horseshoe vortices. Similar to AR020, the reversed horseshoe vortices are mostly located near the wave trough.

Note that in both cases, there are few vortical structures around the spanwise central region, we will discuss this phenomenon in section 5.2.4.

(a)

AR020
 $\lambda_{ci}^2 = 4$



(b)

AR020
 $\lambda_{ci}^2 = 4$

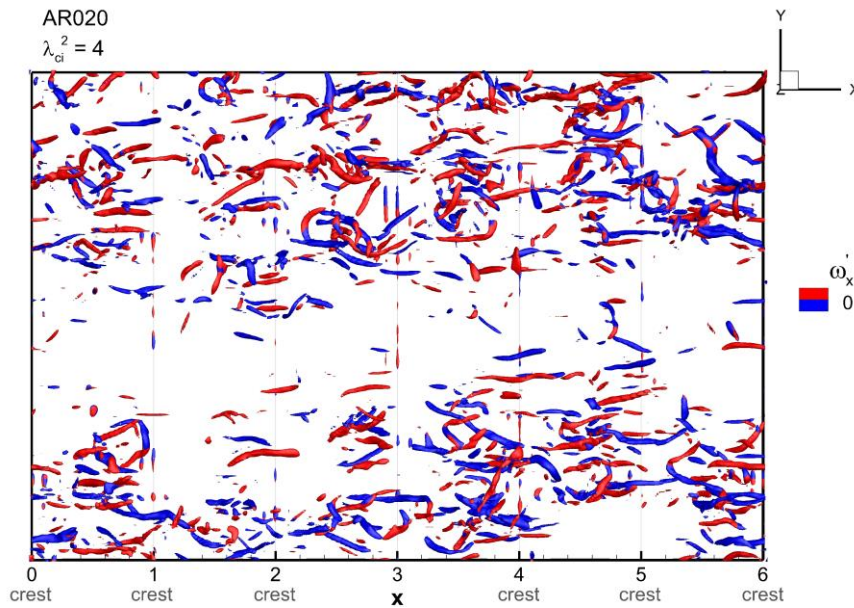


Figure 5-8: Vortical structures above wavy surface of artificial ripples with $ak = 0.2$: (a) oblique view; (b) top view. The wave propagates from left to right and the vortical structures are represented by the isosurface of $\lambda_{ci}^2 = 4$. The structures with $\omega'_x > 0$ are marked in red color; the structures with $\omega'_x < 0$ are marked in blue color.

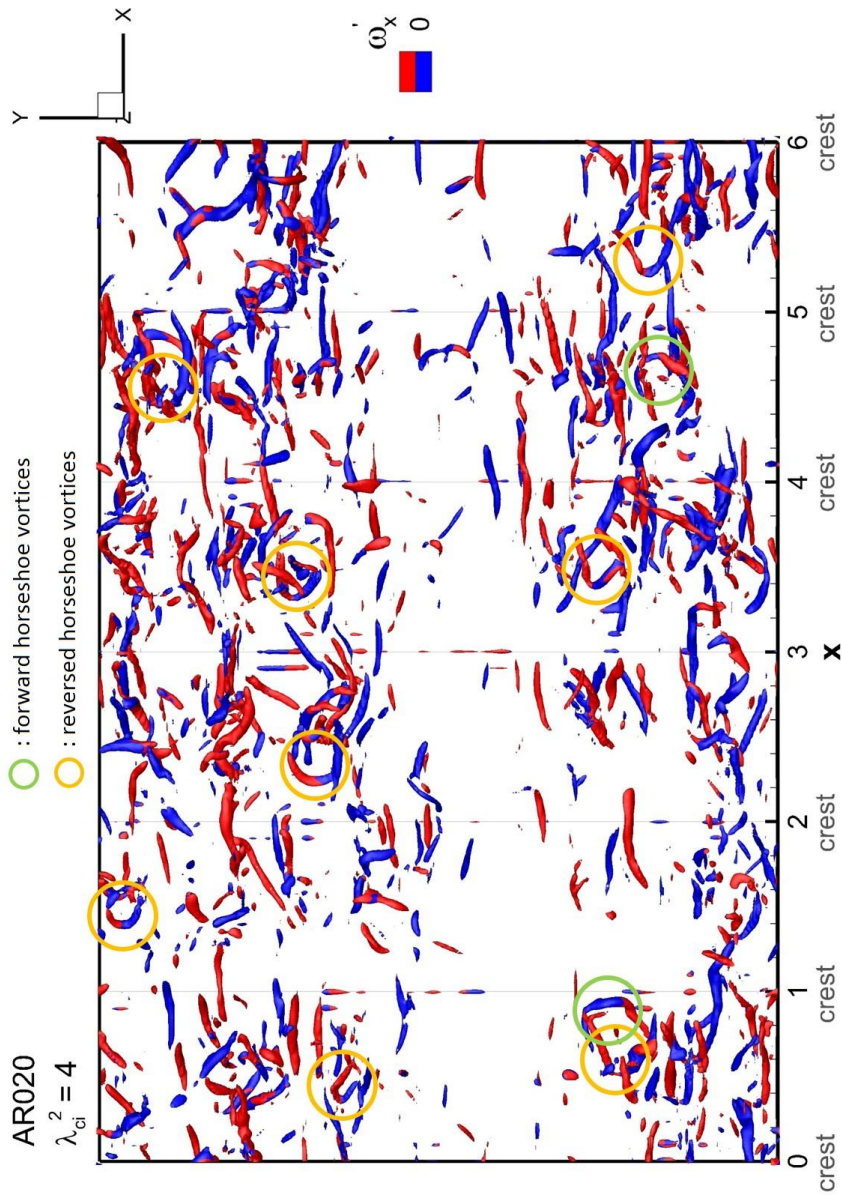


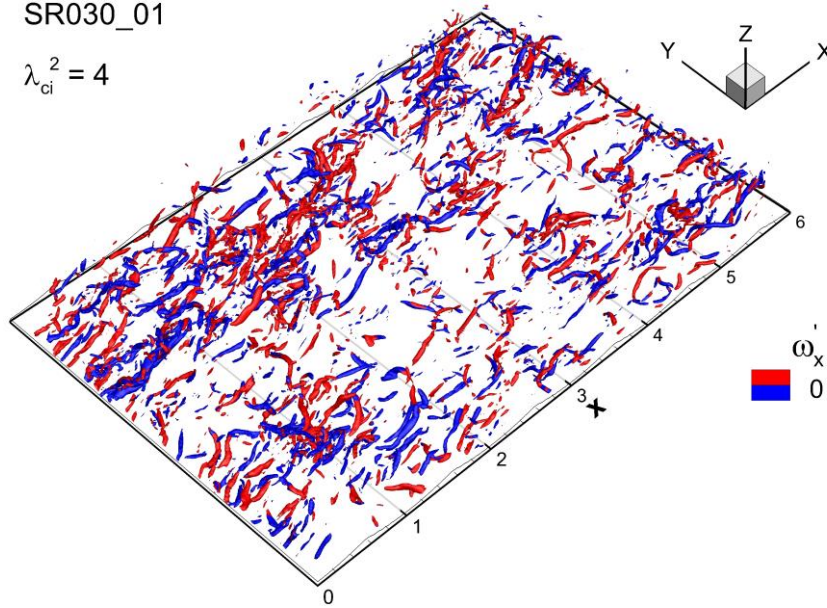
Figure 5-9: Forward and reversed horseshoe vortices above wavy surface of artificial ripples with $ak = 0.2$. The wave propagates from left to right and the vortical structures are represented by the isosurface of $\lambda_{ci}^2 = 4$. The structures with $\omega'_x > 0$ are marked in red color; the structures with $\omega'_x < 0$ are marked in blue color.



(a)

SR030_01

$$\lambda_{ci}^2 = 4$$



(b)

SR030_01

$$\lambda_{ci}^2 = 4$$

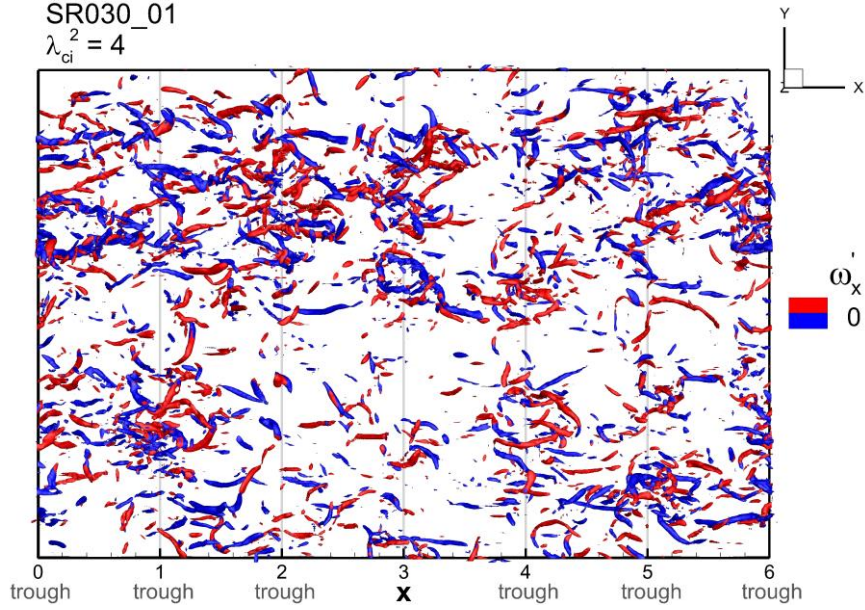
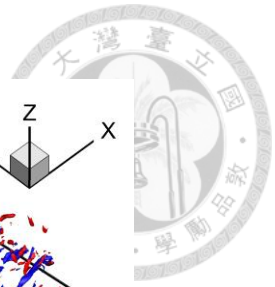
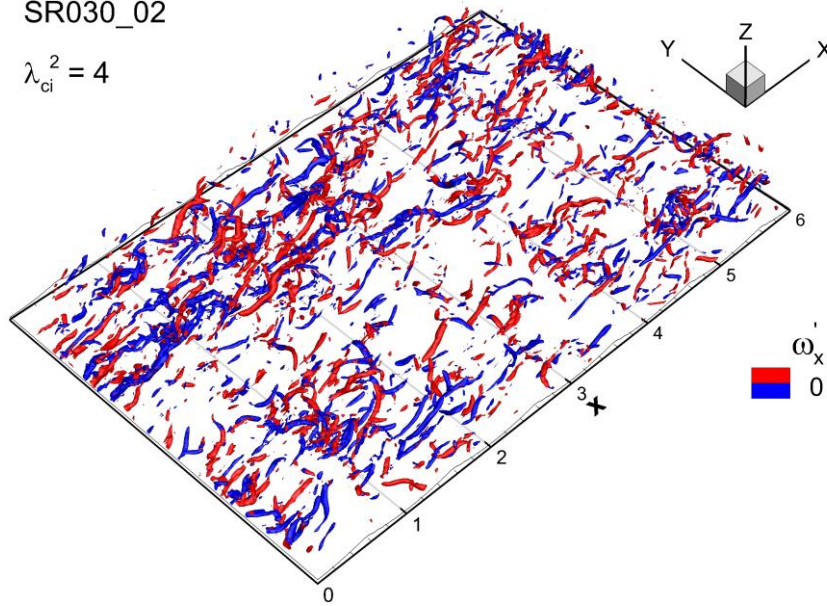


Figure 5-10 (a, b): For caption see page 52.

(c)

SR030_02

$$\lambda_{ci}^2 = 4$$



(d)

SR030_02

$$\lambda_{ci}^2 = 4$$

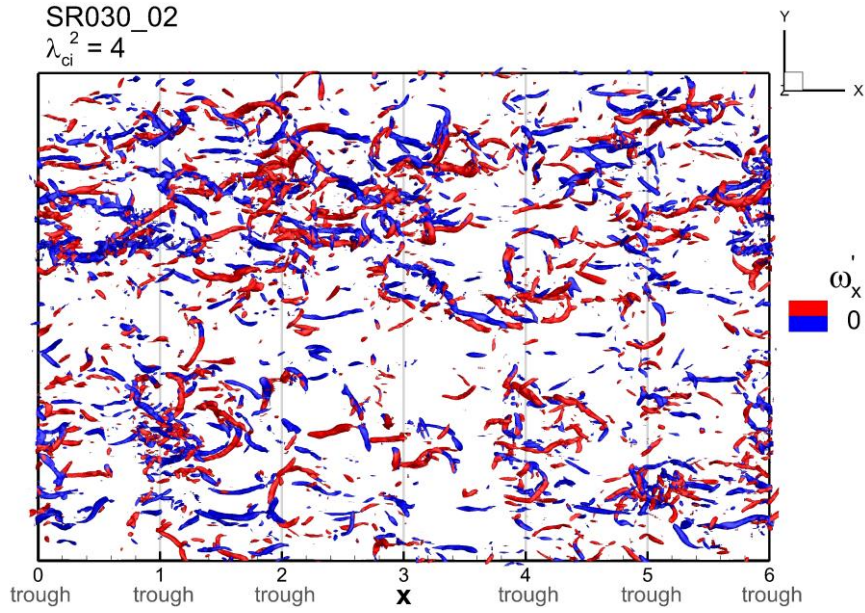
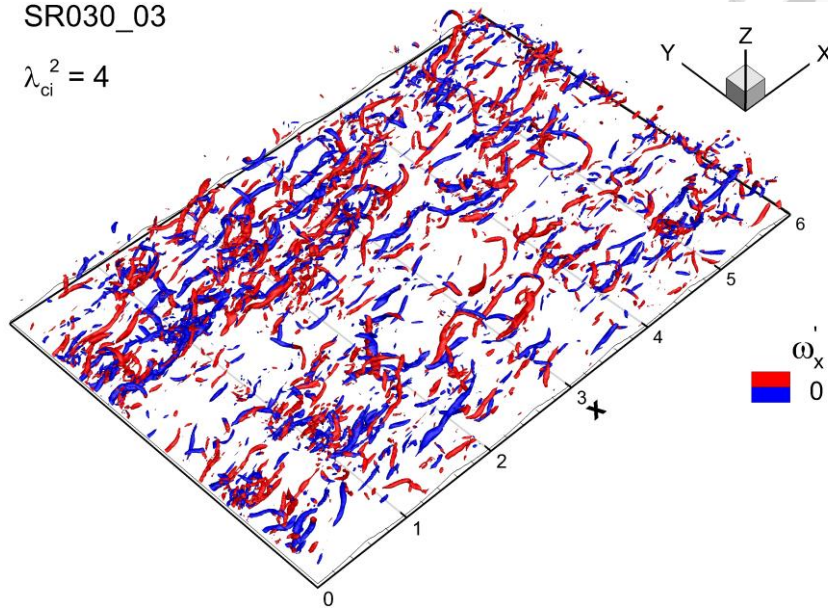


Figure 5-10 (c, d): For caption see page 52.

(e)

SR030_03

$$\lambda_{ci}^2 = 4$$



(f)

SR030_03

$$\lambda_{ci}^2 = 4$$

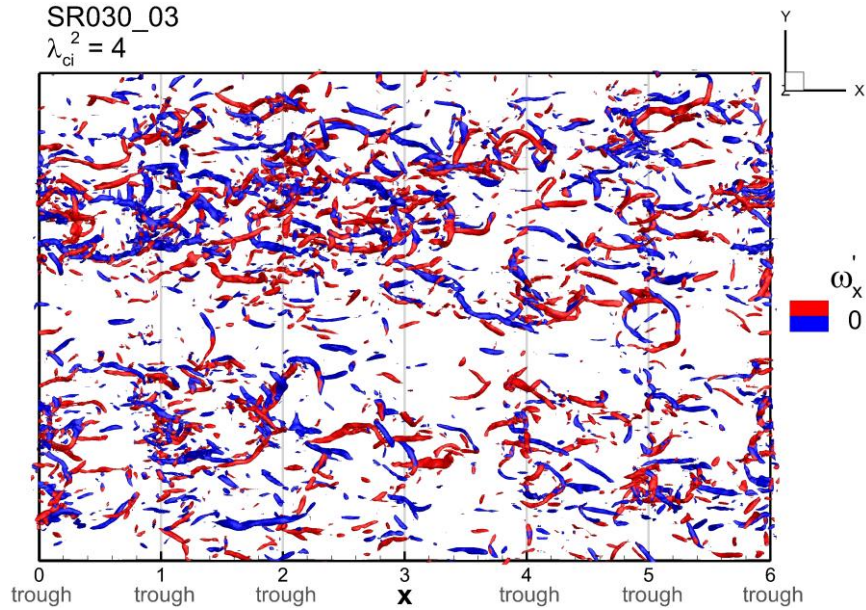
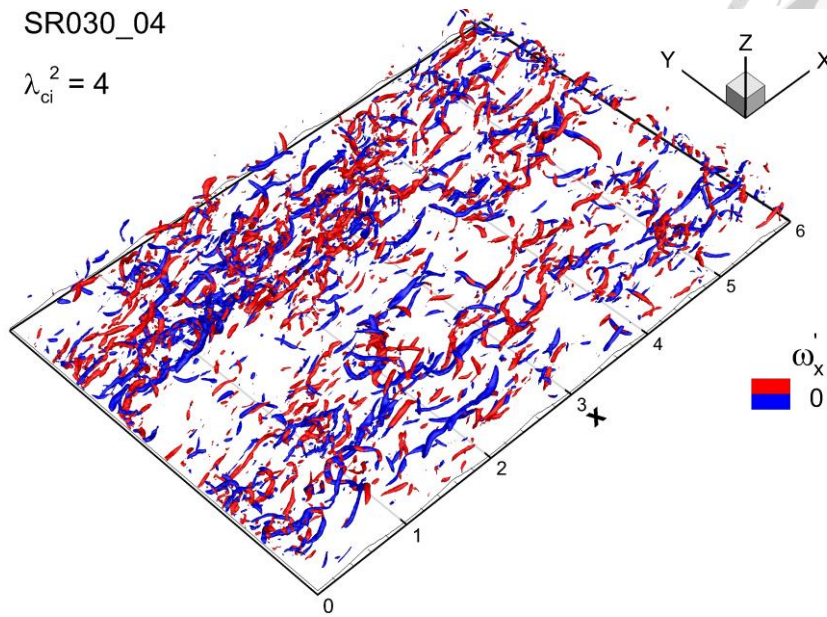


Figure 5-10 (e, f): For caption see page 52.

(g)

SR030_04

$$\lambda_{ci}^2 = 4$$



(h)

SR030_04

$$\lambda_{ci}^2 = 4$$

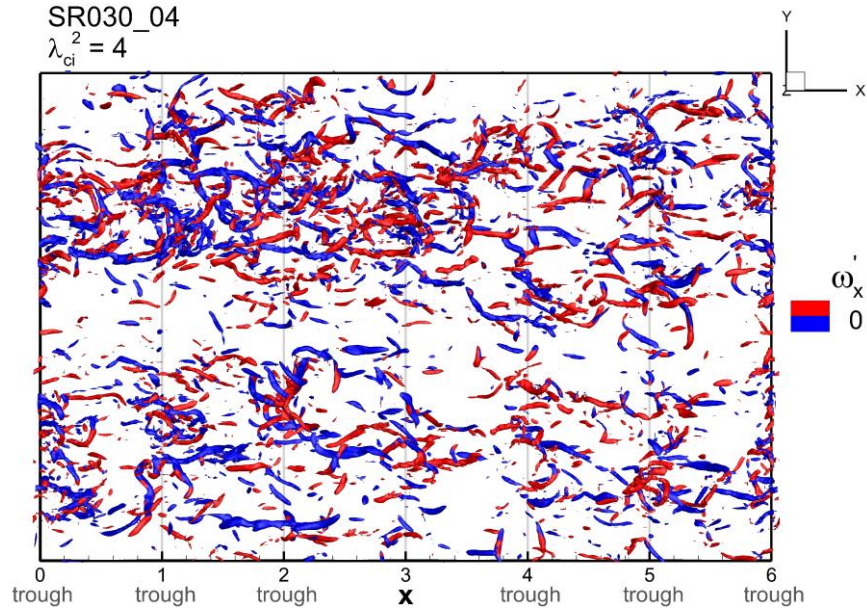


Figure 5-10 (g, h): For caption see page 52.

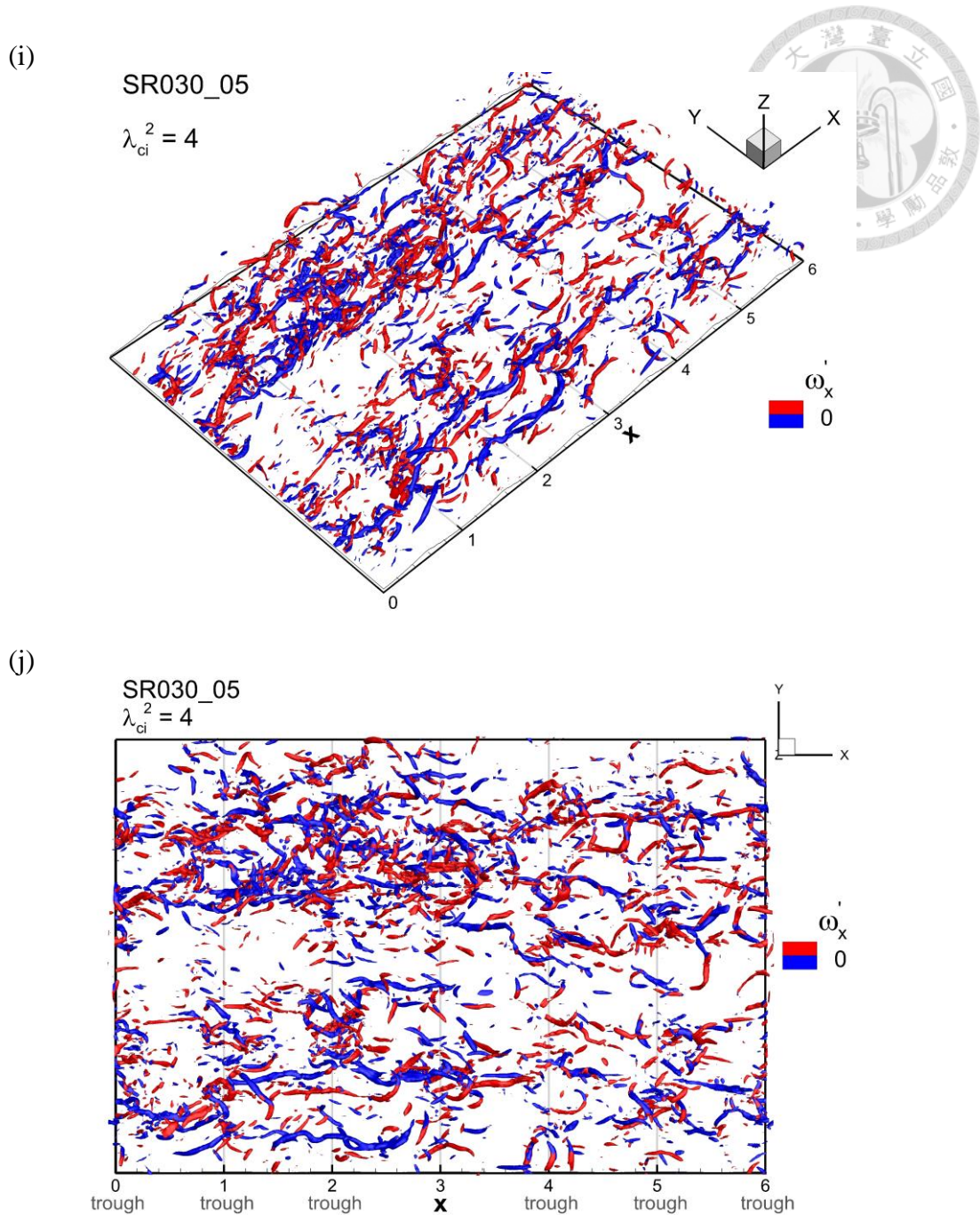


Figure 5-10: Time evolution of vortical structures above wavy surface of artificial ripples with $ak = 0.3$ (oblique and top view): (a, b) time sequence = 01; (c, d) 02; (e, f) 03; (g, h) 04; (i, j) 05. The wave propagates from left to right and the vortical structures are represented by the isosurface of $\lambda_{ci}^2 = 4$. The structures with $\omega'_x > 0$ are marked in red color; the structures with $\omega'_x < 0$ are marked in blue color.

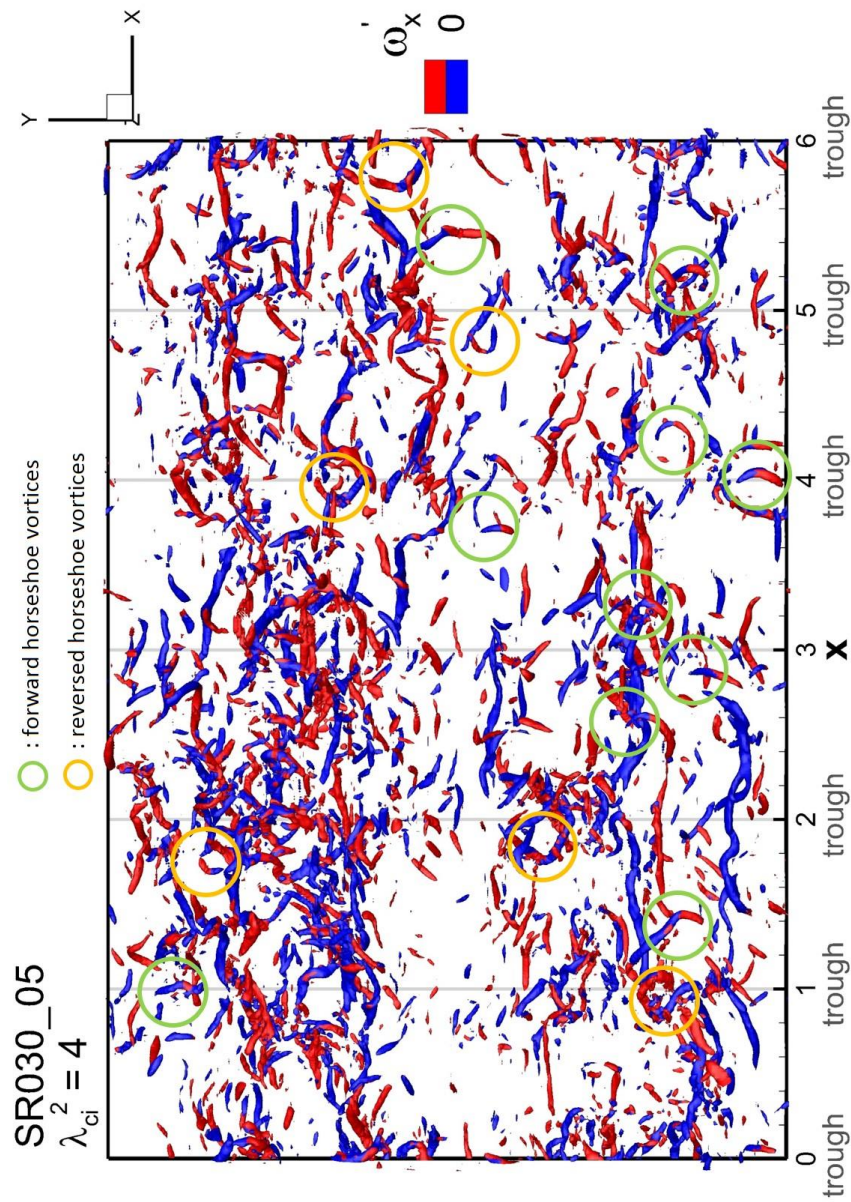
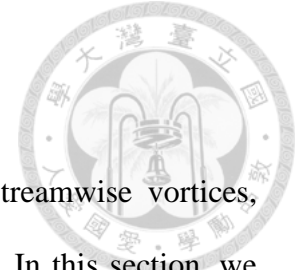


Figure 5-11: Forward and reversed horseshoe vortices above wavy surface of simulated ripples with $ak = 0.3$, time sequence = 05. The wave propagates from left to right and the vortical structures are represented by the isosurface of $\lambda_{ci}^2 = 4$. The structures with $\omega'_x > 0$ are marked in red color; the structures with $\omega'_x < 0$ are marked in blue color.



5.2.3 Regeneration of the forward horseshoe vortices



The results in the previous section indicate that the quasi-streamwise vortices, forward and reversed horseshoe vortices exist above wave surface. In this section, we investigate the evolution of the forward horseshoe vortex.

We first examine the instantaneous vortex field at successive times, hence the case SR030 with multiple time sequences is observed. Figure 5-12 shows the particular forward horseshoe vortex which is observed. The history of forward horseshoe vortex evolution is shown Figure 5-13. In Figure 5-12 (a, b) a forward horseshoe vortex marked with a green arrow is located above the wave trough, this vortical structure is a “parent” structure. In the next time sequence (c, d), the parent structure advance, and a “child” structure with a right leg, marked with a yellow arrow, is generated above the left leg of the parent structure. In (e, f) both structures grow and the parent structure propagate to the windward face; in addition, the child structure start growing its left leg. In (g, h) the child structure grow stronger; on the contrary, the parent structure weakens and breaks at its head. In the last time sequence (i, j), the parent structure vanishes.

The above investigation of vortex evolution history is just an observation, the mechanism of vortex regeneration can be studied in the future.

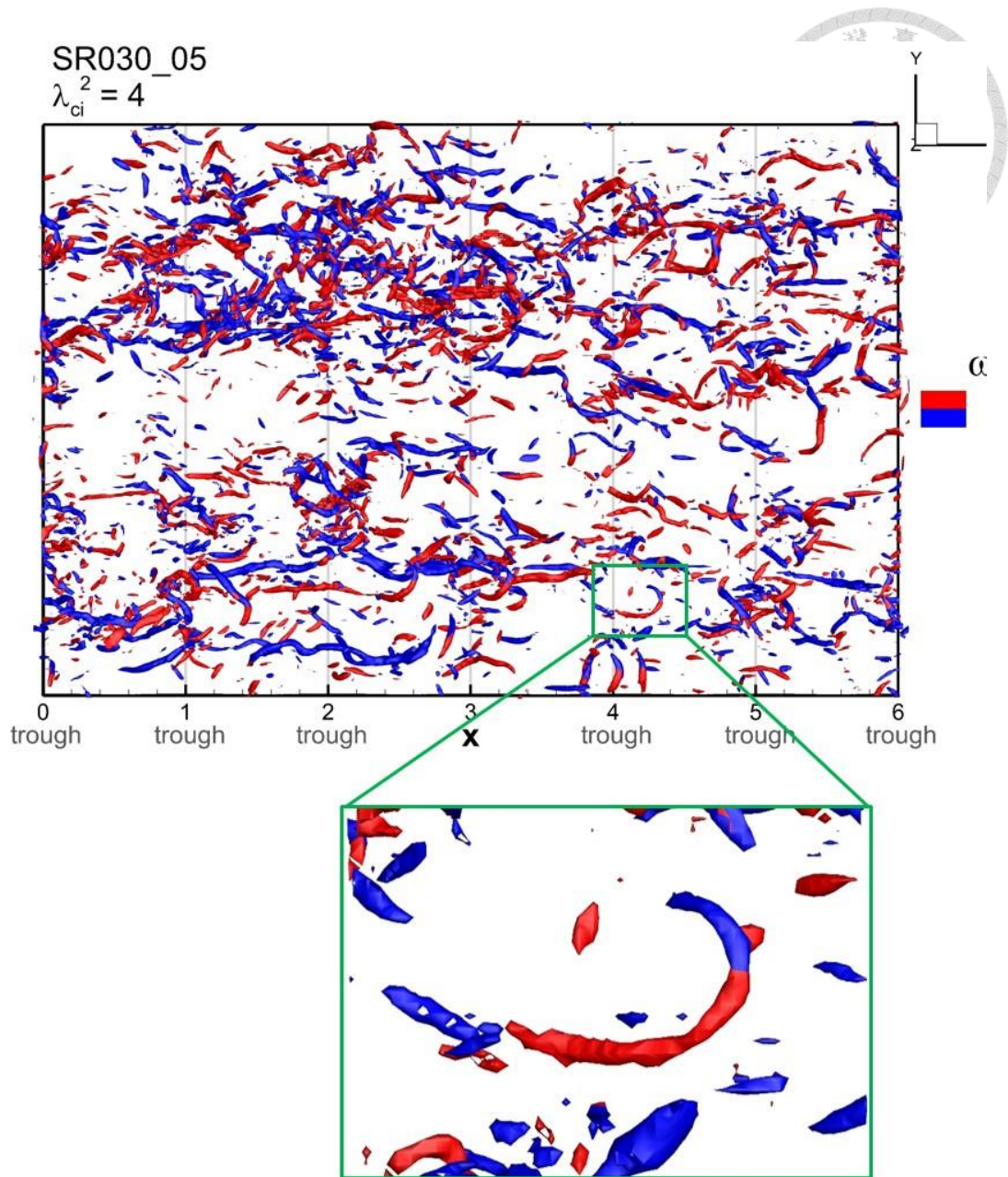


Figure 5-12: Enlarged view of the forward horseshoe vortex marked by the green box above wavy surface of simulated ripples with $ak = 0.3$. The wave propagates from left to right and the vortical structures are represented by the isosurface of $\lambda_{ci}^2 = 4$. The structures with $\omega'_x > 0$ are marked in red color; the structures with $\omega'_x < 0$ are marked in blue color.

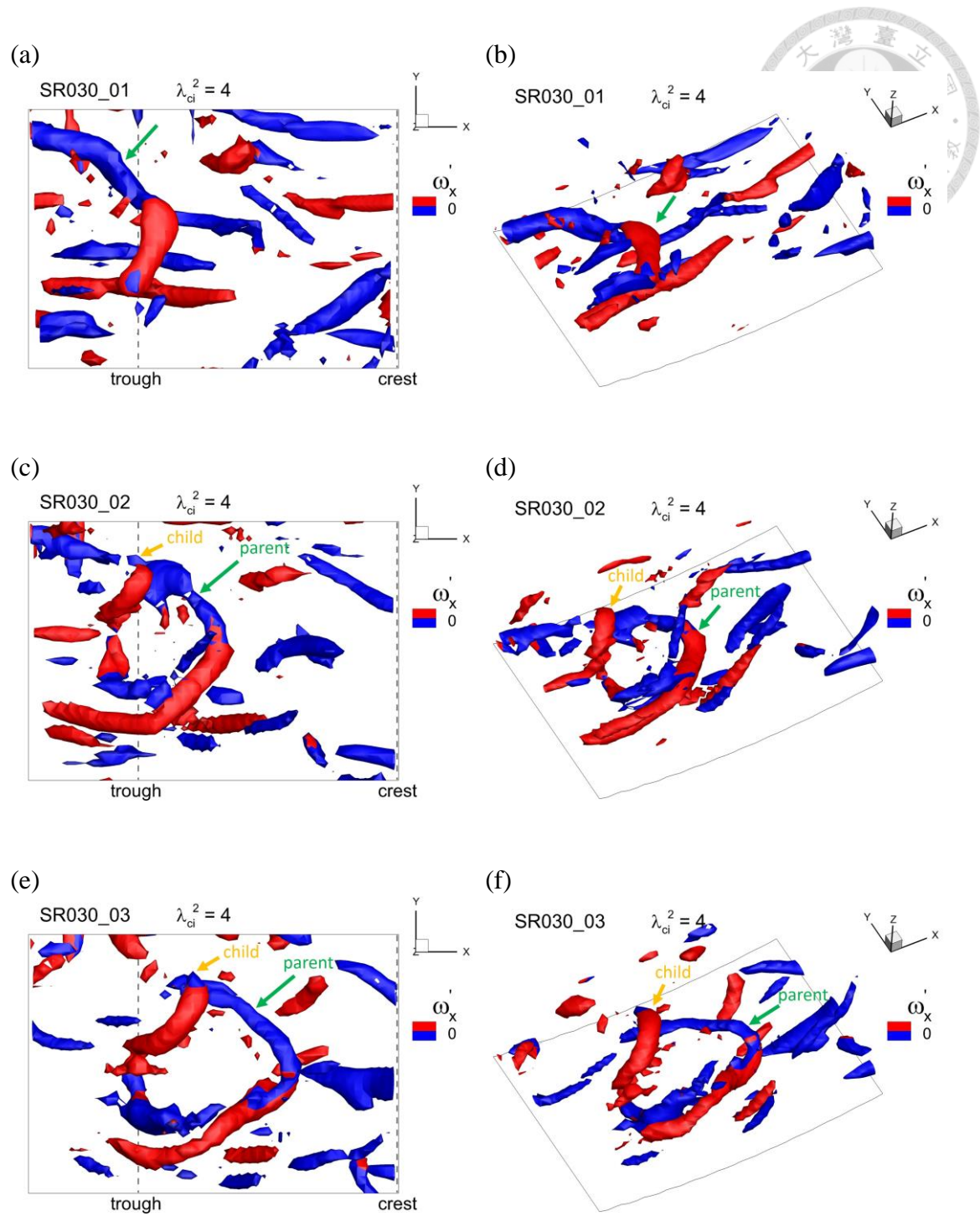
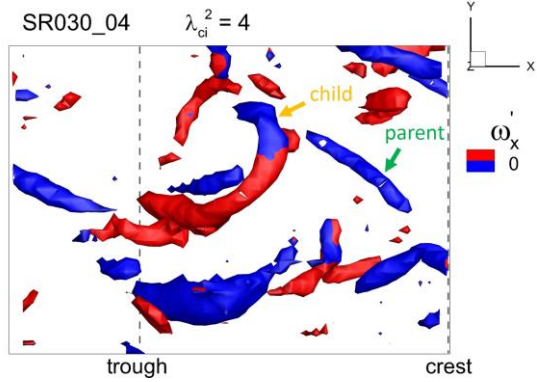
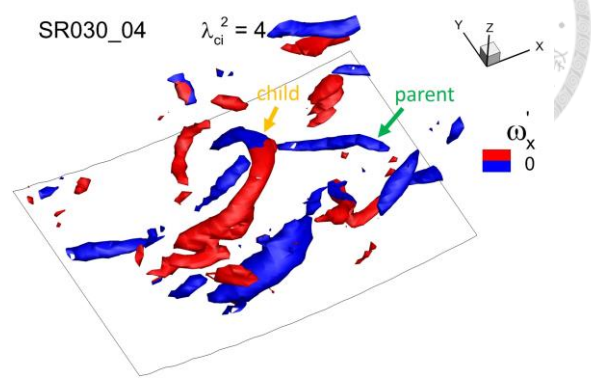


Figure 5-13 (a, b, c, d, e, f): For caption see following page.

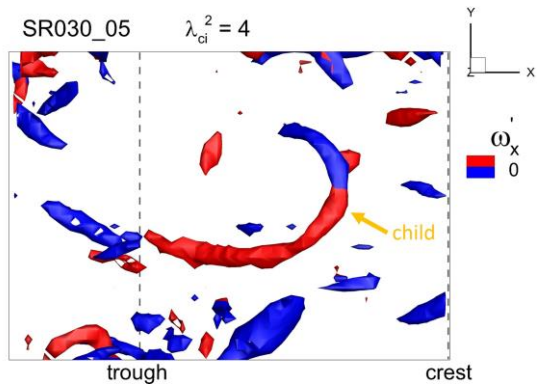
(g)



(h)



(i)



(j)

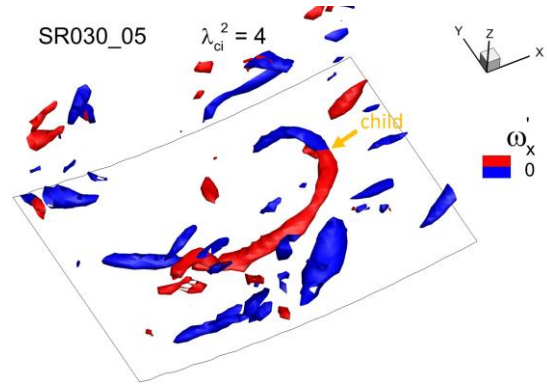



Figure 5-13: Time evolution of the forward horseshoe vortex above wavy surface (oblique and top view): (a, b) time sequence = 01; (c, d) 02; (e, f) 03; (g, h) 04; (i, j) 05. The wave propagates from left to right and the vortical structures are represented by the isosurface of $\lambda_{ci}^2 = 4$.

5.2.4 Larger scale vortical motions



In section 5.2.2, we found that there are few vortical structures around the spanwise central region in both cases of AR020 and SR030. It is found that the area with less vortical structures corresponds with a low-speed streak above those structures; on the contrary, vortical structures tend to be produced within the high-speed region, as shown in Figure 5-14(b). Since two high-speed and two low-speed streaks can be observed and the flow is periodical in the spanwise direction, the width of each streak is about quarter of the span width. The observation above implies that there must exist a larger scale vortical motion over the flow field.

To investigate the relation between streaks and entire flow field, distributions of streamwise-averaged turbulent velocities are shown in Figure 5-15. The interfaces of the high- and low-speed streamwise turbulent velocity contour marked by dash lines are corresponding with that of the high- and low-speed streaks. Furthermore, the turbulent velocity contours reveal the existence of larger scale counter-rotating vortical motions in the flow field. It is assumed that there are different mechanisms in producing vortical structures and larger scale vortical motions. The vortical structures are attributed to the wall boundary layer, and the larger scale vortical motions are speculated to be related to the Langmuir circulation, which is attributed to the instability caused by wave, see Tsai (2017).

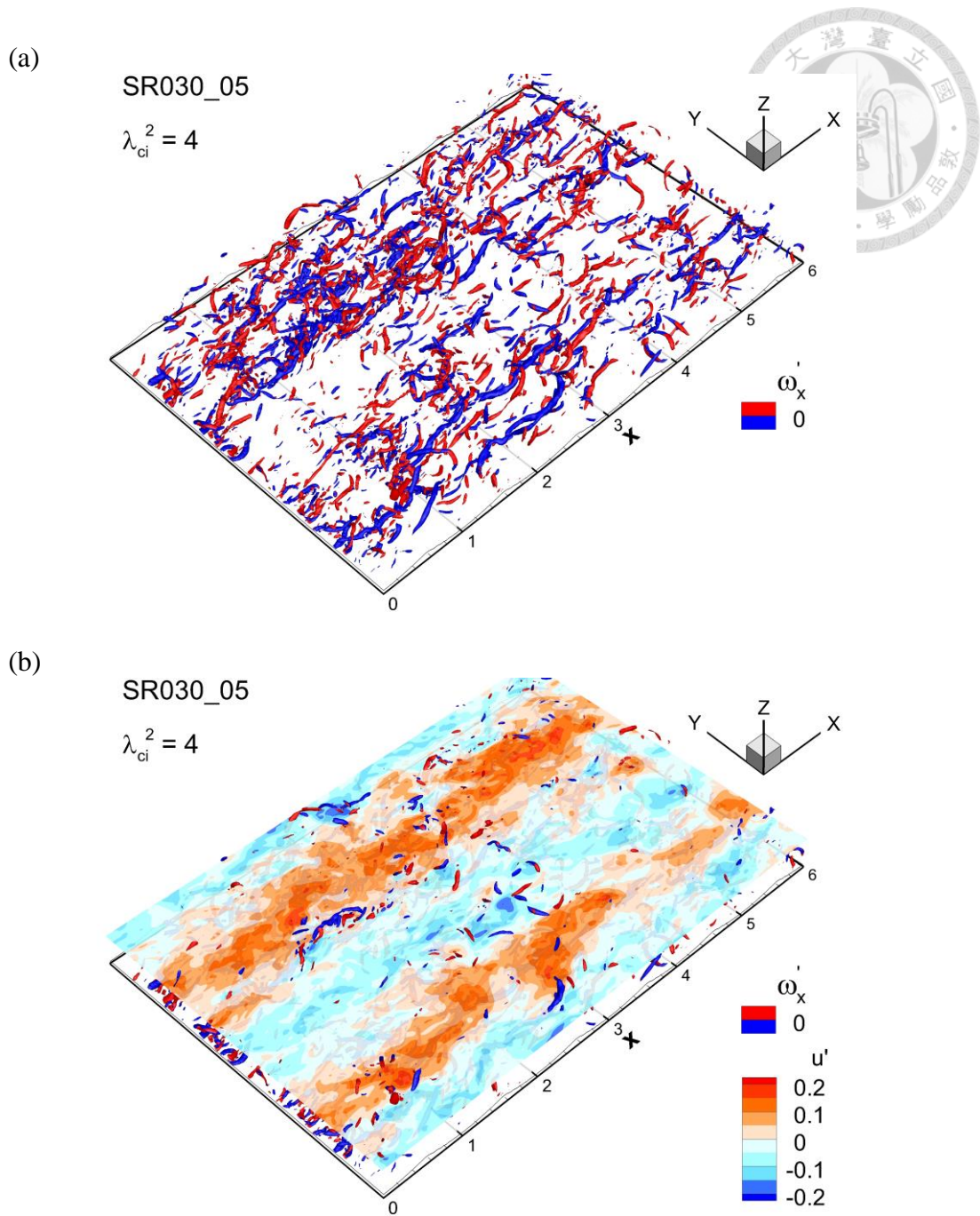


Figure 5-14: (a) Vortical structures above wavy surface of simulated ripples with $ak = 0.3$, time sequence = 05. (b) Vortical structures and streamwise turbulent velocity contour above these structures. The wave propagates from left to right and the vortical structures are represented by the isosurface of $\lambda_{ci}^2 = 4$. The structures with $\omega'_x > 0$ are marked in red color; the structures with $\omega'_x < 0$ are marked in blue color.

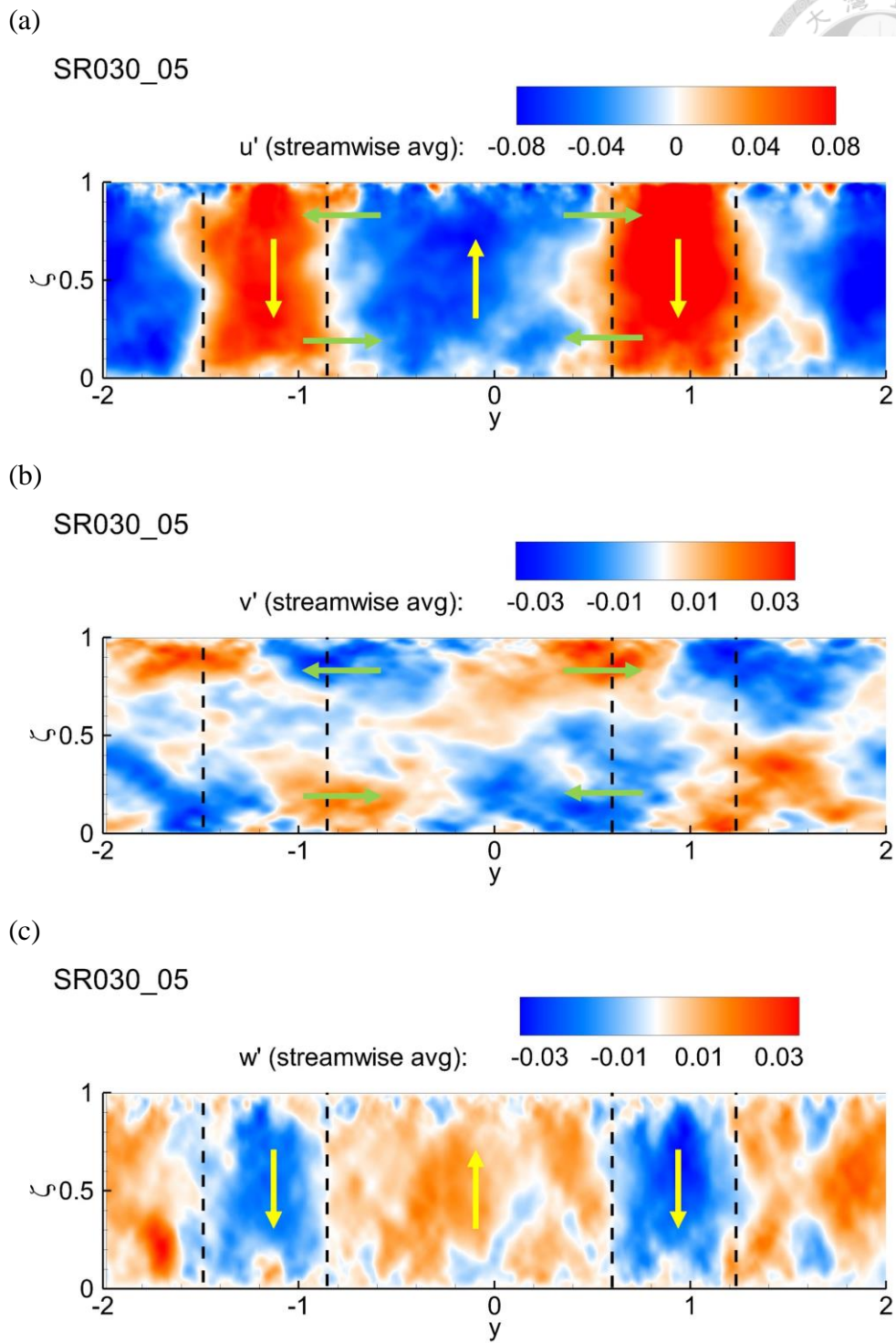
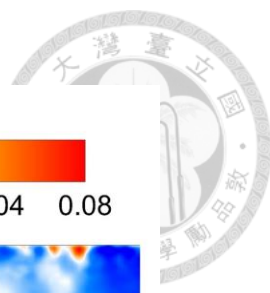


Figure 5-15: Distribution of streamwise-averaged (a) streamwise, (b) spanwise and (c) vertical turbulent velocity above wavy surface of simulated ripples with $ak = 0.3$, time sequence = 05. The green and yellow arrows indicate flow directions. The dotted lines mark the interface of fast and slow-moving fluids.

5.3 Conditional averaging analysis

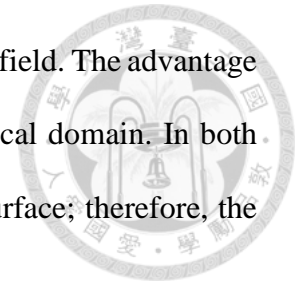


5.3.1 Conditional averaging procedures

The conditional sampling methods are introduced in Chapter 2. Hereinafter we introduce the ensemble averaging method. To conditional average the events in the three-dimensional space, we create several cuboid subdomains corresponding to the number of events detected by the sampling method, then place the events into the middle of the subdomains and average the flow field within these subdomains, this procedure is called ensemble average. In the present study, the length and width of the subdomain is set to be $15\Delta x$ and $15\Delta y$ for streamwise and spanwise, respectively. Note that above procedure is suitable for the numerical simulation with uniform mapping and no wave phase.

Conformal mapping in streamwise direction and non-uniform spacing in the vertical direction of the computational nodes are employed to the numerical simulation, hence ensemble average the subdomains in different phase in physical domain is impracticable. To resolve the problems, two ways of the conditional average are shown in Figure 5-16 and Figure 5-17. In Figure 5-16, we first calculate vorticities, λ_2 , λ_{ci} and so on from the velocity field, then detect events in the flow field subjectively. Eventually, the operation of the ensemble average and reveal are in the computational domain. The values of vortex identification methods are directly ensemble-averaged instead of computing from the ensemble-averaged flow field. Such procedure can avoid problems caused by the wave phase. Referring to Yang and Shen (2009), the other way is to detect events at the same wave phase and ensemble average primitive flow field of the subdomains, as shown in Figure 5-16. The first step is to determine the detection position on (x, z) -plane and design a suitable conditional sampling criterion. Then detect events at the same phase, and ensemble average the velocity field of the various subdomains. After that, the vortex

identification methods are applied to the ensemble-averaged velocity field. The advantage of this procedure is that the structures can be revealed in the physical domain. In both ways, the bottom of the subdomain is set at the position of wave surface; therefore, the problem of non-uniform spacing in the vertical direction is solved.



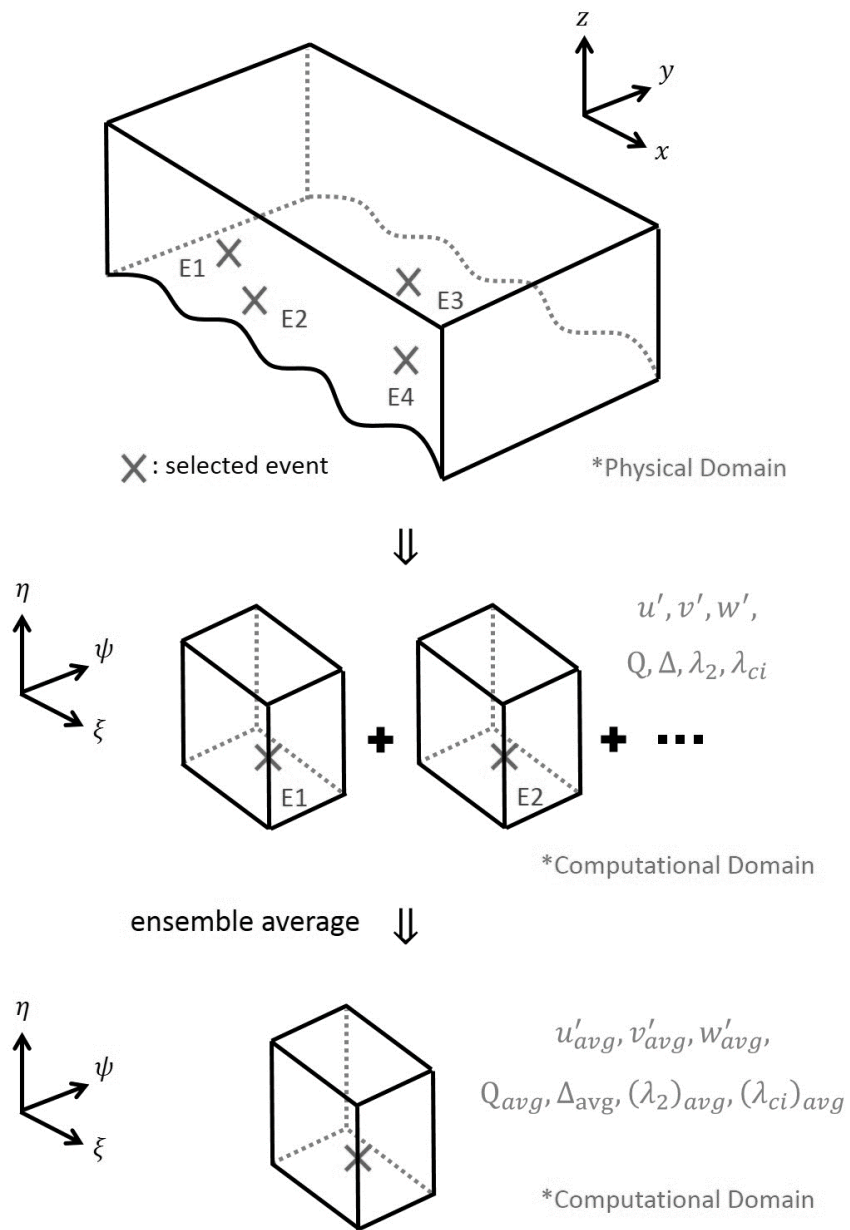


Figure 5-16: An illustration of conditional averaging in the computational domain.

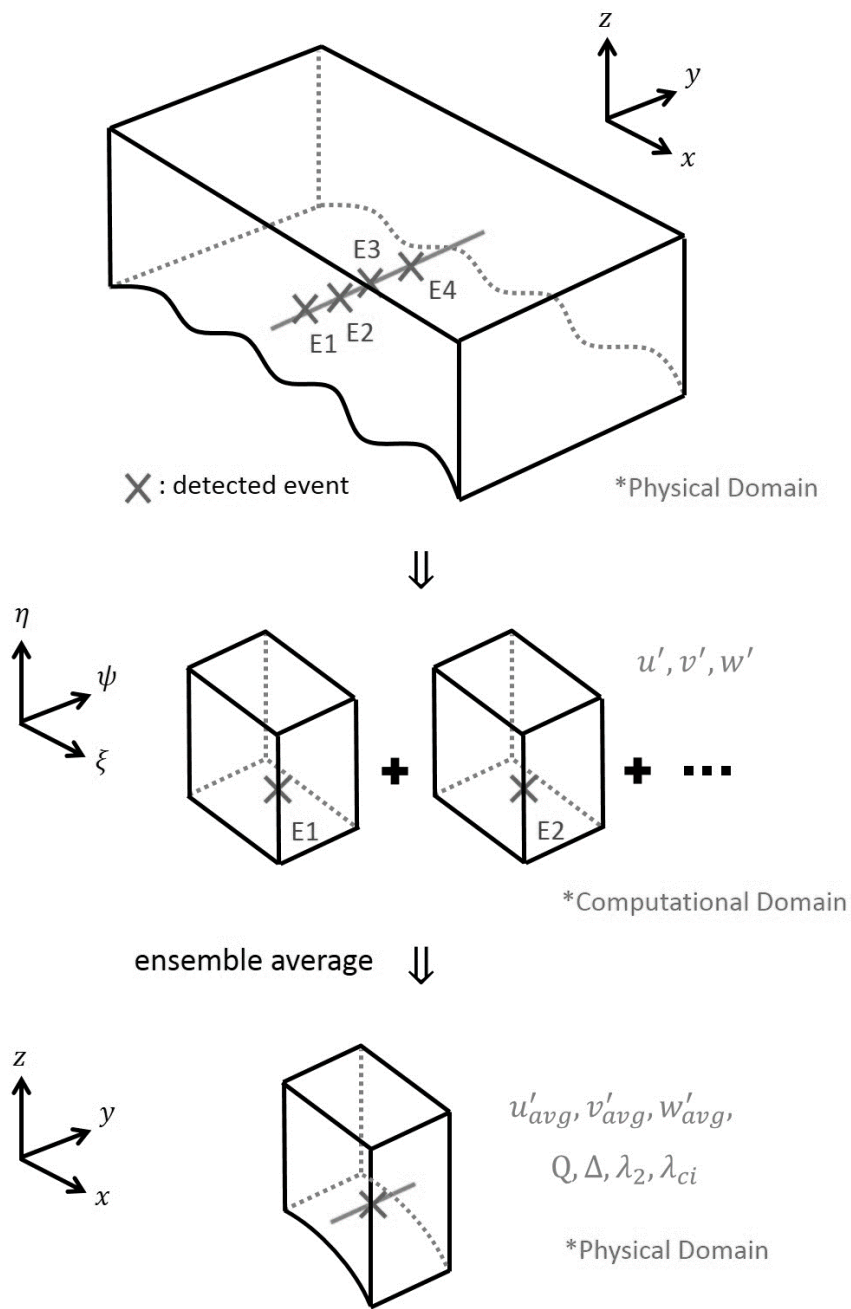


Figure 5-17: An illustration of conditional averaging in the physical domain.



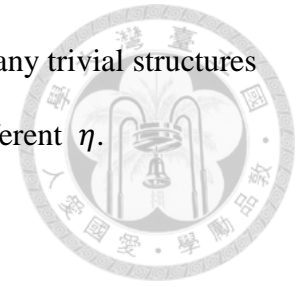
5.3.2 Subjective conditional average

In the previous section, two different procedures of the conditional average are presented. To single out the vortical structures by appropriate detecting criterions and ensure that conditional average with conditional sampling methods is feasible, we first observe the local flow field around the vortical structures which are found subjectively. Afterward, we apply the conditional average technique with conditional sampling methods to numerical simulation. The results of conditional average in manual are shown in this section.

By the observation of horseshoe vortices in Figure 5-9, it is found that forward horseshoe vortices are too rare in the case AR020. Therefore, we ensemble average only the reversed horseshoe vortices in this case, as shown in Figure 5-18. It can be seen that a well-defined reversed horseshoe vortex is located in the center of a subdomain, with complete legs and split head. Furthermore, the result of Δ method is thicker than other methods. To observe the velocity field around the structure, the contour slice of turbulent velocities are shown in Figure 5-19. Around the head part of the reversed horseshoe vortices, the velocity field presents a clockwise rotating vortical motion. Note that upstream to the head of structure, partial derivative of the streamwise turbulent velocity with respect to x are positive.

In the case SR030, more forward horseshoe vortices are observed than reversed horseshoe vortices, as shown in Figure 5-11. A well-defined reversed horseshoe vortex is shown in Figure 5-20, with legs and head clearly represented. Furthermore, the result of Δ method is thicker than other methods. On the contrary, the ensemble average result of the forward horseshoe vortex is terrible, as shown in Figure 5-21. It is found that only

head part of the forward horseshoe vortex can be shown well and many trivial structures are revealed. Such cluttered result is caused by events located in different η .



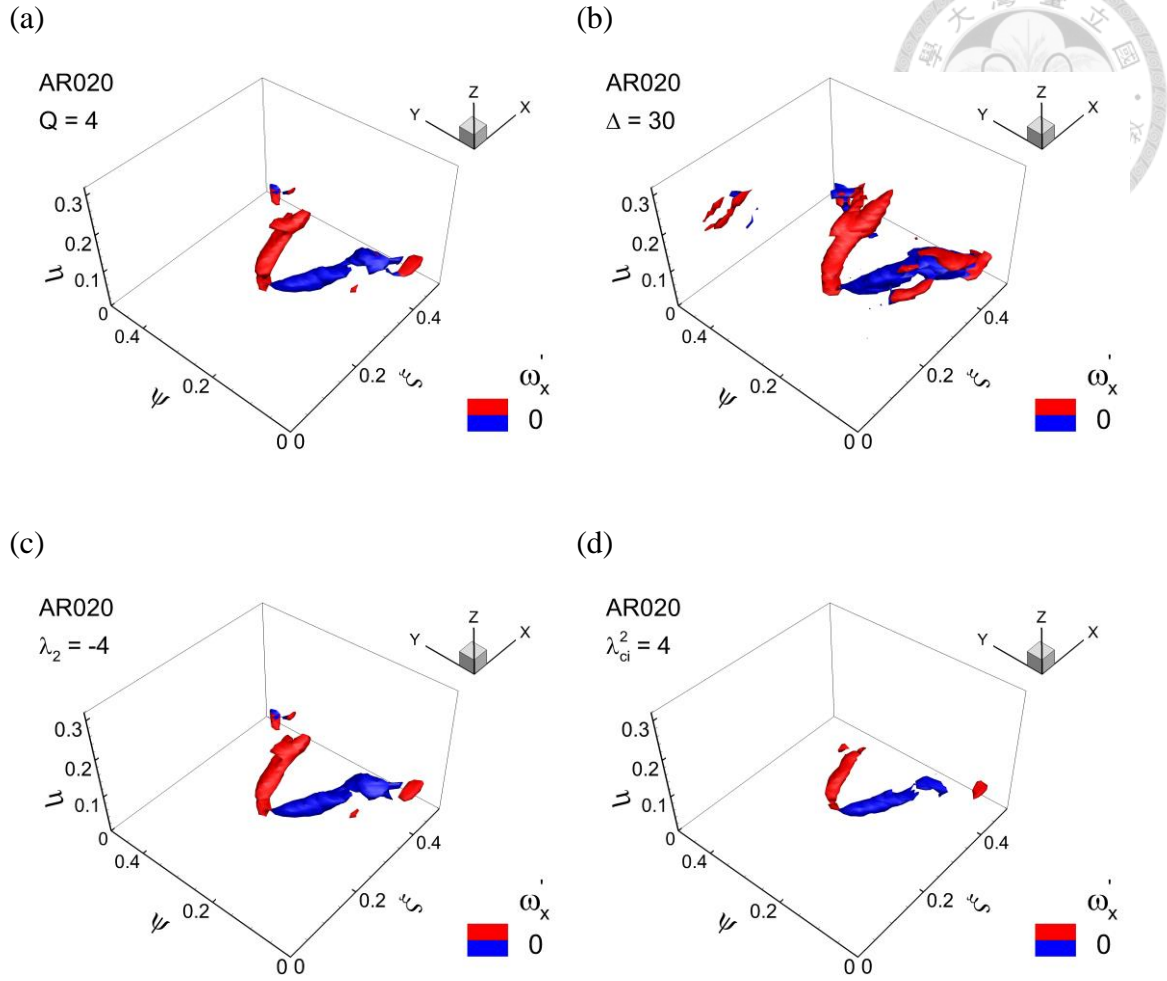


Figure 5-18: Above wavy surface of artificial ripples with $ak = 0.2$: educed reversed horseshoe vortex by conditional averaging subjectively. The structures are represented by the isosurface of (a) $Q = 4$, (b) $\Delta = 30$, (c) $\lambda_2 = -4$, (d) $\lambda_{ci}^2 = 4$. The structures with $\omega'_x > 0$ are marked in red color; the structures with $\omega'_x < 0$ are marked in blue color.

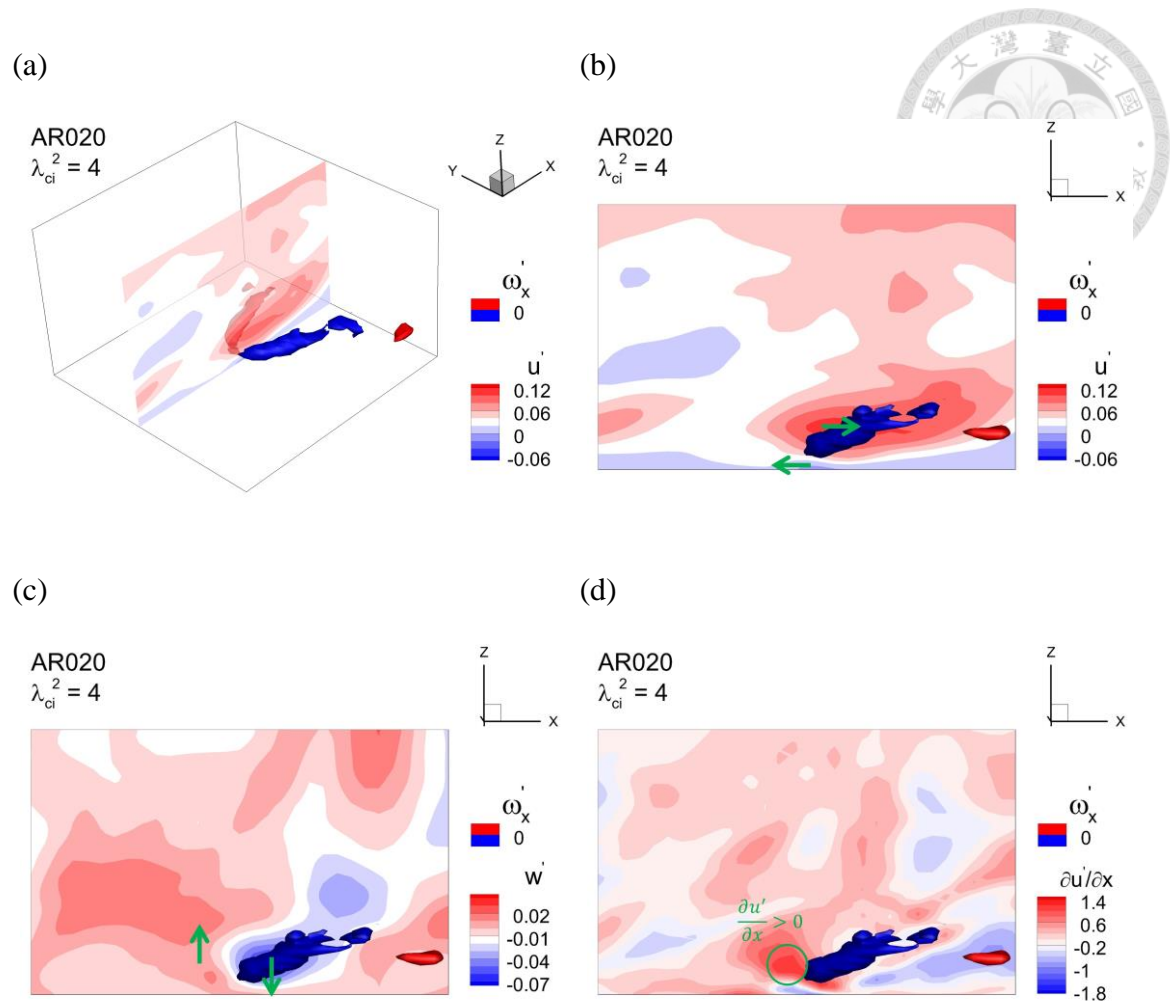


Figure 5-19: Above wavy surface of artificial ripples with $ak = 0.2$: (a) the position of the contour slice; side view of the educed reversed horseshoe vortex by conditional averaging subjectively and contours of (b) streamwise, (c) vertical turbulent velocity, (d) partial derivative of the streamwise turbulent velocity with respect to x . The structures are represented by the isosurface of $\lambda_{ci}^2 = 4$. The structures with $\omega'_x > 0$ are marked in red color; the structures with $\omega'_x < 0$ are marked in blue color. The green arrows indicate flow directions.

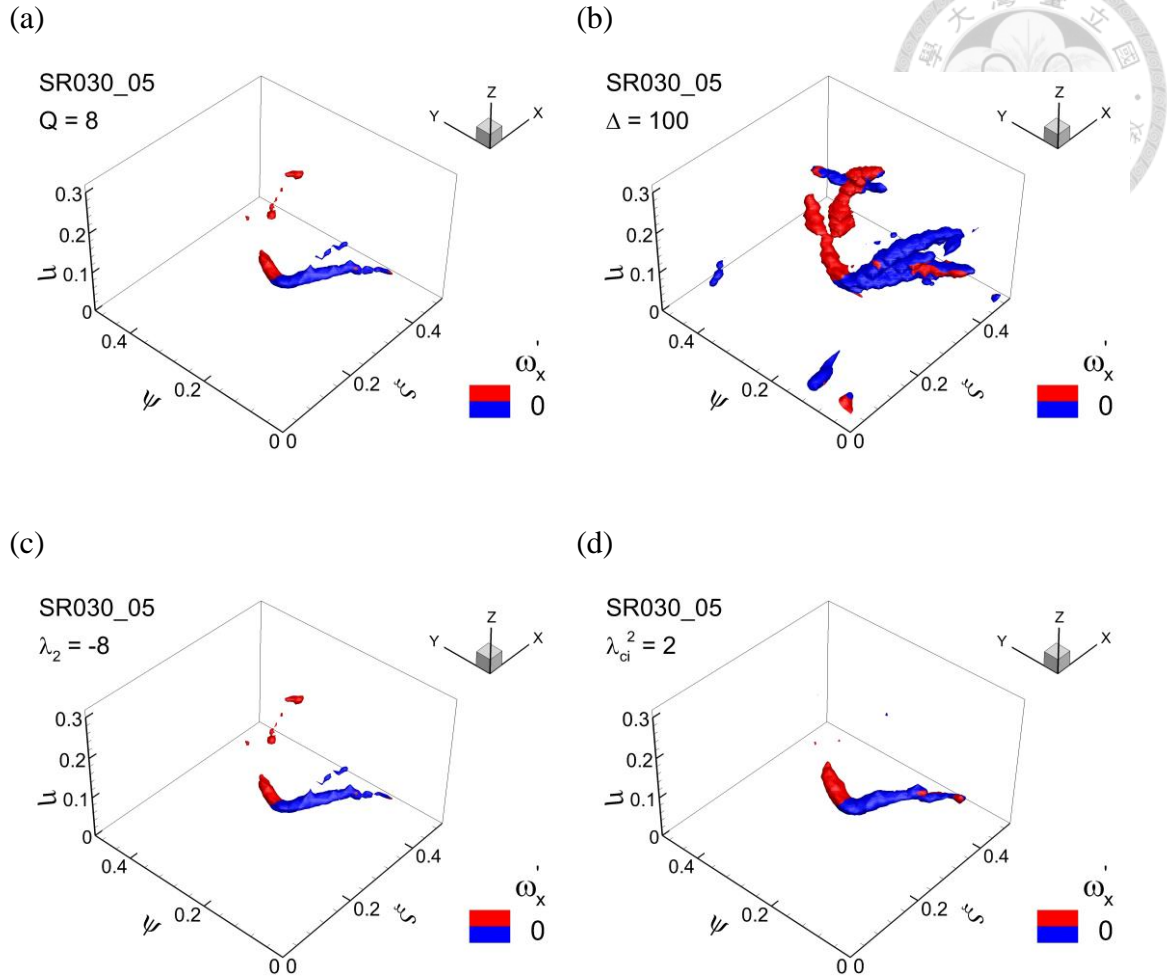


Figure 5-20: Above wavy surface of simulated ripples with $ak = 0.3$, time sequence = 05: educed reversed horseshoe vortex by conditional averaging subjectively. The structures are represented by the isosurface of (a) $Q = 8$, (b) $\Delta = 100$, (c) $\lambda_2 = -8$, (d) $\lambda_{ci}^2 = 2$. The structures with $\omega'_x > 0$ are marked in red color; the structures with $\omega'_x < 0$ are marked in blue color.

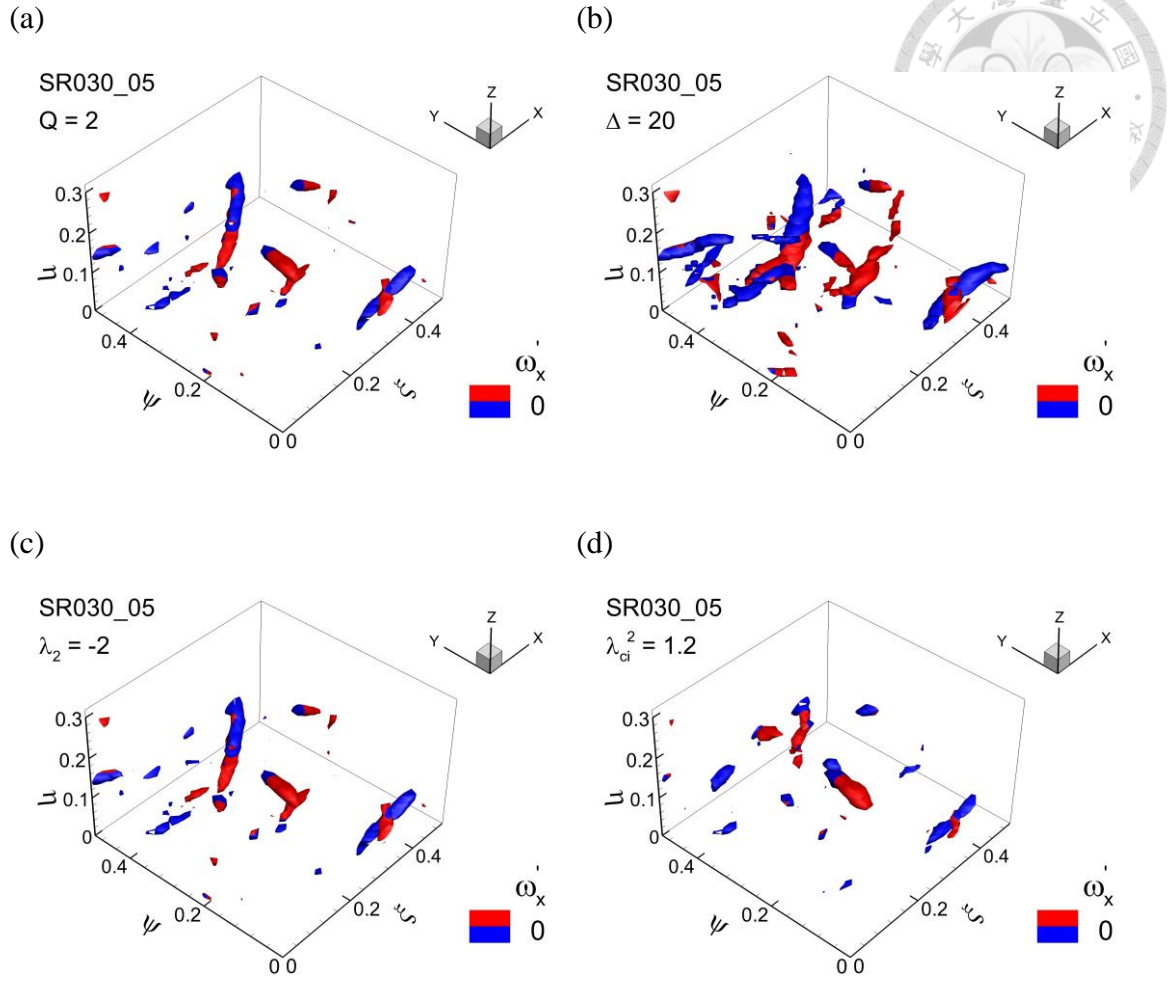
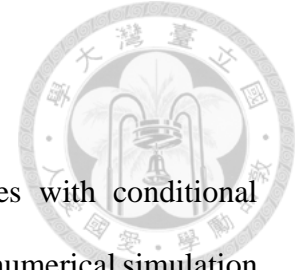


Figure 5-21: Above wavy surface of simulated ripples with $ak = 0.3$, time sequence = 05: educed forward horseshoe vortex by conditional averaging subjectively. The structures are represented by the isosurface of (a) $Q = 2$, (b) $\Delta = 20$, (c) $\lambda_2 = -2$, (d) $\lambda_{ci}^2 = 1.2$. The structures with $\omega'_x > 0$ are marked in red color; the structures with $\omega'_x < 0$ are marked in blue color.

5.3.3 Autonomous conditional average



In this section, we apply the conditional average techniques with conditional sampling methods, such as VISA and quadrant (QD) methods, to the numerical simulation. As introduced in section 5.3.1, referring to Yang and Shen (2009), we use the contours of Reynolds stress $\langle -u'w' \rangle$ to determine the detection positions. Q1 ($u' > 0, w' > 0$), Q2 ($u' < 0, w' > 0$), Q3 ($u' < 0, w' < 0$), and Q4 ($u' > 0, w' < 0$) are the four quadrants of contribution to the Reynold stress. Hereinafter, the contribution from m th-quadrant is referred to as $\langle -u'w' \rangle_m$.

Figure 5-22 shows the color contours of total Reynolds stress above wave surface of the case AR020. It is found that the majority of the contribution to the total Reynold stress comes from the Q2 and Q4 events. The high intensity regions of $\langle -u'w' \rangle_2$ and $\langle -u'w' \rangle_4$ are indicated in Figure 5-22(a) and Figure 5-22(b), respectively. We expect the Q2 events to be associated with the forward horseshoe vortices, and the Q4 events associated with reversed horseshoe vortices. Figure 5-23 shows the conditionally averaged vortical structure associated with the Q4 events of AR020. It can be seen that a well-defined reversed horseshoe vortex is located above the wave trough, with legs and head clearly represented. Figure 5-24 shows the conditionally averaged vortical structure associated with the Q2 events. We expect to find a forward horseshoe vortex; however, two counter-rotating quasi-streamwise vortices incline at a certain angle are revealed in the subdomain. Such result is attributed to the upwelling (Q2) motion induced by the counter-rotating vortex pair; moreover, as we discussed in section 5.2.2, the quasi-streamwise vortices are dominant in the flow field.

Based on the observation in section 5.2.2, the forward horseshoe vortices are rare in the flow field. Hence, we use the VISA sampling method to detect the reversed horseshoe

vortices only. In addition, based on the observation of the velocity field in section 5.3.2, we modify the detecting criterion as

$$D(x, y, z, t_0) = \begin{cases} 1, & \text{if } var > k \cdot u'_{rms}{}^2 \text{ and } \frac{\partial u'}{\partial x} > 0. \\ 0, & \text{otherwise} \end{cases} \quad (5-4)$$

Note that contour of the Reynold stress is impractical for VISA sampling method. Therefore, we subjectively choose an event as the detection position on the (x, z) -plane. The conditionally averaged result is shown in Figure 5-25. It can be seen that the head is shown clearly while legs are split. In addition, some trivial and fine structures are revealed in the flow field.

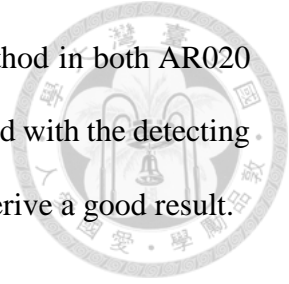
For the case SR030, the color contours of total Reynolds stress above wave surface are shown in Figure 5-26. The conditionally averaged vortical structures associated with the Q4 and Q2 events are shown in Figure 5-27 and Figure 5-28, respectively. It is observed that the conditionally averaged quasi-streamwise vortex pair is shorter than that in the case AR020.

In the previous section, we discussed that the forward horseshoe vortices are located in different η , meaning that detecting at a fixed (x, z) is impracticable. As a result, we use the VISA sampling method to detect the reversed horseshoe vortices only. We failed to detect the events by the detecting criterion of (2-6), hence we modify the detecting criterion as

$$D(x, y, z, t_0) = \begin{cases} 1, & \text{if } var > k \cdot \omega'_{y,rms}{}^2 \text{ and } \omega'_y > 0. \\ 0, & \text{otherwise} \end{cases} \quad (5-5)$$

Figure 5-29 shows the conditionally averaged results of the VISA sampling method detected with (5-5). As shown in the oblique and top view, a conditionally averaged reversed horseshoe vortex exists in the flow field full of structures. To maintain the completeness of the structure, the value of the isosurface is set to be small.

Apparently, the results of QD method are better than VISA method in both AR020 and SR030. However, the VISA sampling method is heavily associated with the detecting criterion; if detected with an appropriate criterion, it is probable to derive a good result.



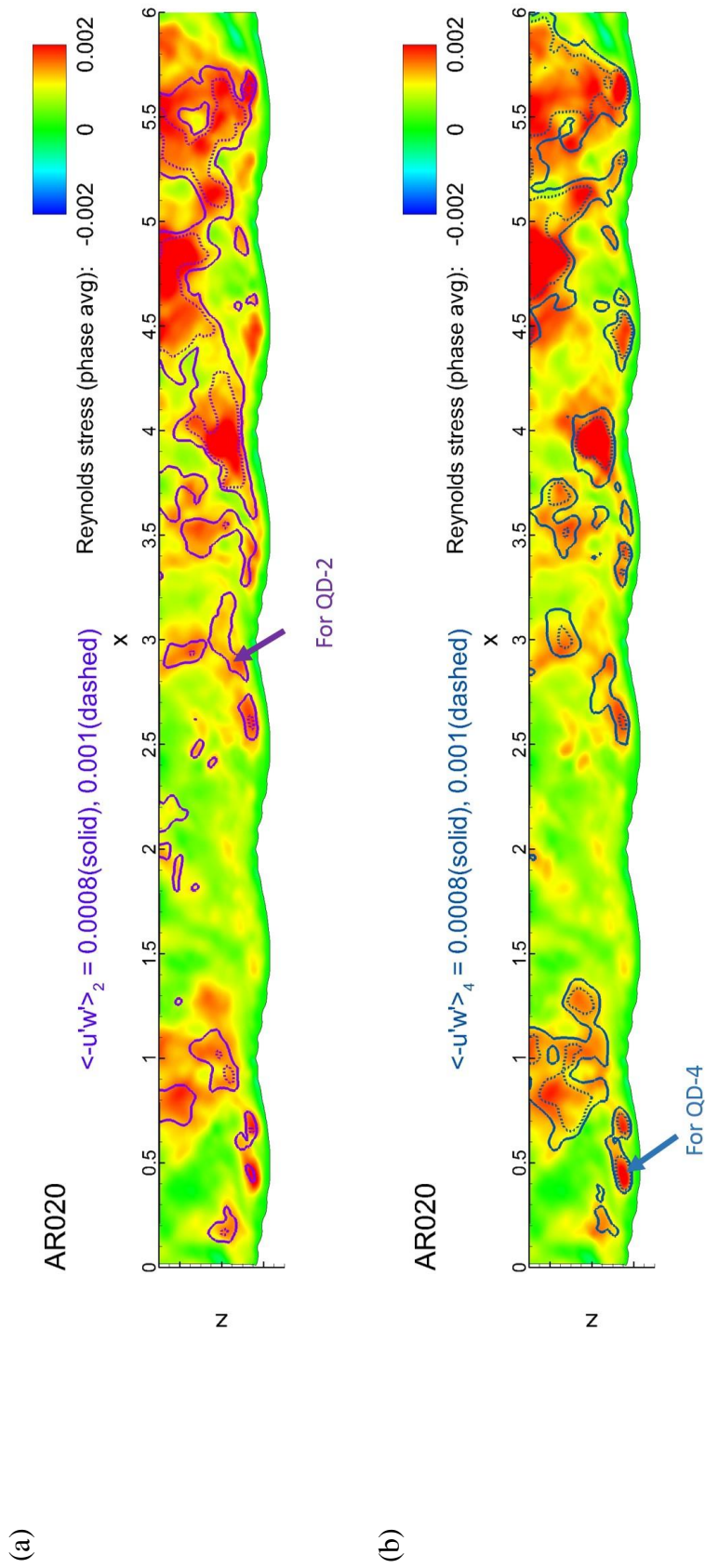
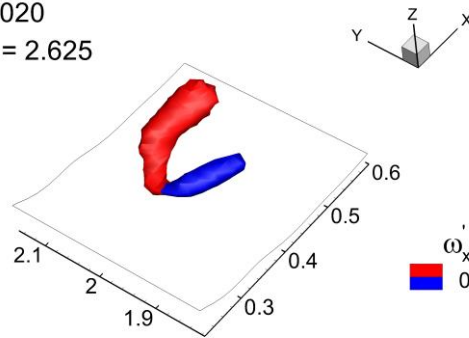


Figure 5-22: Above wavy surface of artificial ripples with $ak = 0.2$: contours of Reynolds stress. (a) High intensity regions of $\langle -u'w' \rangle_2$ are denoted by the 0.0008 and 0.001 contour with solid and dotted lines, respectively; the purple arrow indicate the detection position for the QD-2 method. (b) High intensity regions of $\langle -u'w' \rangle_4$ are denoted by the 0.0008 and 0.001 contour with solid and dotted lines, respectively; the green arrow indicate the detection position for the QD-4 method.



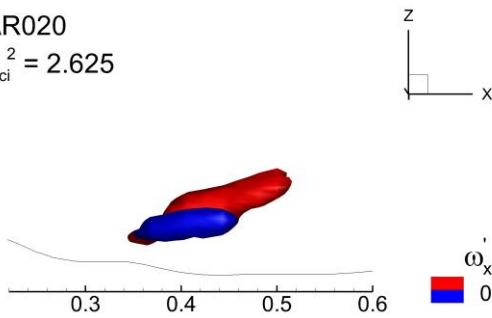
(a)

AR020
 $\lambda_{ci}^2 = 2.625$



(b)

AR020
 $\lambda_{ci}^2 = 2.625$



(c)

AR020
 $\lambda_{ci}^2 = 2.625$

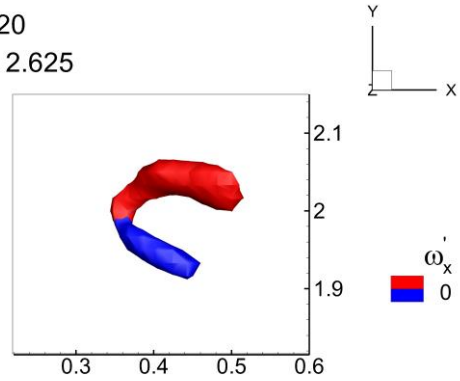
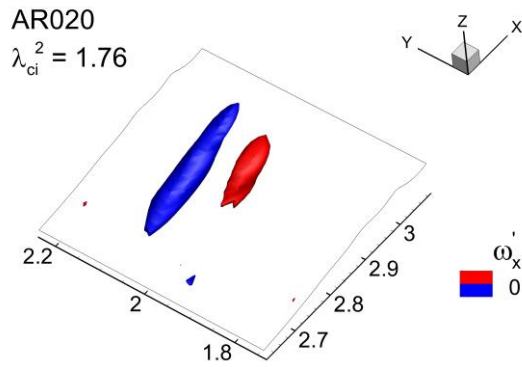
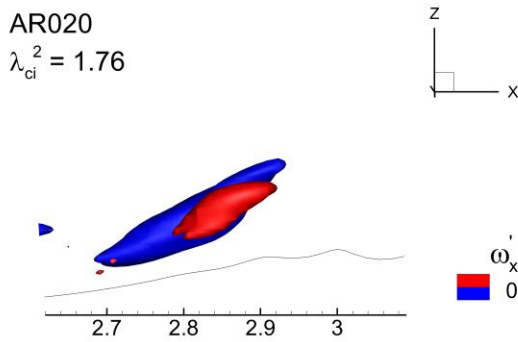


Figure 5-23: Above wavy surface of artificial ripples with $ak = 0.2$: (a) oblique view, (b) side view and (c) top view of the conditionally averaged reversed horseshoe vortex by QD-4 sampling method. The detection threshold is chosen to be 5 and the structures are represented by the isosurface of $\lambda_{ci}^2 = 2.625$. The structures with $\omega'_x > 0$ are marked in red color; the structures with $\omega'_x < 0$ are marked in blue color.

(a)



(b)



(c)

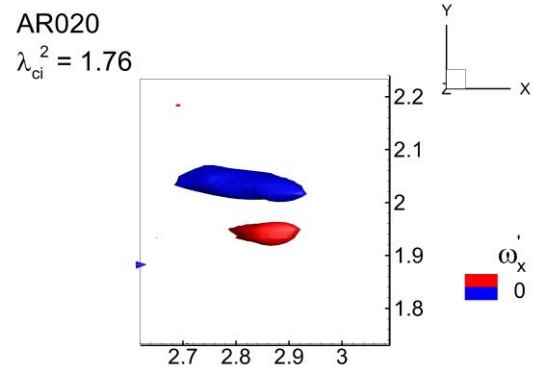
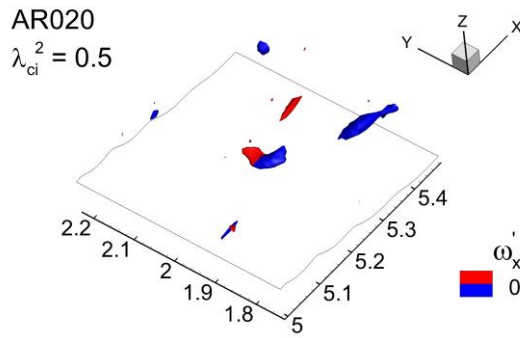
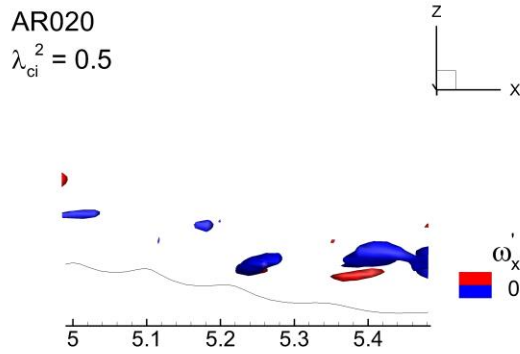


Figure 5-24: Above wavy surface of artificial ripples with $ak = 0.2$: (a) oblique view, (b) side view and (c) top view of the conditionally averaged quasistreamwise vortex by QD-2 sampling method. The detection threshold is chosen to be 3 and the structures are represented by the isosurface of $\lambda_{ci}^2 = 1.76$. The structures with $\omega'_x > 0$ are marked in red color; the structures with $\omega'_x < 0$ are marked in blue color.

(a)



(b)



(c)

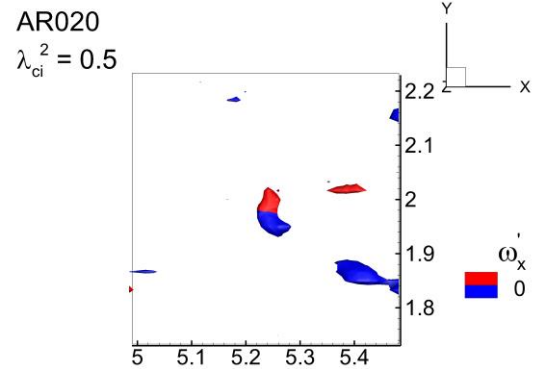


Figure 5-25: Above wavy surface of artificial ripples with $ak = 0.2$: (a) oblique view , (b) side view and (c) top view of the conditionally averaged reversed horseshoe vortex by VISA sampling method. The detection threshold is chosen to be 1.5 and the structures are represented by the isosurface of $\lambda_{ci}^2 = 0.5$. The structures with $\omega'_x > 0$ are marked in red color; the structures with $\omega'_x < 0$ are marked in blue color.

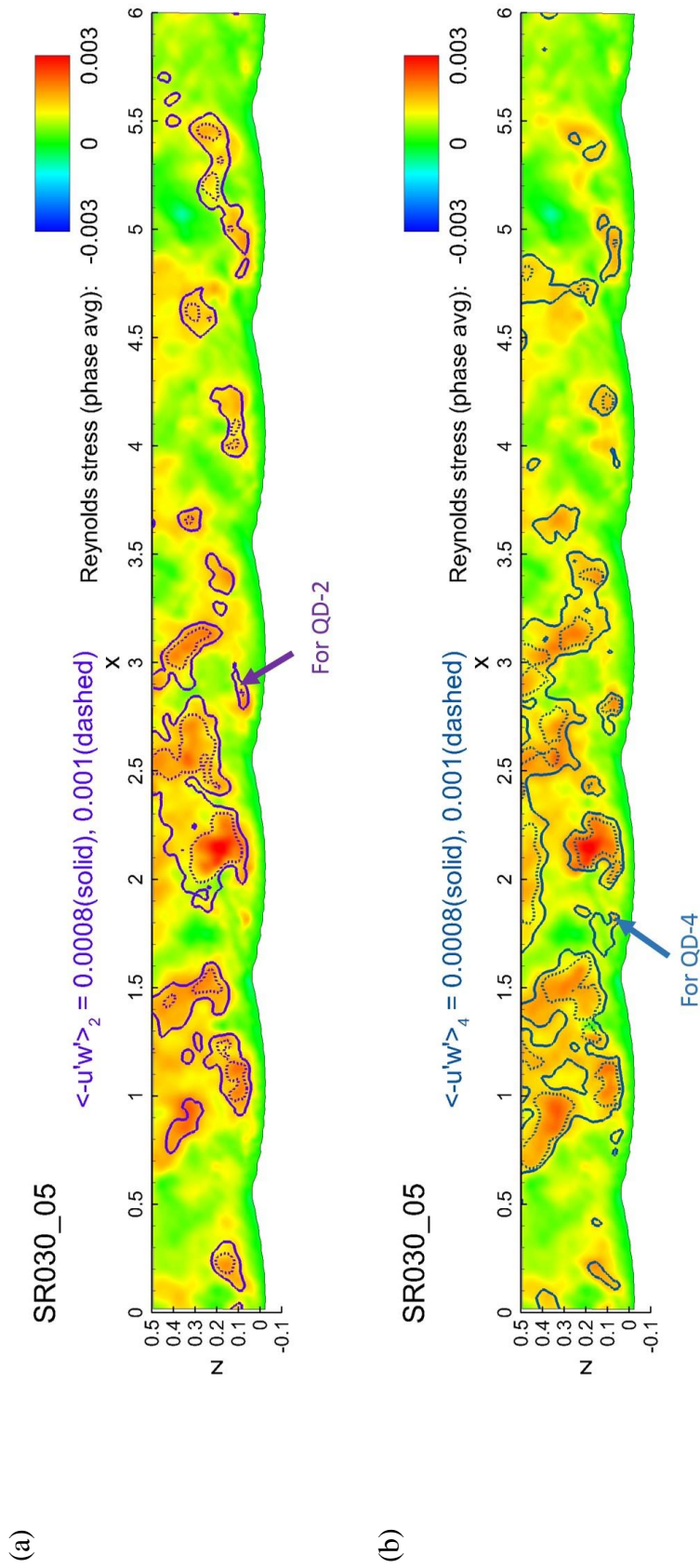
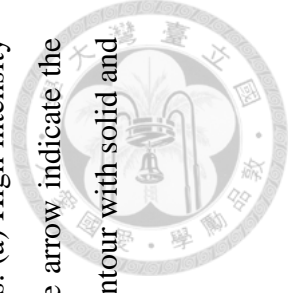


Figure 5-26: Above wavy surface of simulated ripples with $ak = 0.3$, time sequence = 05: contours of Reynolds stress. (a) High intensity regions of $\langle -u'w' \rangle_2$ are denoted by the 0.0008 and 0.001 contour with solid and dotted lines, respectively; the purple arrow indicate the detection position for the QD-2 method. (b) High intensity regions of $\langle -u'w' \rangle_4$ are denoted by the 0.0008 and 0.001 contour with solid and dotted lines, respectively; the green arrow indicate the detection position for the QD-4 method.



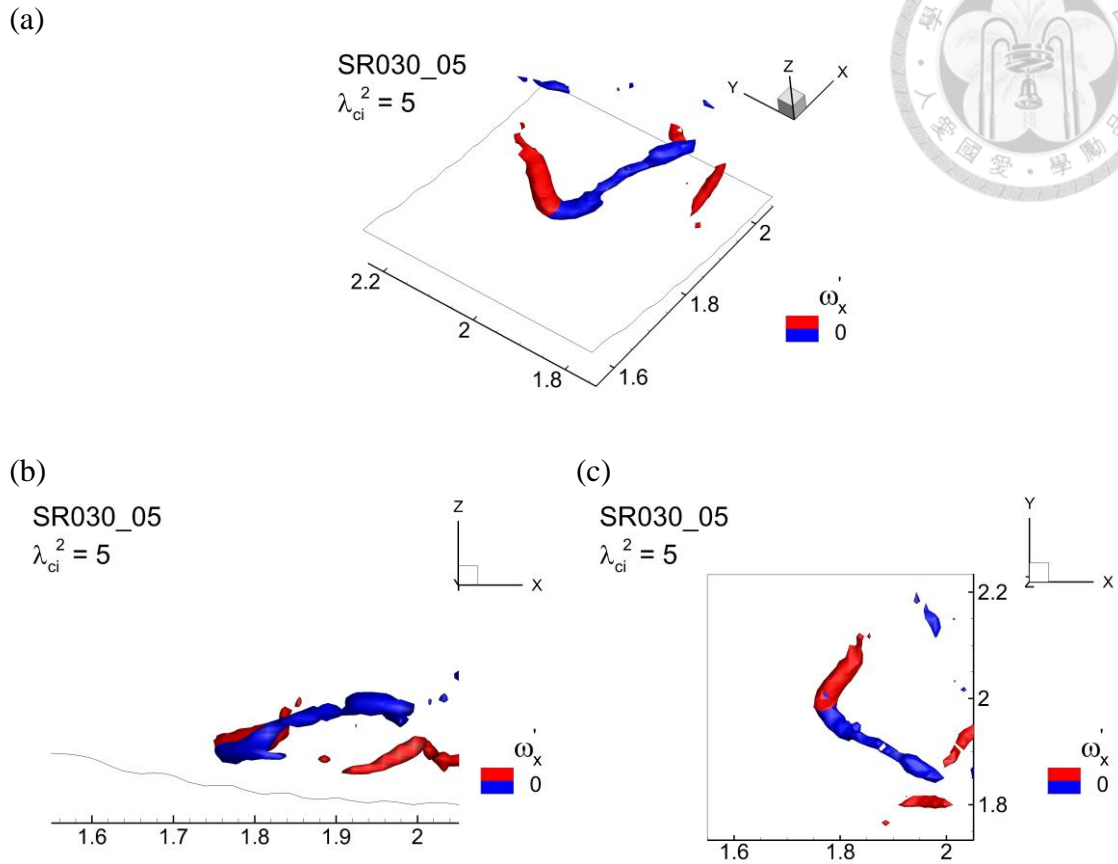


Figure 5-27: Above wavy surface of simulated ripples with $ak = 0.3$, time sequence = 05: (a) oblique view, (b) side view and (c) top view of the conditionally averaged reversed horseshoe vortex by QD-4 sampling method. The detection threshold is chosen to be 10 and the structures are represented by the isosurface of $\lambda_{ci}^2 = 5$. The structures with $\omega'_x > 0$ are marked in red color; the structures with $\omega'_x < 0$ are marked in blue color.

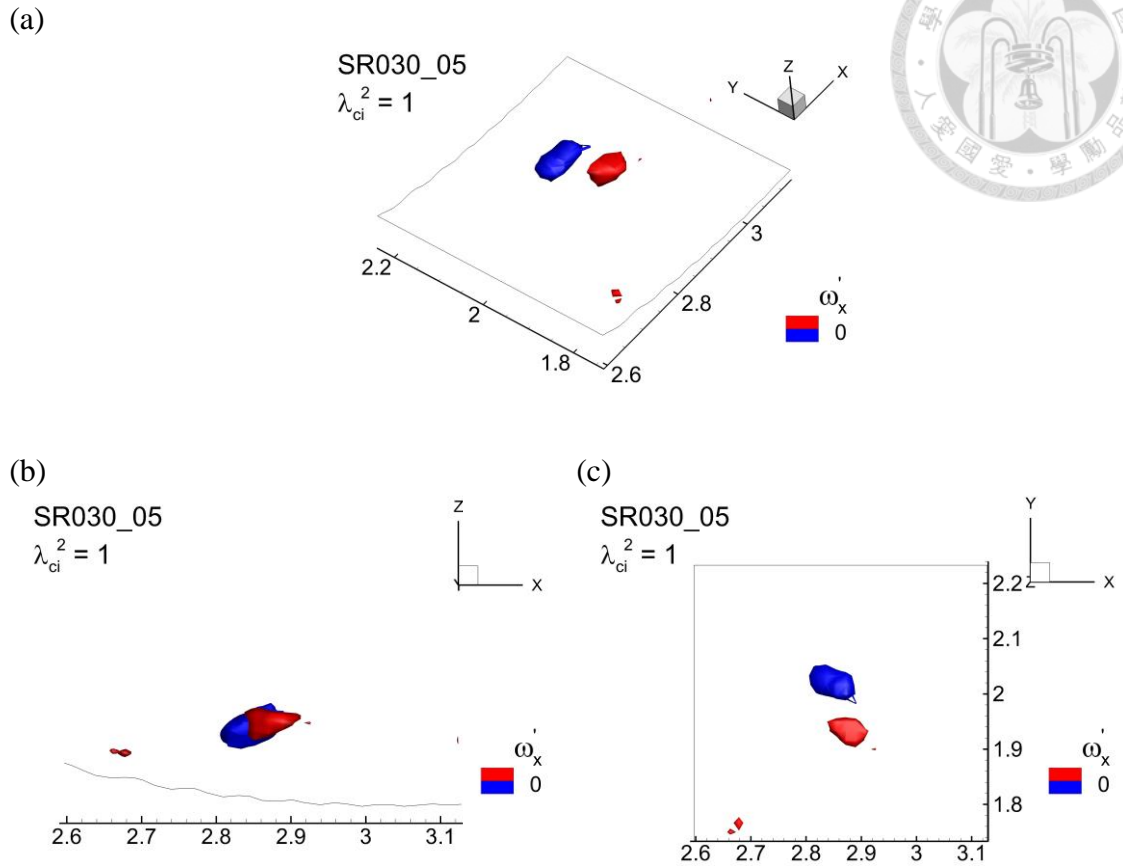


Figure 5-28: Above wavy surface of simulated ripples with $ak = 0.3$, time sequence = 05: (a) oblique view , (b) side view and (c) top view of the conditionally averaged quasistreamwise vortex by QD-2 sampling method. The detection threshold is chosen to be 2 and the structures are represented by the isosurface of $\lambda_{ci}^2 = 1$. The structures with $\omega'_x > 0$ are marked in red color; the structures with $\omega'_x < 0$ are marked in blue color.

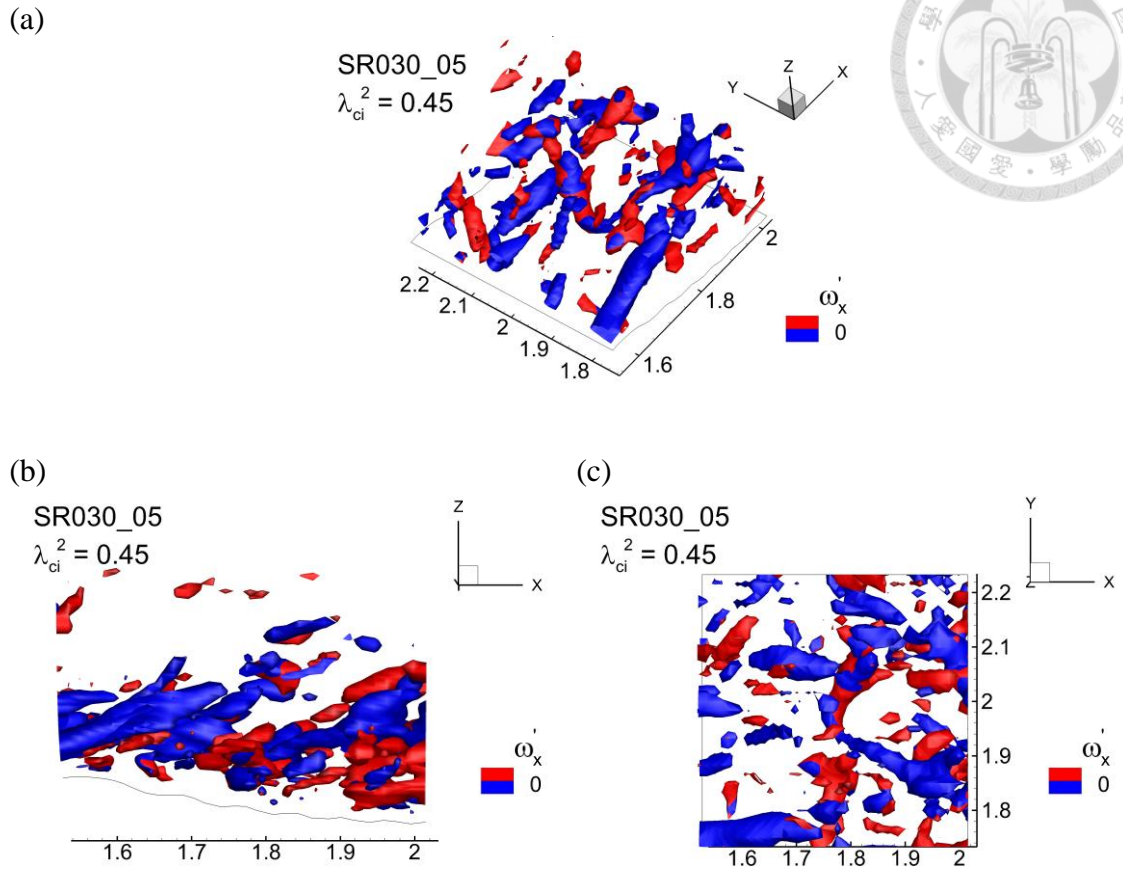


Figure 5-29: Above wavy surface of simulated ripples with $ak = 0.3$, time sequence = 05: (a) oblique view, (b) side view and (c) top view of the conditionally averaged reversed horseshoe vortex by VISA sampling method. The detection threshold is chosen to be 6 and the structures are represented by the isosurface of $\lambda_{ci}^2 = 0.45$. The structures with $\omega'_x > 0$ are marked in red color; the structures with $\omega'_x < 0$ are marked in blue color.



Chapter 6.

Conclusion



In this study, we investigate the flow field near wavy surface in two different sets of numerical simulation. The vortex identification methods are applied to the numerical simulation, showing that four methods could derive similar results by adjusting their isosurface values; however, results of the Δ criterion in the air flow case often shows more fluctuating than others. By drawing the vortex lines among vortical structures, we realize that both of them can explain the mechanism of cold streaks; moreover, observing the vortical structures is a more intuitive way to study the flow field. However, it is inadequate for researchers to study the turbulence by observing the vortical structures only. Other information such as the velocity field, vorticity field, and so forth are essential. For instance, the streamwise turbulent vorticity is marked on the vortical structures to assist the determination of swirling direction in this study. The conditional average results show that the quadrant analysis sampling technique is more feasible than the VISA sampling technique in our cases due to the detecting criterion. For future works, the mechanisms of structure regeneration as well as larger scale vortical motions in the turbulent flow can be investigated.

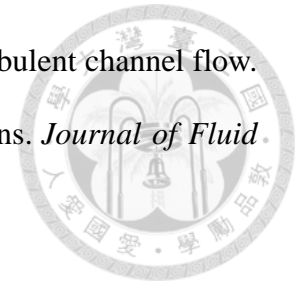


References



- Andrilli, S., & Hecker, D. (2003). *Elementary linear algebra*. Elsevier.
- Blackwelder, R. F., & Kaplan, R. E. (1976). On the wall structure of the turbulent boundary layer. *Journal of Fluid Mechanics*, 76(1), 89-112.
- Chakraborty, P., Balachandar, S., & Adrian, R. J. (2005). On the relationships between local vortex identification schemes. *Journal of fluid mechanics*, 535, 189-214.
- Chong, M. S., Perry, A. E., & Cantwell, B. J. (1990). A general classification of three-dimensional flow fields. *Physics of Fluids A: Fluid Dynamics*, 2(5), 765-777.
- Druzhinin, O. A., Troitskaya, Y. I., & Zilitinkevich, S. S. (2012). Direct numerical simulation of a turbulent wind over a wavy water surface. *Journal of Geophysical Research: Oceans*, 117(C11).
- Hunt, J. C., Wray, A. A., & Moin, P. (1988). Eddies, streams, and convergence zones in turbulent flows.
- Jeong, J., & Hussain, F. (1995). On the identification of a vortex. *Journal of fluid mechanics*, 285, 69-94.
- Kim, J. (1983). On the structure of wall-bounded turbulent flows. *The Physics of fluids*, 26(8), 2088-2097.
- Kim, J., & Moin, P. (1986). The structure of the vorticity field in turbulent channel flow. Part 2. Study of ensemble-averaged fields. *Journal of Fluid Mechanics*, 162, 339-363.
- Kreyszig, E. (2010). *Advanced engineering mathematics*. John Wiley & Sons.

Moin, P., & Kim, J. (1985). The structure of the vorticity field in turbulent channel flow. Part 1. Analysis of instantaneous fields and statistical correlations. *Journal of Fluid Mechanics*, 155, 441-464.



Robinson, S. K. (1991). Coherent motions in the turbulent boundary layer. *Annual Review of Fluid Mechanics*, 23(1), 601-639.

Schafhitzel, T., Vollrath, J. E., Gois, J. P., Weiskopf, D., Castelo, A., & Ertl, T. (2008, May). Topology - Preserving λ_2 - based Vortex Core Line Detection for Flow Visualization. In *Computer Graphics Forum* (Vol. 27, No. 3, pp. 1023-1030). Blackwell Publishing Ltd.

Tsai, W. T., Chen, S. M., & Lu, G. H. (2015). Numerical evidence of turbulence generated by nonbreaking surface waves. *Journal of Physical Oceanography*, 45(1), 174-180.

Tsai, W. T., Lu, G. H., Chen, J. R., Dai, A., & Phillips, W. R. (2017). On the Formation of Coherent Vortices beneath Nonbreaking Free-Propagating Surface Waves. *Journal of Physical Oceanography*, 47(3), 533-543.

Willmarth, W. W., & Lu, S. S. (1972). Structure of the Reynolds stress near the wall. *Journal of Fluid Mechanics*, 55(1), 65-92.

Wallace, J. M., Eckelmann, H., & Brodkey, R. S. (1972). The wall region in turbulent shear flow. *Journal of Fluid Mechanics*, 54(1), 39-48.

Yang, D., & Shen, L. (2009). Characteristics of coherent vortical structures in turbulent flows over progressive surface waves. *Physics of Fluids*, 21(12), 125106.

Zhou, J., Adrian, R. J., Balachandar, S., & Kendall, T. M. (1999). Mechanisms for generating coherent packets of hairpin vortices in channel flow. *Journal of fluid mechanics*, 387, 353-396.

Appendix A.

Phase plane method and critical point theory



Consider a two dimensional homogeneous system

$$\mathbf{y}' = \mathbf{A}\mathbf{y}; \quad (\text{A-1})$$

in components,

$$y_1' = a_{11}y_1 + a_{12}y_2, \quad (\text{A-2})$$

$$y_2' = a_{21}y_1 + a_{22}y_2,$$

try the solution

$$\mathbf{y} = \mathbf{x}e^{\lambda t}. \quad (\text{A-3})$$

Substitute (A-3) into (A-1) and eliminate $e^{\lambda t}$, we obtain the eigenvalue problem

$$\mathbf{A}\mathbf{x} = \lambda\mathbf{x}. \quad (\text{A-3})$$

Hence the general solution is

$$\mathbf{y} = c_1\mathbf{x}_1e^{\lambda_1 t} + c_2\mathbf{x}_2e^{\lambda_2 t}, \quad (\text{A-4})$$

where c_1, c_2 are constant coefficients, $\mathbf{x}_1, \mathbf{x}_2$ and λ_1, λ_2 are the eigenvectors and eigenvalues of \mathbf{A} . From (A-2), we obtain

$$\frac{dy_2}{dy_1} = \frac{y_2'}{y_1'} = \frac{a_{21}y_1 + a_{22}y_2}{a_{11}y_1 + a_{12}y_2}. \quad (\text{A-5})$$

At a point $P(y_1, y_2) = (0,0)$, (A-4) becomes $0/0$. Therefore, this point is called a critical point.

The (y_1, y_2) -plane is called the phase plane. There are five types of critical points in the phase plane, depending on the geometric shape of the trajectories near them. As figure A-1 shown, improper node, proper node and saddle point occur when the

eigenvalues are real; in contrast, center and spiral point occur when the eigenvalues are not real.

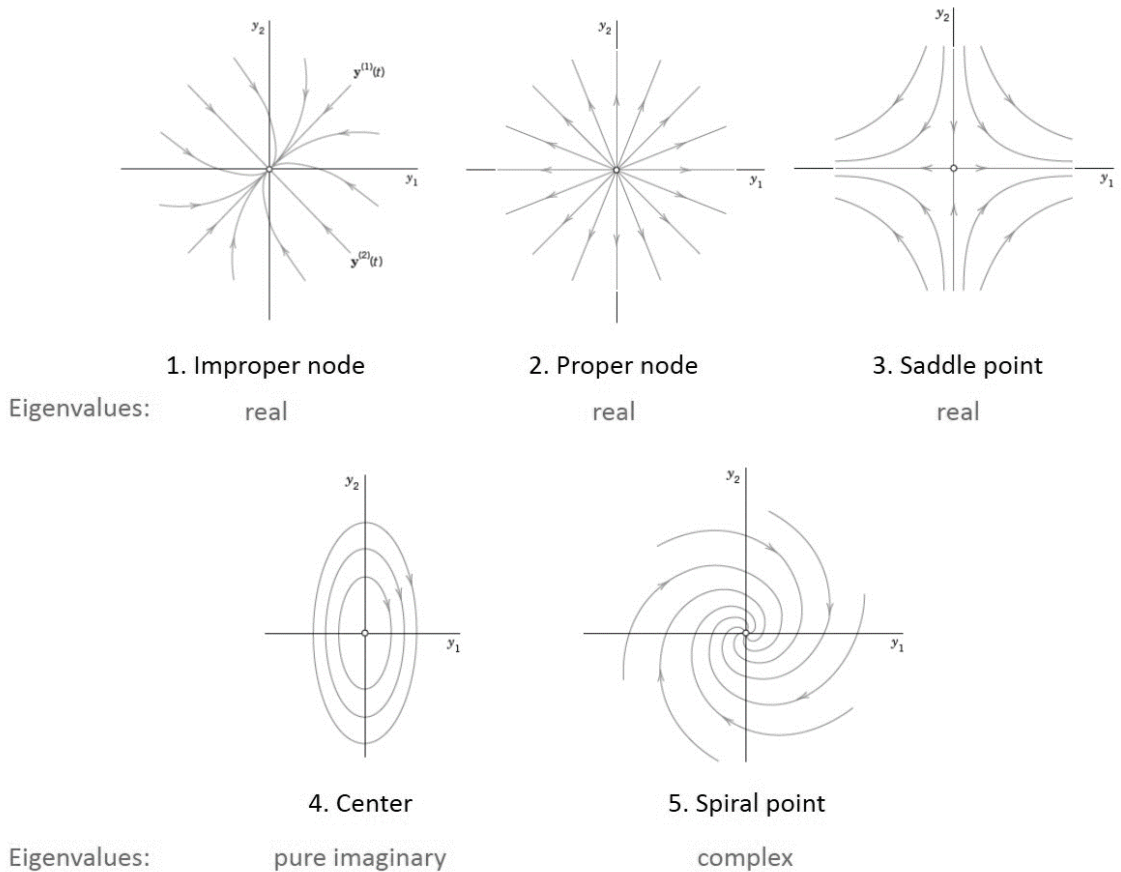


Figure A-1: Five types of critical points (phase portrait). Adapted from Advanced engineering mathematics (p.143-145), by Kreyszig, E., 2010. Copyright 2011, 2006, 1999 by John Wiley & Sons, Inc.

Appendix B.

Properties of the Hessian matrix



The Hessian matrix

$$H_{i,j} = \frac{\partial^2 f}{\partial x_i \partial x_j}, \quad (\text{B-1})$$

has the following properties: If the Hessian is positive definite (all its eigenvalues are positive), then f attains a local minimum. If the Hessian is negative definite (all its eigenvalues are negative), then f attains a local maximum. If the Hessian has both positive and negative eigenvalues then it is a saddle point for f .

Take two dimensional array for instance, close to a local extreme point \mathbf{x}_0 the Taylor series of a function $f(\mathbf{x}_0 + \mathbf{c})$ can be expressed as

$$\begin{aligned} f(\mathbf{x}_0 + \mathbf{c}) &= f(\mathbf{x}_0) + f_x|_{\mathbf{x}_0} \cdot c_1 + f_y|_{\mathbf{x}_0} \cdot c_2 \\ &\quad + \frac{1}{2}(f_{xx}|_{\mathbf{x}_0} \cdot c_1^2 + f_{yy}|_{\mathbf{x}_0} \cdot c_2^2 + 2f_{xy}|_{\mathbf{x}_0} \cdot c_1 c_2) \\ &= f(\mathbf{x}_0) + \nabla f \cdot \mathbf{c} + \frac{1}{2}c_1(f_{xx}c_1 + f_{xy}c_2) + \frac{1}{2}c_2(f_{xy}c_1 + f_{yy}c_2) \quad (\text{B-2}) \\ &= f(\mathbf{x}_0) + \nabla f \cdot \mathbf{c} + \frac{1}{2} \begin{bmatrix} c_1 & c_2 \end{bmatrix} \begin{bmatrix} f_{xx} & f_{xy} \\ f_{yx} & f_{yy} \end{bmatrix} \begin{bmatrix} c_1 \\ c_2 \end{bmatrix} \\ &= f(\mathbf{x}_0) + \nabla f \cdot \mathbf{c} + \frac{1}{2} \mathbf{c}^T \mathbf{H} \mathbf{c}, \end{aligned}$$

where $\mathbf{c} = \begin{bmatrix} c_1 \\ c_2 \end{bmatrix}$ and \mathbf{H} is the Hessian matrix. At a critical point, the first derivative of function f must be zero, hence

$$f(\mathbf{x}_0 + \mathbf{c}) = f(\mathbf{x}_0) + \frac{1}{2} \mathbf{c}^T \mathbf{H} \mathbf{c}. \quad (\text{B-3})$$

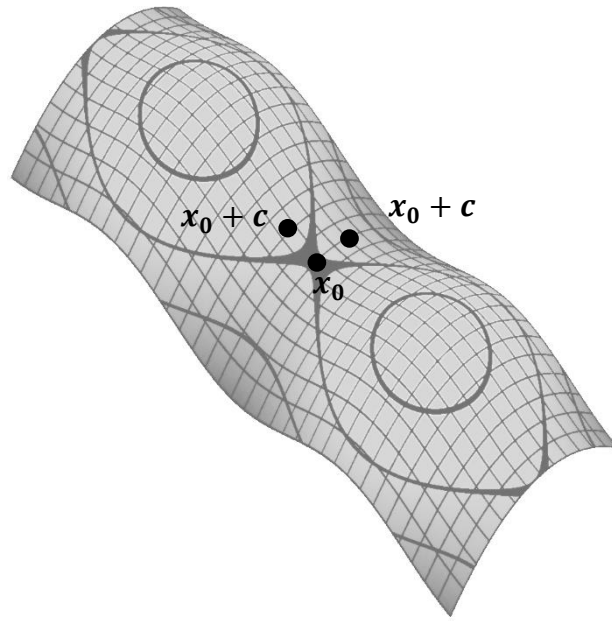


Figure B-1: An illustration of a saddle point. Adapted July 25, 2017, from https://commons.wikimedia.org/wiki/User:StuRat#/media/File:Saddle_pt.jpg.

As figure B-1 shows, if $\mathbf{c}^T \mathbf{H} \mathbf{c} > 0$, then $f(\mathbf{x}_0 + \mathbf{c}) > f(\mathbf{x}_0)$, which means \mathbf{x}_0 is a local minimum point in $\mathbf{x}_0 - \mathbf{c}$ direction. In contrast, if $\mathbf{c}^T \mathbf{H} \mathbf{c} < 0$, then $f(\mathbf{x}_0 + \mathbf{c}) < f(\mathbf{x}_0)$, which means \mathbf{x}_0 is a local maximum point in $\mathbf{x}_0 - \mathbf{c}$ direction.

The Hessian matrix \mathbf{H} can be decomposed by its eigenvalues and eigenvectors

$$\mathbf{H} = \mathbf{E}^T \mathbf{D} \mathbf{E}, \quad (\text{B-4})$$

where $\mathbf{E} = \begin{bmatrix} \mathbf{E}_1 \\ \mathbf{E}_2 \end{bmatrix}$ is the matrix of eigenvectors, $\mathbf{D} = \begin{bmatrix} \lambda_1 & \mathbf{0} \\ \mathbf{0} & \lambda_2 \end{bmatrix}$ is the matrix of eigenvalues. Then,

$$\mathbf{c}^T \mathbf{H} \mathbf{c} = \mathbf{c}^T \mathbf{E}^T \mathbf{D} \mathbf{E} \mathbf{c} = \mathbf{w}^T \mathbf{D} \mathbf{w}, \quad (\text{B-5})$$

where \mathbf{w} is the product of matrix \mathbf{E} and \mathbf{c} . Since \mathbf{D} is diagonal,

$$\mathbf{w}^T \mathbf{D} \mathbf{w} = [w_1 \quad w_2] \begin{bmatrix} \lambda_1 & 0 \\ 0 & \lambda_2 \end{bmatrix} \begin{bmatrix} w_1 \\ w_2 \end{bmatrix} = \lambda_1 w_1^2 + \lambda_2 w_2^2. \quad (\text{B-6})$$

If λ_1 & $\lambda_2 > 0$, then $\mathbf{w}^T \mathbf{D} \mathbf{w} > \mathbf{0}$, thus \mathbf{x}_0 is a local minimum point. If λ_1 & $\lambda_2 < 0$, then $\mathbf{w}^T \mathbf{D} \mathbf{w} < \mathbf{0}$, thus \mathbf{x}_0 is a local maximum point. If λ_1 & λ_2 are opposite sign, then $\mathbf{w}^T \mathbf{D} \mathbf{w}$ can be positive or negative (depend on \mathbf{c}), thus \mathbf{x}_0 is a saddle point.

